

Hot-Spot Formation in Cu(In,Ga)Se₂ Thin Film Solar Cells

Suheir Nofal

Energie & Umwelt / Energy & Environment

Band / Volume 703

ISBN 978-3-95806-903-9

Forschungszentrum Jülich GmbH
Institute of Energy Materials and Devices (IMD)
Photovoltaik (IMD-3)

Hot-Spot Formation in Cu(In,Ga)Se₂ Thin Film Solar Cells

Suheir Nofal

Schriften des Forschungszentrums Jülich
Reihe Energie & Umwelt / Energy & Environment

Band / Volume 703

ISSN 1866-1793

ISBN 978-3-95806-903-9

Bibliografische Information der Deutschen Nationalbibliothek.
Die Deutsche Nationalbibliothek verzeichnet diese Publikation in der
Deutschen Nationalbibliografie; detaillierte Bibliografische Daten
sind im Internet über <http://dnb.d-nb.de> abrufbar.

Herausgeber und Vertrieb: Forschungszentrum Jülich GmbH
Zentralbibliothek, Verlag
52425 Jülich
Tel.: +49 2461 61-5368
Fax: +49 2461 61-6103
zb-publikation@fz-juelich.de
www.fz-juelich.de/zb

Umschlaggestaltung: Grafische Medien, Forschungszentrum Jülich GmbH

Druck: Grafische Medien, Forschungszentrum Jülich GmbH

Copyright: Forschungszentrum Jülich 2026

Schriften des Forschungszentrums Jülich
Reihe Energie & Umwelt / Energy & Environment, Band / Volume 703

D 82 (Diss. RWTH Aachen University, 2025)

ISSN 1866-1793
ISBN 978-3-95806-903-9

Vollständig frei verfügbar über das Publikationsportal des Forschungszentrums Jülich (JuSER)
unter www.fz-juelich.de/zb/openaccess.



This is an Open Access publication distributed under the terms of the [Creative Commons Attribution License 4.0](https://creativecommons.org/licenses/by/4.0/), which permits unrestricted use, distribution, and reproduction in any medium, provided the original work is properly cited.

Abstract

Photovoltaic (PV) modules are susceptible to reliability concerns under *reverse bias* conditions, particularly when subjected to partial shading. When a solar cell is shaded, it generates less current than its unshaded counterparts, causing excess current to flow in reverse through the affected cell. This can result in a substantial reverse voltage, potentially leading to junction breakdown. Under sustained reverse bias stress, localized regions of the cell can become highly conductive, drawing in more current and dissipating it as heat. This heat accumulation can lead to the formation of localized "hotspots," a phenomenon observed across all PV technologies. However, the severity of reverse bias damage varies depending on the material system and device architecture.

A key reliability concern associated with reverse bias damage is the presence of positive feedback effects, which can trigger *thermal runaway*. A positive feedback loop where the hotspot becomes more conductive at higher temperatures, leads to an unstable system where the temperature rises quickly [1]. If the temperature surpasses a critical threshold, the cell undergoes irreversible damage.

Thin-film solar technologies are particularly susceptible to reverse bias-induced thermal runaway due to their structural and thermal properties. The encapsulation materials commonly used in PV modules have poor thermal conductivity, limiting their ability to dissipate heat efficiently. Additionally, the inherently thin absorber layers of thin-film modules provide little thermal mass, making them more prone to rapid temperature increases compared to conventional wafer-based PV technologies.

Among thin-film solar cells, copper indium gallium selenide (Cu(In,Ga)Se_2 or CIGS) is a particularly promising candidate due to its high absorption coefficient of approximately 10^5 cm^{-1} in the visible spectrum (400–700 nm) [2]. This property enables ultra-thin absorber layers (1 – 2 μm), facilitating lightweight and flexible applications such as vehicle- and building-integrated photovoltaics (VIPV and BIPV) and unmanned aerial vehicles (UAVs) [3, 4]. However, like other thin-film technologies, CIGS is prone to reverse bias damage due to its low thermal mass and the limited heat dissipation capabilities of standard encapsulation materials. A well-documented reverse bias degradation mechanism in CIGS solar cells is the formation of so-called "wormlike defects" [5, 6].

In this thesis, I propose a three-phase model describing the progression of re-

verse bias damage in CIGS solar cells: (i) the *nucleation phase*, (ii) the *growth phase*, and (iii) the *wandering phase*. During the *nucleation phase*, thermal activation of the junction breakdown current leads to an initial instability, initiating a thermal runaway. This phase concludes when thermal decomposition occurs, segregating the CIGS material and forming a conductive shunt-like defect, marking the transition to irreversible damage. In the *growth phase*, the defect expands from the nanometer to the micrometer scale. Finally, in the *wandering phase*, the defect propagates through the cell, forming elongated wormlike structures.

To investigate the *nucleation phase*, I developed a novel characterization method called *Laser-Induced Hot-Spot Lock-In Thermography* (HS-LIT) to visualize and quantify the interplay between thermal heat and electrical power. Initial measurements revealed that laser-induced hotspots caused localized power redistribution, leading to temperature increases. To enhance measurement precision, I introduced laser modulation, enabling the direct quantification of the loop gain driving the thermal runaway. A thermal runaway occurs when the loop gain exceeds 1. Typically, a loop gain above 1 is unmeasurable because it signifies an unstable system. However, in a modulated experiment, the system can temporarily exhibit loop gains above 1 while remaining stable over an entire modulation cycle. This allows for the non destructive quantification of a loop gain above 1, demonstrating that the system *would be* unstable under DC conditions.

Experimental results confirmed that thermal runaway is more likely at higher voltages. For instance, a commercial CIGS solar cell on a glass substrate exhibited loop gains of 1.05, 1.10, and 2.03 at reverse biases of 2, 2.5, and 3 V, respectively, demonstrating a superlinear scaling trend. Additionally, HS-LIT measurements revealed that hotspots near the P1 scribe line exhibited higher loop gains compared to those near P3. Further experiments on flexible CIGS modules with steel substrates revealed significantly lower loop gains compared to cells on glass, attributed to the high thermal conductivity of the steel substrate, which effectively dissipated heat from the local hotspot.

To analyze the *growth phase*, I implemented a coupled *electro-thermal finite element model* (FEM) with high spatial and temporal resolution to simulate defect expansion. The model assumes that after the initial thermal runaway, a small ohmic defect is formed. This defect subsequently exhibits its own positive feedback loop, as power dissipation within the defect heats the surrounding material. If the temperature surpasses a critical threshold, the material undergoes decomposition, forming a conductive phase and thereby enlarging the shunt-like defect. The model successfully replicated experimentally observed defect growth, predicting that an initial defect with a radius of 10 nm could expand to a 5 μm defect within just 1 ms. For this result we assume a defect with a resistivity of $R_{\text{def}} = 3.14 \times 10^{-7} \Omega\text{cm}^2$. Simulations demonstrated that lower-resistivity defects grow more rapidly, whereas higher-resistivity defects tend to stabilize or cease expanding. Furthermore, the study examined how different device stack layers influence defect evolution, confirming that compared to glass, steel foil substrates suppress thermal runaway due to enhanced heat dissipation.

Finally, the *wandering phase* was explored using the same simulation model employed for the growth phase. These simulations examined how defect location influences propagation dynamics. Results showed that defects originating near P1 interconnections exhibited little wandering, tending to expand along the P1 line. In contrast, defects forming near the P3 scribe line propagated rapidly toward the P1 line. A 10 nm defect near P3 expanded over a length of $13.5\ \mu\text{s}$ within $18.5\ \mu\text{s}$, driven by applied power. These results align well with observations in the literature.

This work provides a comprehensive framework for understanding reverse bias damage in CIGS solar cells, integrating experimental and modeling approaches to characterize and mitigate thermal runaway. The findings highlight the crucial influence of defect location and substrate selection on the reliability of CIGS thin-film photovoltaics.

Kurzfassung

Photovoltaik (PV)-Module sind unter *Rückwärtsspannung* (Reverse Bias) besonders anfällig für Zuverlässigkeitsprobleme, insbesondere bei Teilverschattung. Wenn eine Solarzelle verschattet wird, erzeugt sie weniger Strom als die unverschatteten Zellen, wodurch überschüssiger Strom in umgekehrter Richtung durch die betroffene Zelle fließt. Dies kann zu einer erheblichen Rückwärtsspannung führen, die möglicherweise den Durchbruch der pn-Übergangsstruktur verursacht. Unter anhaltender Rückwärtsspannung können lokal hochleitfähige Bereiche entstehen, die mehr Strom anziehen und als Wärme dissipieren. Diese Wärmeansammlung kann zur Bildung lokaler „Hotspots“ führen, ein Phänomen, das bei allen PV-Technologien auftritt. Allerdings variiert der Schweregrad des Rückwärtsspannungsschadens je nach Materialsystem und Gerätearchitektur.

Ein zentrales Zuverlässigkeitsproblem im Zusammenhang mit Rückwärtsspannungsschäden ist die positive Rückkopplung, die *thermisches Durchgehen* (Thermal Runaway) auslösen kann. Eine solche Rückkopplung bewirkt, dass sich im Hotspot bei höheren Temperaturen die elektronische Leitfähigkeit erhöht. Dieser Zusammenhang bildet ein instabiles System in dem rasche Temperaturerhöhungen möglich sind und eine kritische Schwelle überschritten werden kann, ab welcher die Zelle irreversible Schäden erleidet [1].

Dünnschicht-Solartechnologien sind aufgrund ihrer strukturellen und thermischen Eigenschaften besonders anfällig für rückwärtige Vorspannungsschäden. Die in PV-Modulen häufig verwendeten Verkapselungsmaterialien besitzen eine geringe Wärmeleitfähigkeit, was ihre Fähigkeit zur effizienten Wärmeableitung begrenzt. Zudem haben Dünnschichtmodule aufgrund ihrer extrem dünnen Absorberschichten eine geringe thermische Masse, wodurch sie im Vergleich zu konventionellen, waferbasierten PV-Technologien anfälliger für schnelle Temperaturanstiege sind.

Unter den Dünnschicht-Solarzellen ist Kupfer-Indium-Gallium-Selenid (CIGS) aufgrund seines hohen Absorptionskoeffizienten von etwa 10^5 cm^{-1} im sichtbaren Spektrum (400 – 700 nm) [2] besonders vielversprechend. Diese Eigenschaft ermöglicht extrem dünne Absorberschichten (1 – 2 μm) und damit leichte, flexible Anwendungen wie fahrzeug- und gebäudeintegrierte Photovoltaik (VIPV und BIPV) sowie unbemannte Luftfahrzeuge (UAVs) [3, 4]. Wie andere Dünnschichttechnologien ist jedoch auch CIGS anfällig

für Rückwärtsspannungsschäden, da die geringe thermische Masse und die begrenzte Wärmeableitung durch Standard-Verkapselungsmaterialien eine effektive Wärmeableitung erschweren. Ein gut dokumentierter Degradationsmechanismus unter Rückwärtsspannung in CIGS-Solarzellen ist die Bildung sogenannter „wurmformiger Defekte“ [5, 6].

In dieser Dissertation stelle ich ein dreiphasiges Modell zur Beschreibung der Entwicklung von Rückwärtsspannungsschäden in CIGS-Solarzellen vor: die (i) *Keimbildungsphase*, (ii) die *Wachstumsphase* und (iii) die *Wanderphase*. Während der *Keimbildungsphase* führt die thermische Aktivierung des Durchbruchstroms zu einer anfänglichen Instabilität, die ein thermisches Durchgehen auslöst. Diese Phase endet mit einer thermischen Zersetzung, die zur Materialsegregation und Bildung eines leitfähigen, shuntartigen Defekts führt, was den Übergang zu irreversiblen Schäden markiert. In der *Wachstumsphase* dehnt sich der Defekt von der Nano- in die Mikrometer-Skala aus. Schließlich propagiert der Defekt in der *Wanderphase* durch die Zelle und bildet längliche, wurmartige Strukturen.

Zur Untersuchung der *Keimbildungsphase* habe ich eine neuartige Charakterisierungsmethode namens *Laserinduzierte Hot-Spot Lock-In-Thermographie* (HS-LIT) entwickelt, um das Zusammenspiel von Wärmeentwicklung und elektrischer Leistung zu visualisieren und zu quantifizieren. Erste Messungen zeigten, dass laserinduzierte Hotspots eine lokale Leistungsverteilung verursachen, die zu Temperaturanstiegen führt. Um die Messgenauigkeit zu verbessern, wurde eine Lasermodulation eingeführt, die eine direkte Quantifizierung der Verstärkungsfaktor ermöglicht, der das thermische Durchgehen antreibt. Ein thermisches Durchgehen tritt auf, wenn der Verstärkungsfaktor den Wert 1 überschreitet. In einem modulierten Experiment kann das System jedoch zeitweise Verstärkungen über 1 aufweisen, ohne instabil zu werden, was eine zerstörungsfreie Quantifizierung ermöglicht. Dies zeigt, dass das System unter Gleichstrombedingungen instabil wäre.

Experimentelle Ergebnisse bestätigten, dass ein thermisches Durchgehen bei höheren Spannungen wahrscheinlicher ist. Eine kommerzielle CIGS-Solarzelle auf einem Glassubstrat zeigte beispielsweise Schleifenverstärkungen von 1,05, 1, 10 und 2,03 bei Rückwärtsspannungen von 2, 2,5 und 3 V, was einen superlinearen Skalierungstrend demonstriert. Zudem ergaben HS-LIT-Messungen, dass Hotspots in der Nähe der P1-Ritzlinie höhere Verstärkungswerte aufwiesen als jene in der Nähe von P3. Weitere Experimente mit flexiblen CIGS-Modulen auf Stahlsubstraten zeigten deutlich niedrigere Schleifenverstärkungen als Zellen auf Glas, was auf die hohe Wärmeleitfähigkeit des Stahlsubstrats zurückzuführen ist, die eine effektivere Wärmeableitung ermöglichte.

Zur Analyse der *Wachstumsphase* implementierte ich ein gekoppeltes *elektrothermisches Finite-Elemente-Modell* (FEM) mit hoher räumlicher und zeitlicher Auflösung zur Simulation der Defektausbreitung. Das Modell geht davon aus, dass nach dem initialen thermischen Durchgehen ein kleiner ohmscher Defekt entsteht, der durch eine eigene positive Rückkopplung weiterwächst. Simulierte Ergebnisse zeigten, dass ein anfänglicher Defekt mit einem Radius von 10 nm innerhalb von nur 1 ms auf 5 μm anwachsen kann, basierend auf einer Defekt-

widerständigkeit von $R_{\text{def}} = 3,14 \times 10^{-7} \Omega\text{cm}^2$.

Schließlich wurde die *Wandersphase* mit demselben Simulationsmodell untersucht. Ergebnisse zeigten, dass Defekte nahe der P1-Verbindungsline kaum wanderten, sondern entlang der P1-Linie expandierten, während Defekte in der Nähe der P3-Ritzlinie schnell in Richtung P1 propagierten. Ein 10 nm Defekt nahe P3 dehnte sich über eine Länge von $13,5 \mu\text{m}$ innerhalb von $18,5 \mu\text{s}$ aus, getrieben durch die angelegte Leistung. Diese Ergebnisse stimmen gut mit Literaturbeobachtungen überein.

Diese Arbeit bietet ein umfassendes Rahmenwerk zur Charakterisierung und Minderung von Rückwärtsvorspannungsschäden in CIGS-Solarzellen durch experimentelle und modellbasierte Ansätze. Die Ergebnisse unterstreichen den entscheidenden Einfluss von Defektposition und Substratauswahl auf die Zuverlässigkeit von CIGS-Dünnschichtphotovoltaik.

Contents

Abstract	iv
Kurzfassung	viii
List of Figures	x
Notations and Abbreviations	xvi
List of Publications	xvii
1 Introduction	1
2 Fundamentals	5
2.1 Physics of Solar Cells	5
2.2 CIGS Solar Cells	7
2.2.1 Structure	8
2.2.2 CIGS Cells to Module	9
2.2.3 Equivalent Circuit	10
2.2.4 Influence of parallel and Series Resistance on I/V curve	12
2.2.5 Influence of Reverse Bias Conditions on I/V curve	13
2.3 Partial shading in CIGS solar cells	15
2.4 Reverse Bias Damage in CIGS solar cells	16
2.5 Lock-In Thermography (LIT)	22
2.5.1 Black Body Radiation	22
2.5.2 Principles of Lock-In Thermography	25
3 Electro-Thermal loop gain & Hot-Spot Lock-In	29
3.1 Hot-Spot Lock-In Thermography	30
3.2 HS-LIT with CW Laser Source	31
3.2.1 Sample preparation	31
3.2.2 Experimental	31
3.2.3 Results and Discussion	34
3.3 HS-LIT with Modulated Laser Source	37
3.3.1 Sample Preparation	37
3.3.2 Experimental	38

3.3.3	Results and Discussion	40
3.4	Summary	46
4	Analyzing Loop-Gain: The impact of Resistive Effects and the Substrate Thermal Conductivity	49
4.1	The Spatial Distribution of the Loop-Gain: The Impact of Electrode Resistance on the Loop-Gain	50
4.1.1	Location-Dependent Measured Loop-Gain	50
4.1.2	Modeling Loop-Gain. The Impact of Resistive Effects	53
4.2	Flexible CIGS solar cells: the Impact of a Steel Substrate on the Loop-Gain	59
4.2.1	Flexible CIGS solar cells	59
4.3	Summary	66
5	An Electro-Thermal model for Defect Growth	67
5.1	Introduction	68
5.2	Experiments	69
5.3	Simulation	69
5.3.1	The "seed-defect" assumption	69
5.3.2	freefem++	71
5.3.3	Thermal model	72
5.3.4	Electrical model	74
5.3.5	Coupling	77
5.3.6	Discussion	79
5.4	Results	80
5.5	Discussion	86
5.6	Summary	87
6	Impact of Encapsulation, Substrate, and Defect Location on Reverse Bias Damage in CIGS Solar Cells	89
6.1	Impact of Encapsulation	90
6.2	Impact of Substrate	94
6.3	Impact of defect location	97
6.4	Summary	108
7	Conclusions	109
A	Emissivity using FTIR spectrometer	113
	Curriculum Vitae	127
	Acknowledgments	129

List of Figures

2.1.1 Schematic illustration of a) p-type and n-type semiconductors and b) their band bending to form a p-n junction at equilibrium.	6
2.1.2 Schematic illustrations of a p-n junction in a) forward bias. b)reverse bias.	7
2.2.1 Schematic image of CIGS solar cell structure with all layer stack.	9
2.2.2 Schematic image of a CIGS solar module	10
2.2.3 Simplified illustration of the equivalent one diode model representing the behavior of a CIGS solar cell.	11
2.2.4 I/V and power curves of a CIGS solar cell under illumination	12
2.2.5 Schematic illustration of illuminated I/V curves in a linear scale.	13
2.2.6 I/V curve of a CIGS solar cell in dark conditions in linear scale.	14
2.2.7 Schematic illustrations of a p-n junction during a) Zener breakdown. b) Avalanche breakdown, due to reverse bias.	15
2.4.1 A schematic illustration of the heat balance curve leading to thermal runaway.	20
2.5.1 Black-body radiation emittance as a function of wavelength for various temperatures.	24
2.5.2 Lock-in amplifier basic principle.	26
2.5.3 Lock-in process.	28
3.1.1 Schematic illustration of the interaction between local heat and local power dissipation in thin-film solar cells.	30
3.2.1 A CIGS full module with a size of $10 \times 10 \text{ cm}^2$.	32
3.2.2 Schematic illustration of the initial laser-induced Hot-Spot Lock-In Thermography (HS-LIT) setup	32
3.2.3 A screenshot shows the interface of "IRBIS Active Online" software from InfraTec	34
3.2.4 Results of lock-in measurements using the initial HS-LIT setup.	35
3.3.1 CIGS minimodules that are used for the HS-LIT experiments with modulated laser and DC reverse biased voltage.	37
3.3.2 Schematic illustration of updated HS-LIT setup.	38
3.3.3 An actual photo of the updated HS-LIT setup.	39

3.3.4	A screenshot of the interface of the LABVIEW-based control panel that controls most of the optical components in the HS-LIT setup.	40
3.3.5	Results of lock-in measurements using the updated HS-LIT setup.	41
3.3.6	Results of lock-in measurements using the updated HS-LIT setup	42
3.3.7	The loop-gain G_L as a function of reverse voltage V	43
3.3.8	The electrical power amplitude (A_{Pe}) and the overall loop-gain (G_L) as functions of the local temperature of the laser-induced hotspot.	46
4.1.1	Overall loop-gain (G_L) as a function of reverse bias voltage (V), while varying the laser-spot location.	52
4.1.2	Loop-gain (G_L) map for a CIGS solar cell a) small spot b) large spot.	57
4.1.3	Loop-gain (G_L) map for a CIGS solar cell.	58
4.2.1	CIGS cell fabricated on thin stainless steel substrate.	60
4.2.2	Electroluminescence (EL) images of a sample before and after conducting LIT measurements on it.	62
4.2.3	The electrical response, in terms of current, to the applied DC voltage of -2 V is depicted as a function of time.	63
4.2.4	Results of lock-in measurements using the updated HS-LIT setup for a CIGS sample on steel substrate.	64
4.2.5	The overall loop-gain as a function of reverse bias voltage for two different LIT measurements.	64
4.2.6	IV sweep for the tested sample before and after the LIT measurements.	65
4.2.7	Electroluminescence (EL) images for the tested sample before and after conducting LIT measurements.	65
5.2.1	The electrical response of the sample under investigation, including both the applied voltage and the resulting current.	70
5.2.2	Microscopic image of a defect with a radius of $5 \mu\text{m}$ in a CIGS thin film solar cell.	71
5.3.1	An illustrative comparison of a generated mesh before and after refining the area in and around a small defect using "adaptmesh" command in freefem++ simulation tool.	72
5.3.2	Schematic illustration of the mesh for both electrical and thermal models.	73
5.3.3	A comparison in potential distribution between the freefem++ electrical model and a semi-analytical solution.	77
5.3.4	Schematic illustration of the coupled electro-thermal model.	79
5.4.1	a) Temperature distribution profile in the middle of CIGS layer, b) phase plot, c) AZO power profile, and d) CIGS power distribution for the baseline simulation, when the defect has reached a radius of around $0.90 \mu\text{m}$ after $0.126 \mu\text{s}$	81

5.4.2 a) Temperature distribution profile in the middle of CIGS layer, b) phase plot, c) AZO power profile, and d) CIGS power distribution for the baseline simulation, when the defect has reached a radius of around $2.5 \mu\text{m}$ after $5 \mu\text{s}$	82
5.4.3 a) Temperature distribution profile in the middle of CIGS layer, b) phase change plot, c) AZO power profile, and d) CIGS power distribution for the baseline simulation, when the defect has reached a radius of around $6.2 \mu\text{m}$ after 0.55ms	83
5.4.4 Growth of a defect illustrated by the change of the effective radius r as a function of time t for three defect resistance values: $3.14 \times 10^{-5} \Omega\text{cm}^2$ (blue), $3.14 \times 10^{-7} \Omega\text{cm}^2$ (green, baseline) and $3.14 \times 10^{-9} \Omega\text{cm}^2$ (purple).	84
5.4.5 The dissipated electrical power obtained from the electrical model and integrated separately over the Al:ZnO (AZO) layer and the CIGS layer as a function of the defect radius.	85
5.4.6 Growth of a defect as a function of time t due to the change in its initial radius r_0	86
6.1.1 a) Temperature distribution profile at the middle of CIGS layer, b) phase plot, c) AZO power profile, and d) CIGS power distribution, when the defect has reached a radius of around $8.5 \mu\text{m}$ after 0.84ms	92
6.1.2 Growth of a defect illustrated by the change of the effective radius r as a function of time t for various scenarios; baseline (encapsulated, glass substrate, green), (non encapsulated, glass substrate, purple), and (encapsulated, steel substrate, blue).	93
6.2.1 a) Temperature distribution profile at the middle of CIGS layer, b) phase plot, c) AZO power profile, and d) CIGS power distribution, where glass was replaced by steel substrate.	95
6.3.1 A schematic illustration of the modified generated mesh for both electrical and thermal models, when the defect is shifted to P1 scribe line.	98
6.3.2 Cross section in the simulated cell showing the thermal profile and temperature distribution for the layer stack near P1 scribe line.	99
6.3.3 a) Temperature distribution profile at the middle of CIGS layer, b) phase plot, c) AZO power profile, and d) CIGS power distribution, when the defect is located at P1 scribe line.	100
6.3.4 A schematic illustration of the modified generated mesh for both electrical and thermal models, when the defect is shifted to P3 scribe line.	102
6.3.5 A schematic illustration for various regenerated meshes of the electrical model throughout the simulation time.	103
6.3.6 A cross section in a CIGS solar cell showing the thermal profile for the layer stack, when the initial defect of 10nm radius has reached a length of around $5 \mu\text{m}$ at $t = 1.78 \mu\text{s}$	103

6.3.7 a) e) i) m) q) Temperature distribution profile at the middle of CIGS layer, and b) f) j) n) r) phase plot c) g) k) o) s) CIGS power profile, and d) h) i) p) t) AZO power distribution over time, respectively.	104
6.3.8 1) The implied growth rate in term of power and 2) The electrical potential for a defect at three locations: a) the P3 scribe line, b) the center, and c) the P1 scribe line	107
A.0.1 FTIR measurement of EVA layer with an area of $2 \times 2 \text{ cm}^2$ and a thickness of 0.30 mm.	115

Notations and Abbreviations

1D	one Dimensional
3D	three Dimensional
AZO	Aluminum-doped Zink Oxide
BIPV	B uilding I ntegrated P hotovoltaics
CdS	C admium S ulfide
CIGS	C opper I ndium G allium S elenide
CW	C ontinuous W ave
DLIT	D ark L ock- I n T hermography
DUT	D evice U nder T est
EL	E lectro L uminescence
EVA	E thylene V inyl- A cetate
FEM	F inite E lement M ethod
FIB	F ocused I on B eam
FTIR	F ourier- T ransform I nfra R ed
HS-LIT	H ot- S pot L ock- I n T hermography
ILIT	I lluminated L ock- I n T hermography
IR	I nfra R ed
IRT	I nfra R ed T hermography
LIT	L ock- I n T hermography
MPP	M aximum P ower P oint
Mo	M olybdenum
NREL	N ational R enewable E nergy L aboratory
OC	O pen C ircuit
PET	P olyethylene T erephthalate
PL	P hoto L uminescence
PID	P otential- I nduced D amage
PV	P hoto V oltaic
SCR	S pace C harge R egion
SEM	S canning E lectron M icroscopy
SMU	S ource M easuring U nit
STC	S tandard T est C onditions
SC	S hort C ircuit
TCO	T ransparent C onducting O xide
TEM	T ransmission E lectron M icroscopy
VIPV	V ehicle I ntegrated P hotovoltaics
ZnO	Z ink O xide

List of Publications

- S. Nofal and B.E. Pieters, "*A novel non-destructive characterization method to investigate hot-spot formation in CIGS solar cells using lock-in thermography*," IEEE 48th Photovoltaic Specialists Conference (PVSC), pp. 1328-1330, 2021.
- S. Nofal and B.E. Pieters and M. Hülsbeck and C. Zahren and A. Gerber and U. Rau, "*A direct measure of positive feedback loop-gain due to reverse bias damage in thin-film solar cells using lock-in thermography*," EPJ Photovolt, vol. 14, no. 3, 2023.
- S. Nofal, and T. S. Vaas and U. Rau and B. E. Pieters, "*An electro-thermal finite element method (FEM) model for local hotspot kinetics in Cu(In, Ga)Se₂ thin-film solar modules*," Journal of Applied Physics, vol. 136, no. 115102, 2024.

Introduction

Global energy demand is projected to rise significantly, with a nearly 50% increase from 2020 levels anticipated by 2050 [7]. This growing demand, heavily reliant on fossil fuels, poses significant environmental concerns, as fossil fuel combustion releases substantial amounts of carbon dioxide (CO₂) and other greenhouse gases, contributing to global warming. In 2020, fossil fuels accounted for approximately 93% of carbon emissions. International climate agreements, such as the Paris Agreement, aim to limit global warming to below 2°C, underscoring the critical need to transition from fossil fuel to renewable energy sources.

Among these renewable sources, photovoltaics (PV), which directly convert sunlight into electricity, has rapidly become one of the fastest-growing energy solutions globally. The declining cost of solar panels, driven by increased supplier competition, has made solar power increasingly competitive with traditional energy sources. By 2050, solar electricity is expected to provide up to 25% of global electricity production [7]. While traditional silicon-based solar cells dominate the market, alternative technologies such as thin-film solar cells present new opportunities for cost reductions and new PV applications where PV is integrated in infrastructure or vehicles. A particular thin film technology is Copper Indium Gallium Selenide (CIGS) solar cells.

In 2024, CIGS thin-film solar cells achieved a world record efficiency of 23.64% [8]. A key advantage of CIGS technology is its high absorption coefficient, of approximately 10^5 cm^{-1} in the visible spectrum (400–700 nm wavelength range), which allows for the use of very thin absorber layers (1–2 μm) [9–11]. This feature enables deposition on lightweight and flexible substrates, such as polymers and steel. As a result, CIGS modules can achieve high specific power densities, making them particularly attractive for applications in unmanned aerial vehicles (UAVs) as well as vehicle- and building-integrated photovoltaics (VIPV and BIPV, respectively) [3, 4]. Moreover, flexible CIGS has demonstrated its potential in tandem cell applications. In 2020, CIGS achieved a tandem cell efficiency record of 23%, which was accomplished through a tandem cell design that pairs a top flexible semi-transparent Perovskite solar cell with a bottom flexible CIGS cell [12].

The long-term reliability of photovoltaic (PV) technologies is a critical con-

sideration, as PV modules are generally designed to operate effectively for at least two decades. A key challenge that can threaten this longevity is the occurrence of partial shading. When shading affects a solar cell, it generates less current than the surrounding unshaded cells, leading to an imbalance that forces excess current to flow in reverse through the shaded cell. This reverse current can cause a significant build-up of reverse voltage, which may push the cell into junction breakdown. Prolonged exposure to this reverse bias condition can result in the formation of "hotspots," a common issue in PV systems. The extent and impact of reverse bias-induced damage, however, depend heavily on the specific material composition and design of the solar module.

Thin-film solar cells are especially vulnerable to reverse bias-related damage due to their structural and thermal characteristics [13–15]. The encapsulation layers used in most PV modules tend to have low thermal conductivity, which limits the dissipation of excess heat. Moreover, the thin absorber layers in thin-film modules provide minimal thermal mass, making them more susceptible to a rapid temperature increase compared to traditional silicon-based PV technologies. This combination of factors increases the likelihood of thermal runaway in thin-film devices under reverse bias stress.

In CIGS solar cells, reverse bias often induces so-called "wormlike" defects [5]. These defects pose a significant reliability concern, as they act as shunts and degrade the performance of CIGS solar modules [5, 16–18]. Moreover, once these defects appear, they continue to grow and propagate, meandering through the solar cell and potentially causing extensive damage [5].

It is widely believed that positive feedback mechanisms play a crucial role in the formation and evolution of these defects [1]. Specifically, the coupling between Joule heating and thermally activated conductivity creates a self-reinforcing feedback loop. In this process, a localized temperature increase—caused by a highly concentrated current—enhances local conductivity, which in turn further amplifies the current density. This mechanism is inherently unstable, leading to a rapid, localized temperature rise, a phenomenon known as thermal runaway.

Building upon the work of Karpov [1], Nardone *et al.* developed an electrothermal simulation to investigate reverse bias stress in thin-film photovoltaic modules, with a particular focus on shading-induced failures in monolithically integrated CIGS solar modules [19]. In his case study, Nardone *et al.* simulated a CIGS solar minimodule with randomly distributed weak spots to account for the inherent nonuniformity of CIGS material, which is expected to cause thermal inhomogeneity under partial shading. A comparison of his simulation results—with and without electrothermal coupling—identified Joule heating as the primary driver of thermal runaway [19].

However, a fundamental challenge in studying systems with positive feedback is their inherent tendency toward chaos. Small variations in initial conditions are amplified by the positive feedback mechanisms. Consequently, minor inhomogeneities in the material or even random temperature fluctuations can significantly influence the outcome. As a result, the location and exact conditions under which thermal runaway occurs tend to be chaotic, complicating the

study of this phenomenon.

To mitigate the chaos introduced by positive feedback, Vaas *et al.* deliberately induced a hotspot in CIGS solar cells using a continuous wave (CW) laser on the backside of the cell [20]. By precisely defining the hotspot's location, size, and intensity, the controlled laser-induced heating dominates the initial conditions, rendering the system response more predictable. Through this approach, Vaas *et al.* experimentally demonstrated the redistribution of local power dissipation in the presence of a hotspot, thereby visualizing and, to some extent, quantifying the positive feedback effect [20]. However, Vaas *et al.*'s experiments were still destructive, leading to thermal runaway events that caused irreversible damage to the cells, thus limiting further investigation [20].

In this thesis, I aim to study the formation of reverse bias-induced damage. To this end, I distinguish between two key processes: the mechanisms preceding permanent damage and the subsequent evolution of reverse bias damage after an initial defect has formed.

To investigate the pre-damage phase, I build upon the work of Vaas *et al.*, utilizing a laser-induced hotspot to develop reproducible and non-destructive methods for measuring and quantifying the positive feedback effect before permanent damage occurs. This part of the study focuses on the initial stages of hotspot formation.

The second part of this work examines how, once a hotspot has evolved into permanent damage, this damage further develops into wormlike defects. To this end, I develop a coupled electro-thermal Finite Element Method (FEM) simulation model to analyze power dissipation and temperature evolution around a defect. By incorporating a critical temperature threshold for defect formation, the model enables defect growth and propagation through the material. Using this approach, I investigate the mechanisms driving the expansion and meandering of these defects.

Together, these two parts form a comprehensive study of reverse bias defect formation in CIGS solar cells, covering the entire progression from an initially defect-free solar cell to one exhibiting wandering wormlike defects.

To support these objectives, the work presented in this thesis is structured into several chapters. First, **Chapter 2** establishes the fundamental background necessary for understanding the thesis. It begins with an introduction to the principles of solar cells and photovoltaic devices, followed by an overview of the current state of research on reverse bias damage in CIGS solar cells. Additionally, this chapter outlines the characterization methods employed in this study, which will be discussed in detail in subsequent chapters.

In **Chapters 3** and **4**, I focus on the early *non-destructive* stages of hotspot formation driven by the positive feedback effect. Specifically, **Chapter 3** is dedicated to developing a non-destructive characterization technique for quantifying the positive feedback and, consequently, assessing the susceptibility of devices to reverse bias damage. This chapter introduces a novel Lock-In Thermography (LIT)-based method to visualize and quantitatively measure the positive feedback, or loop gain.

Furthermore, **Chapter 4** delves deeper into the factors influencing loop-gain within the CIGS device stack. It examines how various thermal and electrical properties impact loop-gain, including the hotspot location, the presence of shunts within the cell, and the substrate type (i.e., thickness and material).

This investigation provides deeper insights into hotspot formation in thin-film solar modules under reverse bias stress while employing a non-destructive approach.

In contrast, **Chapters 5** and **6** focus on the *destructive* phases of hotspot formation, specifically addressing defect growth and the time scale over which it develops. Although defect growth is also an unstable process driven by positive feedback, the underlying mechanism differs from the initial hotspot formation.

Chapter 5 introduces an electro-thermal Finite Element Method (FEM) model that I developed to investigate the growth mechanism of a pre-existing defect induced by reverse bias stress in CIGS thin-film solar cells. This chapter primarily details the electrical and thermal models, as well as their coupling, while examining the influence of electrical conductivity and initial defect size on the growth process.

In **Chapter 6**, I extend the investigation of defect growth by further developing the coupled FEM model to explore the impact of various thermal and electrical properties within the device stack. This analysis includes examining the effects of encapsulation and substrate layers, as well as the influence of defect location within the cell on its evolution.

Finally, **Chapter 7** summarizes the key findings of this work.

Fundamentals

This chapter provides the essential foundation for understanding the thesis. It begins with an introduction to solar cell physics, followed by a focused examination of CIGS thin-film solar cell and module structure and design. The chapter then explores the critical issue of reverse bias damage caused by partial shading in solar cells. Finally, it presents a comprehensive overview of lock-in thermography (LIT) imaging, highlighting its applications in solar cell characterization. This foundational knowledge sets the stage for the in-depth research and analysis presented in subsequent chapters.

2.1 Physics of Solar Cells

A solar cell is a semiconductor device that converts light energy into electrical energy through the photovoltaic effect. Essentially, a solar cell comprises an absorber, which absorbs light to excite electrons to higher energy levels, and energy-selective contacts. These selective contacts enable the extraction of charge carriers with excess energy, allowing this energy to be harnessed, and then re-inject electrons at a lower energy state [21–25].

The most common method for fabricating an absorber with energy-selective contacts (i.e. a solar cell) is through the creation of a semiconductor p-n junction. In this configuration, the semiconductor serves as the absorber, while the doped n and p regions form selective contacts to the conduction and valence bands, respectively. This setup facilitates the extraction of electrons with excess energy from the conduction band and their re-injection into the valence band at a lower energy state. In this section I give an introduction in the physics of a pn-junction solar cell.

As illustrated in Fig. 2.1.1(a), an n-type semiconductor is formed by doping the material with elements that have more valence electrons than the host semiconductor, resulting in an excess of quasi-free electrons, or negative charge carriers. Conversely, a p-type semiconductor is created by doping the material with elements that have fewer valence electrons than the semiconductor itself, leading to the formation of “holes,” or positive charge carriers [23–25].

Furthermore, as depicted in Fig. 2.1.1(b), when these two materials are

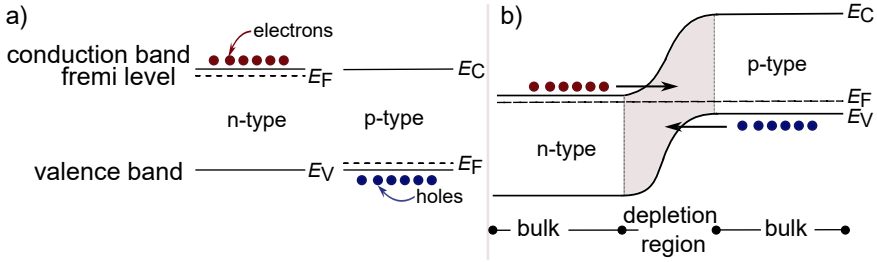


Figure 2.1.1: A schematic illustration of a) p-type and n-type semiconductors and b) their band structure bending to form a p-n junction at equilibrium.

brought into contact, electrons from the n-type region diffuse into the p-type region, while holes from the p-type region diffuse into the n-type region. This diffusion of charge carriers leads to the alignment of the Fermi levels in the n- and p-type regions. The Fermi level represents the energy of the collective electron distribution, so its alignment indicates the averaging of electron energies across the entire device. This alignment of the Fermi levels is also responsible for the creation of the built-in electric field and the formation of the depletion region [23–25].

Since the n-type layer contains a large number of quasi-free electrons in the conduction band, a contact formed with this layer facilitates the exchange of charge carriers between the contact electrode and the electrons in the conduction band. Simultaneously, the low concentration of holes in the valence band limits the exchange of charge carriers with the valence band. Therefore, a contact with the n-type layer effectively establishes a connection with the conduction band. Similarly, a contact with the p-type layer effectively forms a connection with the valence band.

As illustrated in Fig. 2.1.2(a), when the cell is subjected to an external bias, the Fermi level splits into two quasi-Fermi levels, representing the potentials in the conduction band (E_{fn}) and the valence band (E_{fp}). Under a forward bias, the shift in these quasi-Fermi levels reduces the barrier potential and narrows the depletion region, thereby allowing charge carriers to flow across the junction more easily. On the other hand, as illustrated in Fig. 2.1.2(b), when the p-n junction is subjected to a reverse bias, the width of the depletion region increases, and the potential barrier becomes higher. This results in a stronger electric field within the depletion region, which opposes the movement of charge carriers across the junction. A p-n junction thus essentially functions like a valve, allowing current to flow easily in one direction (forward bias) while effectively blocking it in the opposite direction (reverse bias).

Under illumination, the selective contacts ensure that photo-generated electrons in the conduction band are extracted through the n-contact, while electrons are re-injected into the valence band via the p-contact. This process creates a photocurrent. The built-in electric field facilitates the rapid spatial separation of photo-generated charge carriers, reducing the likelihood of recombination between electrons and holes before the electrons can be extracted.

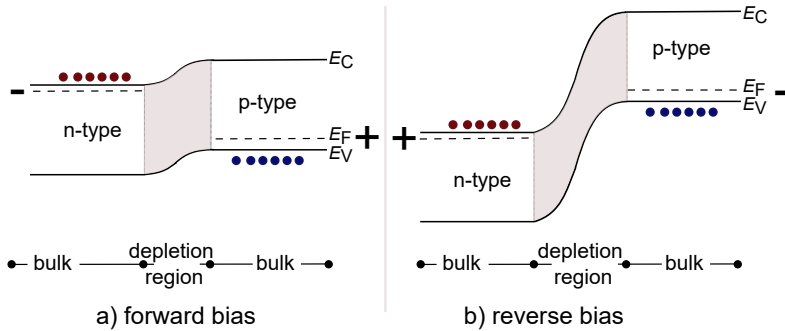


Figure 2.1.2: Schematic illustrations of a p-n junction in a) forward bias. b) reverse bias. When the cell is subjected to an external bias, the Fermi level splits into two quasi-Fermi levels. Forward bias leads to a narrow depletion region allowing current to flow easily, while reverse bias results in a wider depletion region blocking the current in the opposite direction.

However, to extract power, a photocurrent alone is insufficient; a forward voltage is also required. This forward voltage enables power extraction but also reduces the energy barrier and increases charge carrier concentrations, which inevitably leads to higher recombination rates. As a result, there is an optimal operating voltage at which maximum power can be extracted [21, 23, 25].

2.2 CIGS Solar Cells

Copper Indium Gallium Selenide (CIGS) solar cells represent a promising thin-film photovoltaic technology that offers several advantages over traditional silicon-based solar cells. CIGS is a direct bandgap semiconductor material with a high absorption coefficient, allowing it to absorb sunlight more efficiently than silicon [21, 26, 27].

Unlike traditional silicon-based solar cells, CIGS cells are lightweight, flexible, and can be produced with much thinner layers of semiconductor materials. The CIGS layer can be as thin as $1 - 3 \mu\text{m}$, compared to $160 - 190 \mu\text{m}$ for crystalline silicon cells. This reduction in material usage not only lowers manufacturing costs but also allows for a variety of applications, including integration into building materials as Building-Integrated Photovoltaics (BIPV) [26, 28].

One of the key advantages of CIGS technology is its tunable bandgap [21, 26]. By adjusting the ratio of indium to gallium, researchers can optimize the cell's performance for different lighting conditions and applications. This flexibility, combined with its high efficiency potential (with record efficiency reaching 17.6% for a full-sized module of $120 \times 60 \text{ cm}^2$ [29] in 2019, while cells have reached an efficiency of 23.64% [8] in 2024), makes CIGS an attractive option for various solar energy applications.

CIGS technology, while currently occupying a niche in the solar market, offers unique properties that make it a promising candidate for expanding the

reach of solar energy. It is particularly advantageous for integrated PV applications, which include BIPV such as solar roofing and facades, as well as Vehicle-Integrated Photovoltaics (VIPV) and solar pavements. The potential benefits of CIGS for these applications are notable. These include its excellent performance under low-light conditions [30], which is crucial since integrated PV systems are often not optimally oriented towards sunlight. Additionally, CIGS cells exhibit strong mechanical stability; their thin-film nature makes them less prone to cracking, an important factor for durability in integrated systems. Furthermore, CIGS can be manufactured on flexible substrates, enabling seamless integration into curved and irregular surfaces, broadening the scope of where and how solar technology can be applied.

2.2.1 Structure

CIGS is a I-III-VI₂ semiconductor compound consisting of copper, indium, gallium, and selenium (Cu(In,Ga)Se₂) and belonging to the chalcogenide family [21, 24, 26]. Figure 2.2.1a presents a schematic illustration of a typical CIGS thin-film solar cell structure. The cell is composed of several layers: starting with a soda-lime glass substrate, followed by a molybdenum (Mo) back contact, a Cu(In,Ga)Se₂ absorber layer, a cadmium sulfide (CdS) buffer layer, intrinsic zinc oxide (i-ZnO), and an aluminum-doped zinc oxide (AZO) front contact. To protect the cells, typical solar modules additionally have an encapsulation consisting of a polymer, like Ethylene-vinyl acetate (EVA) and a front glass.

Figure 2.2.1b depicts the band diagram of this structure, highlighting the heterostructure formed due to the differences in bandgap energy among the materials used in the various layers. Also indicated is the MoSe₂ alloy, which is naturally formed during the depositing the CIGS on the Mo contact.

Starting from the bottom, the soda lime glass substrate, with a thickness of 3 mm, offers mechanical stability, allowing the module to endure outdoor conditions such as snow [26, 31]. Next, the 1 μm Mo back contact is not only highly conductive but also reflective, reducing voltage loss and enhancing light absorption by reflecting a good percentage of the incident light [32].

Following the deposition of the Mo back contact, a thin p-type Cu(In_{1-x}Ga_x)Se₂ (CIGS) absorber layer is deposited, typically with a thickness of around 3 μm. In this compound semiconductor, the parameter x controls the stoichiometry, varying from 0 (indicating no gallium) to 1 (indicating no indium). The value of x directly influences the electronic properties of the material, allowing for tunable control over characteristics such as the bandgap energy. By adjusting x , the bandgap of the CIGS layer can varied between 1.04 and 1.67 eV [21, 33]. Typically, a bandgap of around 1.15 eV is used for optimal efficiency [34].

The naturally formed MoSe₂ layer has the fortunate side effect it creates a quasi-ohmic contact with the Mo contact layer [35–37], and acts as a back surface field [37], reducing surface recombination.

The n-type layer is formed by a 50 nm CdS layer with a bandgap of 2.42 eV [22, 38], creating the heterojunction with the CIGS absorber. The i-ZnO layer,

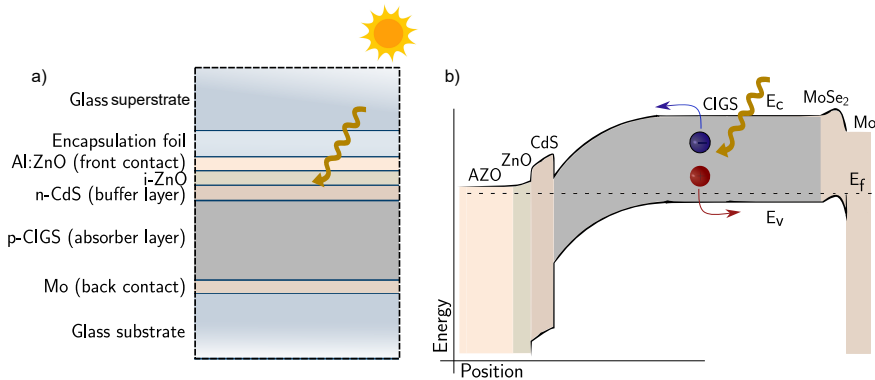


Figure 2.2.1: A schematic illustration of a) CIGS solar cell structure. b) the band diagram of the layer stack. The cell includes a soda lime glass substrate/molybdenum (Mo) back contact/ Cu(In,Ga)Se_2 absorber layer/ cadmium sulfide (CdS) buffer layer/ intrinsic zinc oxide (i-ZnO)/ aluminum-doped zinc oxide (AZO) front contact/ encapsulation foil (EVA). The heterostructure formed due to the different bandgap energies of the material used.

50 nm thick with a resistivity of $2.5 \times 10^6 \Omega\text{cm}$ [24], improves cell performance [39].

The front contact consists of a $1 \mu\text{m}$ thick aluminum-doped zinc oxide (AZO) layer, which is both electrically conductive and highly transparent [21, 40]. Finally, Encapsulation is achieved using EVA and a front glass cover, which adds mechanical stability, acts as an electrical insulator, protects against corrosion, and prevents contamination [26, 41]. In this work the used cells do not have a front glass cover. Instead I typically use an encapsulation consisting of EVA and a polyethylene terephthalate (PET) lamination foil.

2.2.2 CIGS Cells to Module

Solar modules always consist of multiple, series connected cells. The primary reason for this series connection is that the voltage provided by a single cell is rather low (well below 1 V for most solar cell technologies). Thus, to deliver a significant amount of power from a single cell would require a high current, which leads to series resistance losses in the connection toward the cell. It is thus favorable to series connect many small cells, as this increases the voltage of the solar module and decreases the current, allowing the same amount of power transfer at a much lower current, decreasing series resistance losses. In CIGS solar modules, the series connection is typically achieved using a so called monolithic series connection. In this process there are three scribing lines created at different stages between various solar cell deposition processes [42, 43]. The three lines are called P1, P2, and P3, and define the boundaries between cells, as shown in Fig. 2.2.2.

The P1 scribe is the first step, where a laser is used to remove the Mo back

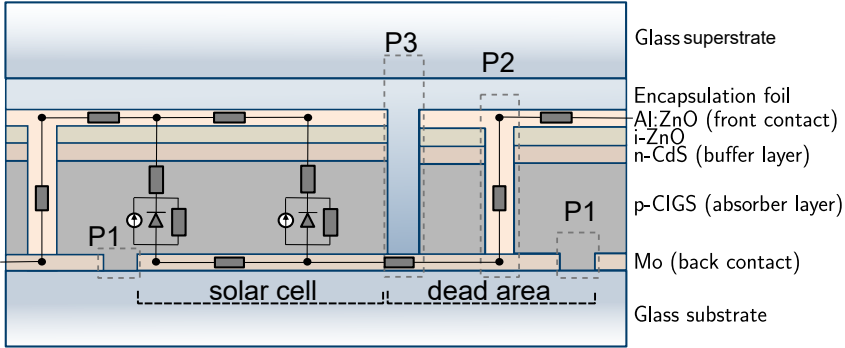


Figure 2.2.2: Schematic image of a CIGS solar module illustrating the three scribing lines (P1, P2, and P3) used to produce a monolithic interconnection between the cells. From left to right, the active area of a solar cell lies between the P1 and P3 lines, while a dead area is produced between the P3 and P1 lines.

contact layer from the glass substrate. This process separates (electrically isolates) the back contacts of the individual cells. Following the deposition of the CIGS absorber and buffer layers, the P2 scribe is performed. This scribe penetrates through these layers to expose the Mo back contact. The subsequent deposition of the AZO front contact fills this gap formed by the P2 line, connecting the front AZO contact with the back Mo contact. The final P3 line is scribed after the deposition of the front AZO and penetrates through the AZO and CIGS layers. This last scribing step separates the front contacts from neighboring cells.

Typically the P2 and P3 steps are performed mechanically, as laser processes tend to damage the CIGS absorber (heat affected zone) [44]. The interconnection area inbetween the P1 and P3 lines is shunted by the P2 line, and is thus not active as a solar cell. For this reason this area is usually referred to as dead-area. Optimized scribing processes try to minimize the width of the dead area.

The scribing processes are somewhat critical. The P1 and P3 lines are most critical as a defect in one of these lines leads to shunting [44]. Defects in the P2 line are typically more benign but may lead to increased series resistance losses [44].

2.2.3 Equivalent Circuit

The one diode model offers a simple yet effective representation for analyzing the behavior of CIGS solar cells. The model is schematically shown in Fig. 2.2.3. It conceptualizes the solar cell as a single diode in parallel with a current source, a shunt resistance, and a series resistance. The current source represents the charge carrier generation, the diode the recombination, and the series resistance the transport losses in both the electrodes as well as in the absorber itself. The shunt resistance can account for localized shunts like scribing defects [21, 22, 24].

Mathematically, the model can be written down as:

$$I = I_{\text{ph}} - I_0 \left[\exp \left(\frac{qV + IR_s}{nk_B T} \right) - 1 \right] - \frac{V + IR_s}{R_p} \quad (2.1)$$

where I represents the total current flowing through the solar cell, V denotes the voltage across its terminals, I_{ph} stands for the photogeneration current, and I_0 signifies the dark saturation current, and q is the absolute value of electron charge. The ideality factor n (i.e. ideally between 1 and 2), Boltzmann constant (k_B), and the temperature (T) further influence the diode current. Finally, the model also incorporates series resistance (R_s) and parallel resistance (R_p) [21, 22, 24, 45, 46]. Note that the equation is implicit and solving it requires numerical methods.

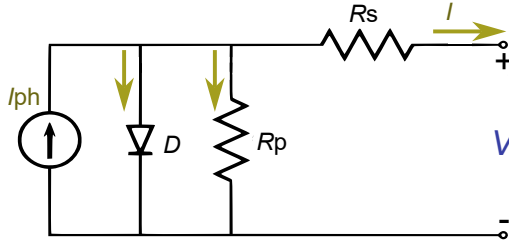


Figure 2.2.3: Simplified illustration of the equivalent one diode model representing the behavior of a CIGS solar cell. The solar cell is represented as a single diode in parallel with a current source and a series resistor, along with a parallel resistance.

The I/V curve of a CIGS solar cell typically exhibits the characteristic shape of a diode curve shifted downward due to photocurrent generation, as shown in Fig. 2.2.4. The curve's shape is influenced by series and shunt resistances, which affect the "squareness" of the curve. This curve passes through three important points:

- Open-circuit voltage (V_{oc}): The voltage at zero current.
- Short-circuit current (I_{sc}): The current at zero voltage.
- Maximum power point (MPP): The point on the curve where the product of voltage and current is maximized (i.e V_{MPP} and I_{MPP} , respectively).

Finally, the fill factor (FF) can be visualized as the ratio of the area of the largest rectangle that fits under the I/V curve ($I_{\text{MPP}} \times V_{\text{MPP}}$) to the product of I_{sc} and V_{oc} .

The power plot, which is overlaid on the same plot as the I/V curve in Fig. 2.2.4 (the curve in dark-red color), shows the power output ($P = I \times V$) as a function of voltage. This curve starts at zero for $V = 0$, rises to a maximum at the MPP, and then falls back to zero at V_{oc} . The power curve peaks at the same

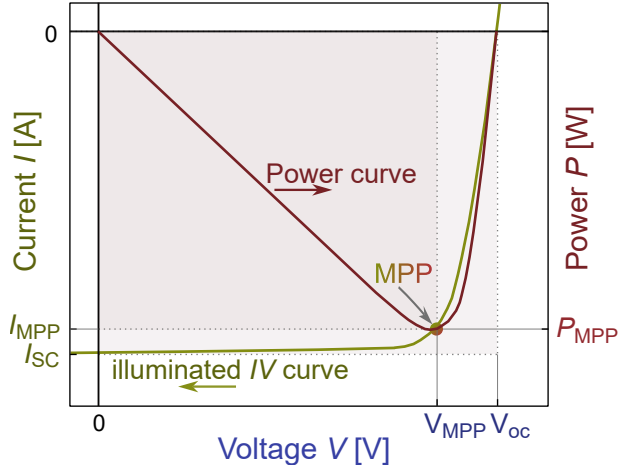


Figure 2.2.4: I/V (in gold) and power (in dark red) curves of a CIGS solar cell under illumination. The I/V curve swipes between open circuit voltage (V_{oc}) and short circuit current (I_{sc}) under illumination, while the power at maximum power point illustrates product of current and voltage at its highest.

MPP, which occurs at a voltage less than V_{oc} and a current less than I_{sc} (i.e. the V_{MPP} and I_{MPP} , respectively). Both I/V characteristics and power output are affected by environmental conditions such as temperature and irradiance, where higher temperatures typically decrease V_{oc} and slightly increase I_{sc} , while higher irradiance increases both I_{sc} and V_{oc} [21, 22, 24].

2.2.4 Influence of parallel and Series Resistance on I/V curve

Parallel and series resistance may significantly influence the performance of a solar cell and the shape of previously discussed I/V curve. Figure 2.2.5 depicts illuminated I/V curves of a CIGS solar cell in linear scale to describe the impact of parallel (Fig. 2.2.5(a)) and series (Fig. 2.2.5(b)) resistances.

Parallel resistance, represents resistance paths within the solar cell, typically due to material defects or imperfections. Series resistance, on the other hand, represents the internal resistance encountered by the current as it moves through the various components of the solar cell, including the semiconductor material, contacts, and interconnections.

As depicted in Fig. 2.2.5(a), the decrease in parallel resistance will lead to a decrease in open-circuit voltage, with a pronounced sharp drop near zero voltage caused by leakage currents. This will result in a decrease in fill factor and the output power. Interestingly, the open-circuit voltage is not affected by the series resistance since no current flows through the cell at that point. However, the increase in series resistance, as illustrated in Fig. 2.2.5(b), causes the I/V curve to bend downward more sharply. This bending results in a reduced fill factor and a shift in the maximum power point due to the increased voltage drop,

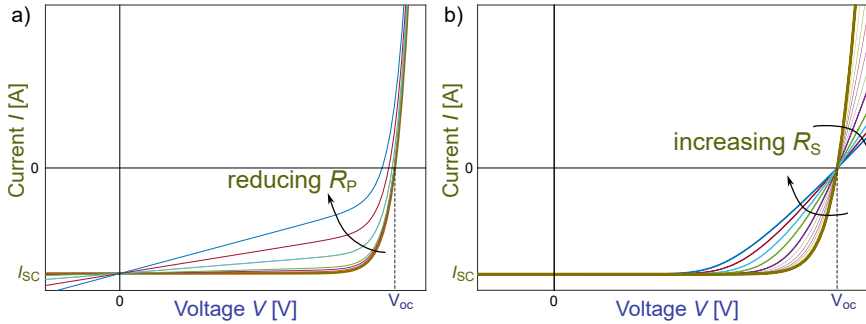


Figure 2.2.5: Schematic illustration of illuminated I/V curves in a linear scale. The curves show the impact of both a) series and b) parallel resistances on the overall shape of a I/V curve, deviating it from the ideal shape (bold dark gold). The decrease in parallel resistance (R_p) causes a decrease in open-circuit voltage (V_{oc}) with a sharp drop in current near zero voltage. The increase in series resistance (R_s) results in slope reduction leading to less fill factor and less output power, but no change in the open-circuit voltage.

ultimately decreasing the overall efficiency of the solar cell [45, 47].

2.2.5 Influence of Reverse Bias Conditions on I/V curve

Figure 2.2.6 depicts an extended version of the linear I/V curve in dark conditions to include the region of reverse bias voltage and current. As depicted in the figure, in forward bias, the I/V curve exhibits a diode behavior similar to what is discussed in Fig. 2.2.4. Under reverse bias the diode effectively blocks the reverse current, making the reverse current dominated by the parallel resistance. However, if the negative voltage reaches a certain critical value, the breakdown voltage V_{br} , the diode starts to become conductive again. This effect is called junction breakdown. There are two primary mechanisms for junction breakdown, as shown in Fig. 2.2.6:

- Zener breakdown: occurs when a strong electric field is applied across a heavily doped p-n junction. This causes electrons to tunnel directly from the valence band to the conduction band through the narrow depletion region, as illustrated in Fig. 2.2.7(a). It typically happens at low voltages (below 5 V) and is characterized by a sharp, well-defined breakdown voltage [21, 24, 25, 48].
- Avalanche breakdown: occurs at higher reverse voltages and involves the acceleration of free carriers in the electric field. These accelerated carriers collide with atoms in the crystal lattice, creating additional electron-hole pairs through impact ionization, as illustrated in Fig. 2.2.7(b). This process multiplies, leading to a rapid increase in current flow [21, 24, 25, 48].

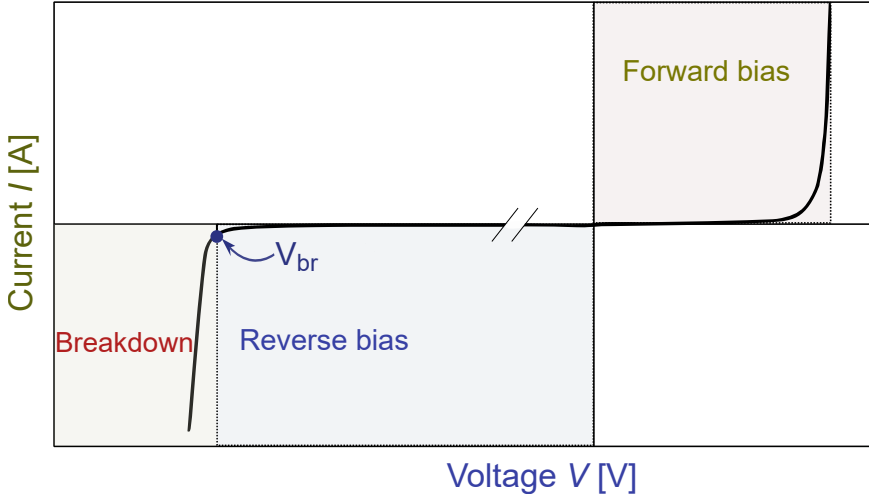


Figure 2.2.6: I/V curve of a CIGS solar cell in dark in linear scale. The I/V curve swipes between forward and reverse bias in dark conditions. In forward, the curve shows a diode behavior similar to Fig. 2.2.4. In reverse, the I/V curve typically shows a very small, relatively constant negative current until a critical voltage (V_{br}) is reached, where the reverse current begins to increase dramatically, indicating the onset of junction breakdown.

Junction breakdown in CIGS solar cells does not match very well with the above described mechanisms. The most striking features of junction breakdown in CIGS are a relatively low breakdown voltage, a strongly temperature dependent breakdown voltage, with a negative temperature coefficient (decreasing breakdown voltage with increasing temperature), and a strong impact of irradiation, where under light the breakdown voltage decreases [49]. At first glance, this best matches with Zener breakdown, which also exhibits low breakdown voltages and a negative temperature coefficient. However, CIGS solar cells are not heavily doped. Moreover, while temperature effects in Zener diodes are relatively small, breakdown in CIGS solar cells is strongly temperature-dependent [49, 50]. Avalanche breakdown, on the other hand, takes place at higher voltages and normally exhibits a positive temperature coefficient, inconsistent with CIGS solar cells. Szaniawski *et al.* [49] suggested trap-assisted tunneling transport through the buffer (Poole-Frenkel tunneling) [49]. This could indeed explain the strong temperature dependency. However, Poole-Frenkel transport alone cannot explain the observed light enhanced breakdown [49]. Thus several open questions remain as to the exact breakdown mechanism.

It is important to note that junction breakdown is inherently non-destructive [21, 50]. However, a prolonged exposure to reverse bias conditions can cause damage to solar cells, in particular due to the local heating induced by the high current densities, which will be further discussed in Section 2.3.

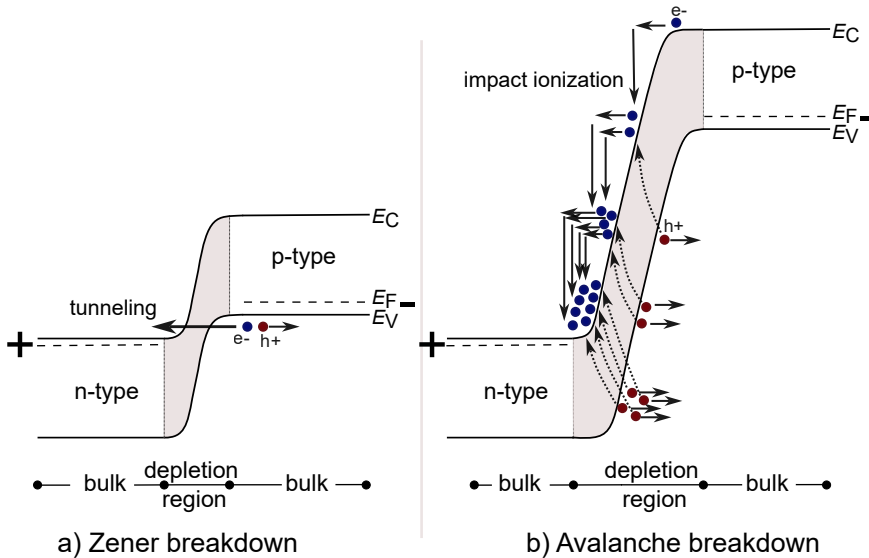


Figure 2.2.7: Schematic illustrations of a p-n junction during a) Zener breakdown. b) Avalanche breakdown, due to reverse bias. (a) A strong electric field enables electrons to tunnel directly from the valence band to the conduction band through the narrow depletion region, resulting in a sharp and well-defined breakdown voltage. (b) Free electrons are accelerated by the electric field and collide with lattice atoms, generating additional electron-hole pairs via impact ionization. This carrier multiplication leads to a rapid increase in current flow.

2.3 Partial shading in CIGS solar cells

Partial shading is a significant issue in commercial photovoltaic (PV) applications. This phenomenon occurs when objects such as buildings, trees, dust, or snow obstruct sunlight from reaching some or all of the solar cells within a module. Although regular maintenance can help mitigate shading, it cannot be completely eliminated [13–15, 21].

A cell which receives less light will produce a lower short circuit current. However, as many cells are series connected, all cells must carry the same current. Thus, the cell producing the least current will limit the current. A solar module typically produces voltages exceeding the breakdown voltage of a singly cell by far. Thus, it may happen that the overall maximum power point current of a module is such that a shaded cell within the module is driven into junction breakdown. This decreases the maximum power point voltage, but largely maintains nearly the same maximum power point current. In this situation the shaded cell do not contribute power but dissipate part of the power generated by the module, leading to the heating of the shaded cells. As the solar cell itself is a thin layer embedded in thermally not very conductive materials (such as EVA and glass), the temperature may rise quickly and lead to thermal damage to the solar cell. Under some conditions such heating effects can be very fast

and lead to permanent damage to solar cells. This reverse bias damage is the topic of the next Section.

2.4 Reverse Bias Damage in CIGS solar cells

In the previous two sections, junction breakdown and partial shading were discussed. These are two important factors in reverse bias damage in CIGS solar cells. In this section the focus is on the state of research on reverse bias damage, highlighting existing gaps and limitations that my PhD work aims to address.

Wormlike Defects in CIGS solar cells

One of the first reports on the effects of reverse bias stress on CIGS solar cell was by Westin *et al.* [5]. Westin *et al.* subjected CIGS thin film PV modules with a size of $10 \times 12 \text{ cm}^2$ to reverse stress for an extended amount of time (15 minutes) and under a bias light of 500 W/m^2 . During this time the current was kept constant and the voltage was monitored. After the stress damage was observed, for which Westin *et al.* coined the term "wormlike" damages. Observation with a thermal camera revealed the damage was caused by small hotspots wandering through the solar cell. Westin *et al.* [5] observed that most damages originate from somewhere in the bulk of the cell but migrated toward the P1 interconnection line. The wormlike damage was reported to reduce the performance by 5 to 10 % (relative). The samples were studied using Scanning Electron Microscopy (SEM) and Energy-Dispersive X-ray Spectroscopy (EDX), revealing the material became porous, there was intermixing of ZnO and the absorber. Westin *et al.* further found that there was phase segregation of an undetermined, copper-rich compound near the back contact [5].

To investigate the origin of these wormlike defects, Johnston *et al.* [51] and Palmiotti *et al.* [52] induced reverse bias stress on CIGS minimodules with cells of $5 \times 100 \text{ mm}^2$ size while using dark lock-in thermography (DLIT). During DLIT imaging, a negative voltage was pulsed while the camera was triggered at the same frequency. However the exact time of the experiments is not mentioned in their work. Although a high voltage of -20 V was applied to the sample, the current was limited to 1.5 mA to prevent uncontrolled thermal runaway events. In the DLIT image, localized heating, or hotspots were identified along the scribe lines. Afterwards, unrestricted current was allowed to prove the possibility of these spots to lead to wormlike defects. Cross sectional images using SEM method detected wormlike defects propagate near the top CIGS interface. Moreover, focused ion beam (FIB) showed voids near the absorber layer and at TCO interface [51–53], aligning with the work from Westin *et al.* [5]. These observations suggest that hotspots formed by reverse bias stress act as the seed for the resulting wormlike defects [51–53]. Nevertheless, there was no clear understanding of the propagation mechanism behind wormlike defects, and the underlying cause of this propagation remains undetermined.

To understand the propagation mechanism, Bakker *et al.* [6, 17] applied reverse bias stress on small CIGS solar cells, measuring $5 \times 7 \text{ mm}^2$, with various

thicknesses of the TCO layer. Half of the cells feature a TCO layer measuring $1\ \mu\text{m}$, while the other half have a thicker TCO layer of $2\ \mu\text{m}$. All cells were subjected to a controlled voltage sweep in dark, applied in reverse direction, while limiting the current to 100 mA. The voltage sweep began at $+0.7\text{V}$ and extended to -10V , with a step voltage of 50 mV and a scan speed of 100 mV/s, which led to from defects in the tested cells. Microscopic images afterwards showed stationary defects in cells with thick TCO layer, but moving defects in cells with thinner TCO. Furthermore, Bakker *et al.* [17] have proposed a propagation model in which he suggests that wormlike defects originate at local weak spots such as mechanically defined edges (i.e. P3 scribe line) and propagate along P1 line [6, 17]. These findings are consistent with earlier discussed results by Westin *et al.* [5] and Johnston *et al.* [51]. Bakker *et al.* [6] have also observed voids at the CIGS/CdS/TCO interface region. SEM-EDX measurements demonstrated a rearrangement of elements in the affected area, with indium, gallium, and copper replaced by cadmium from the buffer layer, and selenium replaced by sulfur. Additionally, SEM images revealed changes in composition inside the defects, including Cu-rich areas and porous compositions, aligning the investigations from Westin *et al.* [5]. [6, 17]

However, the question that remains unanswered is why wormlike defects propagate from the P3 line to the P1 line. To understand the contribution of these interconnections (i.e., P1 and P3 scribe lines) to defects formation, and investigate the differences between the two cell edges, I determine the risk of damage near the edges experimentally in Section 4.1, and I estimate the likelihood of existing defects to propagate as wormlike defects at these edges using electro-thermal simulations in Section 6.3.

In-Field Shadowing Tests

While the mentioned studies so far focused on inducing reverse bias stress on lab-sized cells and minimodules, multiple Literature, on the other hand, has focused on in-field shadowing tests conducted on commercial full size CIGS modules to replicate real-world shadowing conditions that may happen in the field. For instance, Silverman *et al.* [54] have demonstrated a shade test procedure to study the impact of partial shading stress on CIGS modules, which consist of 100 series-connected cells. Their method aims to replicate realistic shading scenarios with 90% shade using an opaque mask to measure the resulted performance loss. Silverman *et al.*[54] regarded the 90% shading scenario as the worst case of shading, since no obstacle can completely obstruct incident light; in reality, some light can always reach the shaded cells. The total light exposure time during the masked flash testing was under 2s, consisting of multiple light pulses of $1000\text{W}/\text{m}^2$, each lasting 100 ms. During the shading tests, all modules experienced permanent damage. Each module lost between 4% and 11% in maximum power due to the formation of localized shunts in shaded areas [54].

However, the study by Silverman *et al.* [54] focused solely on the performance of CIGS modules under a single shading scenario. Alternatively, the research conducted by Lee *et al.* [16] examined the performance of CIGS modules under various partial shading conditions to investigate the effect of bypass diodes

in protecting the cells from partial shading. In their experiments, Lee *et al.* [16] tested modules with 100 series-connected cells that feature different buffer layers, specifically CdS and ZnS, all of which are equipped with bypass diodes. The modules were oriented vertically and subjected to various shading degrees (0% to 100%) using Al foil. Lee *et al.* [16] observed wormlike defects causing permanent damage in shaded PV modules even when bypass diodes were in operation. Transmission Electron Microscopy (TEM) and SEM images revealed porosity between CIGS and ZnO layers, and an amorphous layer above the ZnO layer resulting from molten EVA. Furthermore, these wormlike defects were reported to originate near the P3 scribe line [16], aligning with findings from previously discussed laboratory work from Westin *et al.* [5] and Bakker *et al.* [17]. Additionally, comparisons between modules with CdS and ZnS buffer layers revealed that only modules with a CdS buffer layer exhibited wormlike defects. This correlation is attributed to the thickness of the buffer layers, as CdS buffer layer was thicker compared to ZnS [16].

Several additional studies on shading tests conducted on monolithically interconnected CIGS modules are provided in details by Bakker *et al.* [18], considering wormlike defects as a primary reliability concern. Overall, monolithically interconnected modules do not provide enough protection against partial shading effects. Although external bypass diodes were reported to not provide any significant protection to individual cells from shadow stress, they do help in limiting the output power loss. Therefore, while bypass diodes may not fully mitigate the reliability concerns associated with shading in CIGS modules, they play a crucial role in managing power output during shading events [55]. Additionally, regular cleaning and proper orientation and installation techniques might reduce the likelihood of shading and improving overall efficiency. However, these strategies cannot entirely eliminate the issue.

Time Scale of Defect Formation

An interesting aspect of the defect formation is how fast reverse bias damage develops. Wendlandt and Podlowski [56] conducted short-term shadowing tests on commercial CIGS modules. Each time, 10% of the module was shaded while a 10 ms flash light of 1000 W/m^2 is applied. After each measurement, the shadowing element was moved along the module to a different position and it got flashed again. This process was repeated until every cell in the module had been covered once. This test has resulted in efficiency drop and irreversible degradation in CIGS solar modules within this short period of time. Infrared (IR) images showed many visible defects after shading the modules for a short time [56].

Vaas *et al.* [57] also investigated the impact of short-term reverse-bias stress to study the initial stages of hotspot formation. The experimental work was conducted on CIGS small samples, each consisting of two-series connected cells, with dimensions of $0.4 \times 8.4 \text{ cm}^2$. The procedure involved incrementally increasing voltage pulses until breakdown occurred. Specifically, a single pulse with a duration of 10 ms is applied to the cell, starting at a voltage of -5 V and increasing step-wise amplitude (0.1 V per step) until a defect formed within

the sample. During the experiments, thermographic videos recorded the thermal response, linking it to electrical response. The electrical response indicated that a defect was created in less than 1 ms when a pulse of -13.4 V was applied, while there was no sign of a defect before the reverse bias pulse. In addition, microscopic images have shown that some defects had an elongated trail after the breakdown, suggesting early-stage wormlike defects with the potential to propagate through the absorber layer [57].

Thus various experimental studies indicate that hotspots may develop very rapidly. Through finite element method (FEM) model developed by Nardone *et al.*[19], Guthrey *et al.* [58] have demonstrated that a pre-existing defect (a point-like shunt), of $10\ \Omega$ resistance with a radius of $2\ \mu\text{m}$ in a single cell sized $5 \times 100\ \text{mm}^2$, can cause the thermal runaway within a few seconds at reverse voltages larger than $-3\ \text{V}$ [58]. These results, however, are several orders of magnitude away from the 1 ms observed by Vaas *et al.* [57]. To resolve this discrepancy between model and experiment, I will investigate the time scale for defect formation due to reverse bias damage through electro-thermal FEM simulations in Chapters 5 and 6.

Thermal Runaway and Positive Feedback Loop

Thermal runaway can be understood using the heat balance curve shown in Fig. 2.4.1, which depicts the heat generation and cooling as functions of temperature in systems such as semiconductor devices or batteries. The heat generation curve (plotted in red) typically increases nonlinearly with temperature, reflecting how these systems produce more heat at elevated temperatures due to enhanced current flow or accelerated chemical reactions. In contrast, the cooling curve (in blue) generally rises linearly. The intersections of these two curves represent points of thermal equilibrium. At lower temperatures, the system operates at a stable equilibrium, where any small increase in temperature leads to more cooling than heating, restoring the system to balance. However, beyond a certain critical temperature, this balance reverses: heat generation begins to exceed cooling. This unstable operating point marks the onset of thermal runaway. In this regime, even minor increases in temperature result in disproportionately more heat generation, driving a positive feedback loop.

Thermal runaway, driven by positive feedback loop, is a critical failure mechanism known in various technologies including lithium-ion batteries, semiconductor devices such as bipolar junction transistors (BJTs) and metal-oxide-semiconductor field-effect transistor (MOSFETs), and thin-film semiconductors. Despite the differences in mechanisms and severity, they are all governed by the same principle: thermal coupling to another temperature-sensitive process, whether chemical or electrical, that leads to instability [1, 59–63].

In lithium-ion batteries, thermal runaway is primarily caused by exothermic chemical and electrochemical reactions. Under conditions—such as overcharging, mechanical damage, or elevated ambient temperature—the solid electrolyte interphase (SEI) layer on the anode begins to decompose, releasing heat [59]. This initiates further reactions, including electrolyte oxidation and cathode decomposition, which generate additional heat and gas. As temperature and

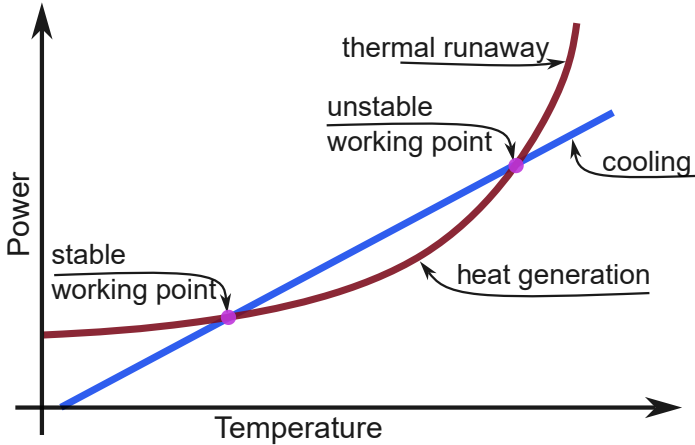


Figure 2.4.1: A schematic illustration of the heat balance curve leading to thermal runaway. The heat generation (red) and cooling (blue) as functions of temperature. The heat generation curve increases nonlinearly, reflecting systems like transistors and batteries, which produce more heat at higher temperatures. The cooling curve rises linearly. The intersection points represent thermal equilibrium, with the system stable at lower temperatures. Beyond a critical temperature, heat generation surpasses cooling, triggering thermal runaway and a positive feedback loop.

pressure rise, a positive feedback loop of heat generation is established, potentially leading to venting, fire, or explosion¹. The positive feedback in this case is chemically driven, where elevated temperatures accelerate reaction kinetics, which further increase heat output [59, 60].

Unlike batteries, thermal runaway in transistors is driven by internal electrical conditions rather than chemical reactions. When a BJT or MOSFET operates at high current densities or under poor thermal dissipation, the junction temperature rises, which in turn increases minority carrier concentrations and increases leakage current. The resulting rise in power dissipation feeds back into the temperature, forming a positive feedback loop that can rapidly lead to device failure if not properly managed [62]. In trench power MOSFETs, for example, localized heating causes a reduction in threshold voltage in hotter regions, increasing local current and exacerbating thermal runaway through current crowding effects [63].

Similarly, a form of thermal runaway can occur in CIGS thin-film solar cells. Unlike the internal electrical or chemical triggers seen in transistors or batteries, thermal runaway in CIGS cells is primarily caused by external factors—specifically, the reverse bias conditions induced by partial shading, as discussed in Section 2.3. When shaded cells are forced into reverse bias to maintain current continuity in series-connected modules, localized power dissipation arises at

¹The explosive potential naturally relates to the amount of stored energy in the system, which can be particularly high for batteries (often hundreds of watt-hours per kilogram [61]).

defects or shunt paths. This localized heating increases current density and reduces local resistance, forming a positive feedback loop that rapidly escalates temperature and leads to thermal runaway.

Theoretical studies have been conducted to develop theories that can explain the mechanisms of reverse bias damage in CIGS solar cells. These theories aim to provide a deeper understanding of the underlying physics involved in the thermal runaway process in thin-film applications. Karpov[1] in their theory describes the interaction of electron transport and heat transfer in thin-film semiconductor structures, providing a comprehensive framework for understanding instabilities such as thermal runaway, hotspots, and reversible thermal breakdown. The model consists of an active conducting layer sandwiched between two thermally insulating layers. The active layer generates Joule heat, and the heat transfer is influenced by the insulating layers. The potential difference across the electrodes is maintained by an external power source, with temperature fixed at the boundaries. This research demonstrates that the interaction between Joule heating and thermally activated conductivity creates a positive feedback loop, leading to instability, commonly referred to as thermal runaway. These instabilities can result in hotspots, characterized by increased temperature and conductivity in localized regions [1].

Building on the theory proposed by Karpov [1], Nardone *et al.* [19] introduced an electro-thermal simulation to analyze reverse bias stress in thin-film photovoltaic modules [19]. Utilizing FEM electro-thermal modeling with COMSOL, they investigated shading-induced failures in monolithically integrated CIGS solar modules. In their case study, Nardone *et al.*[19] examined a CIGS solar minimodule consisting of 20 cells. A shading scenario where 4 out of the 20 cells were fully shaded (replicating a scenario of 20% shading reported by Lee *et al.* [16]) was simulated, with 20 randomly placed weak spots within the module. The model revealed a rapid temperature increase in the weak spots located in the shaded area. Subsequent qualitative comparisons between the simulation with and without the electrothermal coupling indicated that joule heating was the primary contributor at the runaway point. This way Nardone *et al.*[19] demonstrated that weak spots, with a lower breakdown voltage, can rapidly develop into hotspots due to the positive feedback between temperature and breakdown current [19].

A fundamental challenge in systems with positive feedback is their inherent tendency toward chaos. Small initial inhomogeneities are amplified by positive feedback, making such systems highly sensitive to initial conditions. In the case of reverse bias damage, this sensitivity renders the location of thermal runaway events and the threshold for reverse stress unpredictable, complicating efforts to investigate the conditions leading to breakdown. To address the chaos introduced by positive feedback, Vaas *et al.* [20] deliberately created a hotspot in CIGS solar cells using a continuous wave (CW) laser on the backside of the cell [20]. The controlled laser-induced hotspot, with precisely defined location, size, and intensity, dominates the initial conditions, enabling reproducible system responses.

Vaas *et al.* [20] conducted experiments on unencapsulated CIGS samples. In

the initial experiment, only the laser was applied, raising the hotspot temperature to approximately 140 °C. In a subsequent experiment, the laser was initially blocked by a shutter, while reverse stress was applied using a reverse current of 15 mA. During the first 10 seconds of reverse bias alone, the cell heated nearly uniformly, with an observed increase of approximately 0.40 °C. After this initial period, the laser shutter was opened, combining reverse bias and hotspot stress for the remaining 20 seconds. During this phase, the laser-induced hotspot temperature rose rapidly, with thermal images revealing a dramatic increase from approximately 26 °C to over 260 °C in just 3 seconds [20].

These experimental results underscore the role of positive feedback in redistributing electrical dissipation, leading to further heating of the hotspot. The hotspot temperature exceeded 140 °C, the maximum temperature observed under laser stress alone, demonstrating the amplifying effect of positive feedback [20]. Moreover, these findings demonstrate that the conditions under which positive feedback occurs can be systematically controlled. Such control enables targeted experimental investigations into the mechanisms and conditions that trigger thermal runaway, advancing our understanding of system breakdown under reverse bias stress.

The concept of using a laser-induced hotspot makes reverse bias breakdown results more predictable, both in terms of whether a thermal runaway occurs and where it occurs. However, for investigating the conditions leading to breakdown, the experiments developed by Vaas *et al.* [20] remain destructive. In Chapters 3 and 4, I build upon Vaas *et al.*'s results with the goal of developing a non-destructive method. This approach combines pulsed lock-in thermography (see Section 2.5) with a laser-induced hotspot.

2.5 Lock-In Thermography (LIT)

Lock-In Thermography (LIT) is a widely used non-destructive technique for characterizing and analyzing solar cells, enabling efficient failure analysis by identifying defects, hotspots, and performance variations through lock-in correlation and thermal imaging [64–69]. Breitenstein and Langenkamp [64] introduced LIT analysis for detecting defects in solar cells and significantly contributed to establishing it as a versatile tool for solar cell failure analysis and characterization. Today, LIT is an industry standard technique in the field of photovoltaics. In this thesis, LIT analysis forms the foundation of Chapters 3 and 4, hence this section provides a thorough introduction to the technique while its applications in solar cell analysis is described in the subsequent section.

2.5.1 Black Body Radiation

A black body is an idealized physical object that absorbs all frequencies of electromagnetic radiation, including visible light. It exhibits perfect absorption across the entire electromagnetic spectrum, with an absorptivity of 1 at all wavelengths. This characteristic defines it as an ideal absorber.

A black body does not only absorb but also emits radiation across the entire electromagnetic spectrum. According to Kirchhoff's law of thermal radiation there is a reciprocity between absorption and emission. As a result, a perfect absorber is also a perfect emitter, with an emissivity of 1 [21, 64, 70].

Fig 2.5.1 summarizes the fundamental principles governing black body radiation. As illustrated in the figure, the intensity and distribution of radiation emitted by the black body are primarily determined by its temperature. As the temperature increases, the intensity of emitted radiation increases for all wavelengths. Furthermore, the peak of the spectrum shifts to shorter wavelengths, corresponding to higher energy levels. This intensity of radiation emitted by a black body at different wavelengths in thermal equilibrium at a given temperature T , is described by Planck's radiation law

$$I(\lambda, T) = \frac{2hc^2}{\lambda^5} \frac{1}{\exp\left(\frac{hc}{\lambda k_B T}\right) - 1},$$

where $I(\lambda, T)$ is the spectral radiance, λ is the wavelength, h is Planck's constant (6.626×10^{-34} Js), c is the speed of light in a vacuum (3×10^8 m/s), k_B is Boltzmann's constant (1.381×10^{-23} J/K), T is the absolute temperature in Kelvin [21, 64, 70].

Furthermore, Wien's Displacement law correlates the temperature of a black body with the wavelength of the peak in spectral emittance. It states that the wavelength at which the intensity is the highest (λ_{max}) is inversely proportional to the absolute temperature, expressed as:

$$\lambda_{max} T = b,$$

where b is Wien's displacement constant [21, 64, 70].

The Stefan-Boltzmann law quantifies the total energy radiated per unit surface area of a black body as proportional to the fourth power of its absolute temperature. It is described by the equation:

$$E = \sigma T^4,$$

where (E) is the total energy emitted per unit area, and (σ) is the Stefan-Boltzmann constant [21, 64].

However, real objects deviate from ideal black body behavior, emitting radiation with reduced intensity, quantified by emissivity ($\varepsilon < 1$). Consequently, the emissivity serves as a measure of a real body's proximity to black body behavior, adjusting radiation emitted by a real body relative to that of a black body:

$$E_{\text{real}} = \varepsilon \sigma T^4.$$

As a result, the transmittance τ together with the reflectance ρ and the absorbance α of radiation are defined by:

$$\tau + \rho + \alpha = 1.$$

Therefore, for a black body, emissivity is equivalent to absorbance as:

$$\varepsilon = \alpha = 1.$$

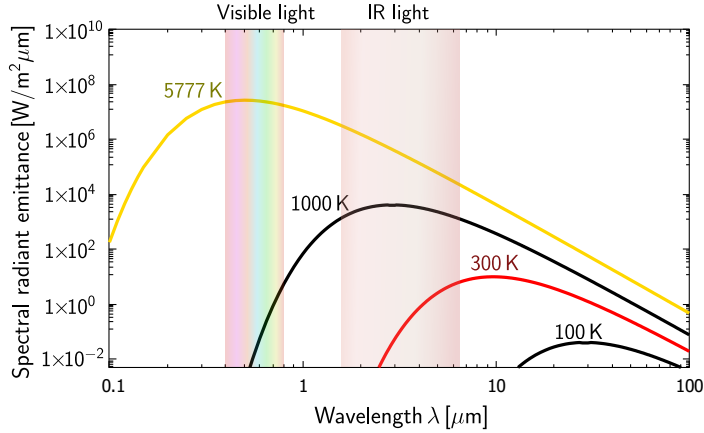


Figure 2.5.1: Black-body radiation emittance as a function of wavelength for various temperatures. Each temperature curve peaks at a distinct wavelength. The intensity and distribution of radiation emitted by the black body are primarily determined by its temperature described by Planck’s radiation law. The wavelength at which the radiation is strongest is given by Wien’s displacement law, and the overall power emitted per unit area is given by the Stefan–Boltzmann law. The Golden curves refers to sun temperature at 5777 K, while red curve corresponds to the earth temperature at 300 K

In this thesis, the real body of interest is a solar cell. A solar cell is designed to absorb light within a specific wavelength range, based on its semiconductor material, and convert it into electrical energy with minimal thermal emission. However, solar cells do emit thermal radiation across a range of wavelengths, with the intensity and spectral distribution of this radiation depending on the cell’s temperature and material properties [21, 64, 65].

The emissivity of a solar cell varies with wavelength. In the visible and near-infrared (NIR) regions, the emissivity is low, allowing the cell to efficiently absorb solar radiation for energy conversion. Conversely, in the mid-infrared (MIR) and far-infrared (FIR) regions, the emissivity is relatively high, enabling the cell to radiate thermal energy more effectively. Notably, defective areas or material inhomogeneities within the solar cell exhibit distinct thermal behavior compared to non-defective regions. This manifests as localized variations in the amplitude and phase of the emitted thermal radiation. The exact emissivity of CIGS solar cells used for the purpose of this thesis will be further discussed and computed in Chapter 3. To detect and map these variations, a thermal camera operating in the IR region is used. The thermal camera captures the IR radiation emitted by the solar cell, enabling detection of defects and inhomogeneities based on the observed temperature variations across the cell’s surface.

2.5.2 Principles of Lock-In Thermography

LIT is an advanced thermographic method which applies Lock-In to enhance the sensitivity and allows a more precise localization of defects in solar cells [64, 65, 71, 72]. LIT analysis is primarily used to extract a small signal embedded in a noisy background by leveraging an active stimulus and synchronous detection. It relies on modulating the heat source (or bias electrical excitation) applied to the solar cell at a specific frequency, typically referred to as the lock-in frequency. By synchronizing the detection system (i.e. an IR camera) with this modulation frequency, signals from other frequencies, including background noise, can be effectively filtered out, enhancing the signal-to-noise ratio and enabling more precise detection of the desired thermal signals associated with the phenomenon under investigation. The high sensitivity of lock-in detection allows LIT to resolve extremely small temperature variations, enabling the detection and localization of defects, hotspots, and material inhomogeneities in solar cells [64, 65, 71, 72].

Figure 2.5.2 illustrates the basic principle of lock-in analysis. The stimulus signal $E(t)$ with the lock-in frequency ($f_{\text{lock-in}}$) causes a thermal response of the solar cell, which is detected by the thermal camera as the measured response signal $F(t)$. However, $F(t)$ is a noisy signal. To extract the lock-in response signal of the system (S) without reduced noise, the following equation is used:

$$S = \frac{1}{t_{\text{int}}} \int_0^{t_{\text{int}}} F(t)K(t) dt \quad (2.2)$$

where t_{int} is the integration time which represent the time of the measurement, and $K(t)$ is the correlation function. The correlation function is a periodic function. Common choices are the square “wide-band” correlation function

$$K(t) = \begin{cases} +2 & \text{for } 0 \leq t < \frac{T}{2} \text{ within one period } T \\ -2 & \text{for } \frac{T}{2} \leq t < T \text{ within one period } T, \end{cases} \quad (2.3)$$

and the harmonic correlation function

$$K(t) = 2 \sin(2\pi ft). \quad (2.4)$$

The choice of correlation function affects the bandwidth of the lock-in procedure.

The integration process in a lock-in amplifier acts as a narrow bandpass filter, selectively preserving signals at the lock-in reference frequency while suppressing noise and other frequency components. This filtering effect arises because the correlation factor, $K(t)$, is a periodic function matching the frequency of the lock-in excitation [64]. When the measured signal—potentially containing both the desired signal and noise components—is multiplied by $K(t)$, only the in-phase components at the reference frequency constructively accumulate over the integration period, T . Meanwhile, noise and signals at other frequencies tend to average out to zero due to their oscillatory nature over the integration window. Consequently, the remaining signal predominantly consists of the desired response and noise components close to the lock-in frequency, while all other noise is effectively rejected.

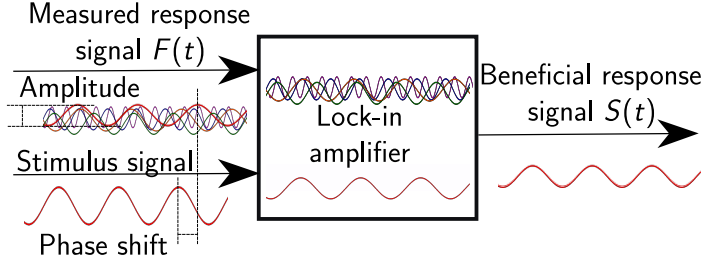


Figure 2.5.2: Lock-in amplifier basic principle. The stimulus signal $E(t)$ represented as the modulated laser is applied to the DUT (with or without a DC voltage) with a specific lock-in frequency ($f_{\text{lock-in}}$ of 0.50 Hz). The stimulus E will cause a thermal response of the DUT that would be detected by the thermal camera. This measured response signal $F(t)$ is a noisy signal. Hence, a lock-in amplifier is used to detect the lock-in response signal of the system (S) with reduced noise.

Often the measured signals are discrete in time (sampled). In this case we can adapt Eq. 2.2 to become a summation expression over the discrete samples within the lock-in period and across multiple lock-in periods. This summation yields the following equation:

$$S = \frac{1}{nN} \sum_{i=1}^N \sum_{j=1}^n K_j F_{i,j} \quad (2.5)$$

where N is the number of lock-in periods, and n is the number of frames within one period. This would mean that each measurement has $n \times N$ number of samples that are averaged.

Often, the response of a system to a periodic excitation may be phase shifted. For this reason it is useful to evaluate the lock-sin signal at different phases. This may be achieved using two correlation functions $K_j^{0^\circ}$ and $K_j^{90^\circ}$

$$K_j^{0^\circ} = + 2 \frac{\sin(2\pi(j-1))}{n} \quad (2.6)$$

$$K_j^{90^\circ} = - 2 \frac{\cos(2\pi(j-1))}{n}, \quad (2.7)$$

where 0° and 90° are the primary phase shifts of a LIT measurement. The phase shift at 0° represents the in-phase signal, and the 90° signal the 90° phase-shifted signal [64].

With these correlation functions two lock-in signals are obtained

$$S^{0^\circ} = \frac{1}{nN} \sum_{i=1}^N \sum_{j=1}^n K_j^{0^\circ} F_{i,j} \quad (2.8)$$

$$S^{90^\circ} = \frac{1}{nN} \sum_{i=1}^N \sum_{j=1}^n K_j^{90^\circ} F_{i,j}. \quad (2.9)$$

With these signals we can now compute the overall amplitude as

$$A = \sqrt{(S^{0^\circ})^2 + (S^{90^\circ})^2}, \quad (2.10)$$

and the phase as

$$\varphi = \arctan\left(\frac{S^{90}}{S^0}\right). \quad (2.11)$$

Breitenstein and Langenkamp [64] played a pivotal role in developing the LIT technique for defect detection in solar cells [64]. In 1988, he introduced LIT to detect weak heat sources caused by current flow inhomogeneities in electronic devices. He applied pulsed voltage while maintaining a constant heat source, enabling the detection of heat dissipation due to cracks or mechanical damage.

When performing LIT on solar cells using the thermal camera, the samples of the signal are referred to as camera frames, and the lock-in procedure is performed for every pixel. This way amplitude and phase images may be obtained. The lock in procedure for thermography is illustrated in Fig. 2.5.3.

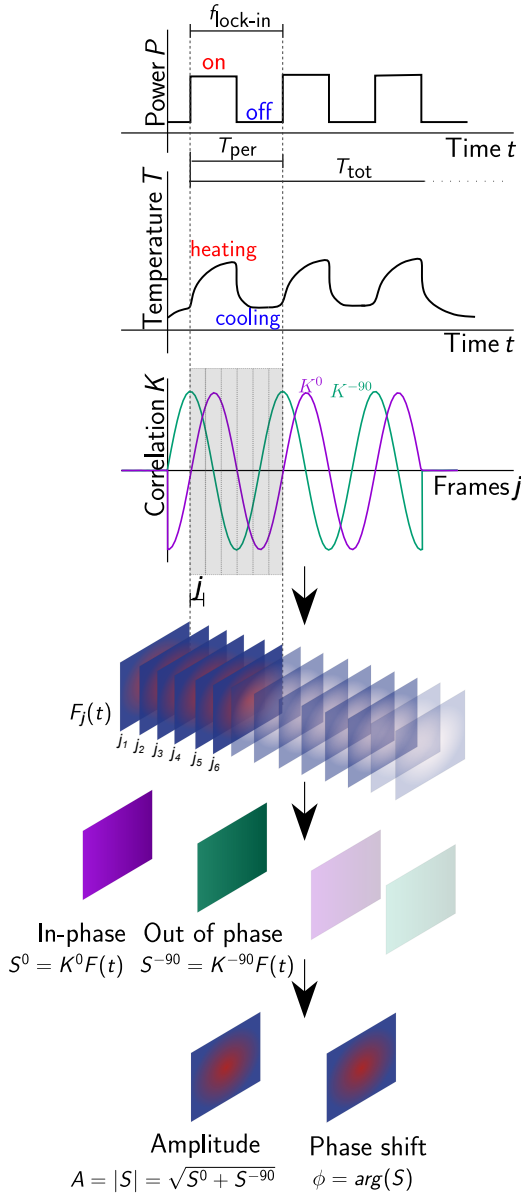


Figure 2.5.3: The lock-in process involves synchronizing the temperature response with the applied excitation source's lock-in frequency. Next, the noisy thermal signal captured by the IR camera is digitized into discrete frames, F_j , and the correlation factor $K(t)$ into discrete values, K_j . Two components of the signal S are computed: the in-phase component S^{0° with no phase shift, and the out-of-phase component S^{90° with a 90° phase shift. This results in the generation of two sets of images: an in-phase image and an out-of-phase image. Ultimately, Lock-in Thermography (LIT) produces an amplitude image and a phase image. The lock-in amplitude A of the beneficial response S for each measurement is calculated as the vector sum of the in-phase and out-of-phase components.

Electro-Thermal loop gain and the Hot-Spot Lock-In (HS-LIT) Method

In this chapter, I aim to develop a non-destructive characterization technique for measuring the susceptibility of devices to reverse bias damage. To achieve this, I have established a method that quantitatively measure the positive feedback loop, or loop-gain. This loop-gain results from the interaction between joule heating, which locally heats the device, and the temperature dependency of the local reverse bias current. This technique builds upon Lock-In Thermography (LIT), introduced in Chapter 2, and is further refined into what I term Hot-Spot Lock-In Thermography (HS-LIT). HS-LIT employs a back-side laser to induce a hotspot in the device. During experiments, either the laser or the reverse bias is modulated, to visualize and quantify the hotspot loop-gain effectively. These results were previously published in references [73, 74].

I first introduce the general principle of HS-LIT in Section 3.1, followed by the first variant of HS-LIT developed in Section 3.2. This initial variant uses electrical modulation, which clearly demonstrates a positive feedback loop but presents challenges in quantitatively interpreting the results. Therefore, the HS-LIT setup was updated to enable the second variant, where the back-side laser is modulated. This latter method has the advantage of directly measuring the loop-gain. This enhanced HS-LIT method is presented in Section 3.3.

3.1 Hot-Spot Lock-In Thermography

Vaas *et al.* [20] have demonstrated that a positive feedback loop exists in Cu(In,Ga)Se₂ thin-film solar cells, where local heating leads to local power dissipation, which in turn leads to reverse breakdown and causes permanent damage [20]. This feedback loop was initiated and triggered during experiments by introducing local heat with simultaneous "hotspot stress" in samples that had no pre-existing local defects [20]. Additionally, it was shown that the size of the local hotspot plays a significant role in the breakdown process, with smaller hotspots being more likely to cause permanent damage than larger ones [20].

The proposed mechanism for this feedback loop is illustrated in Fig. 3.1.1. A small hotspot is present at one location in the solar cell. If the current through the cell is thermally activated (or generally increases with temperature), the local current through the device is enhanced at the hotspot. This, in turn, leads to more Joule heating at the hotspot, further increasing the temperature. Consequently, a positive feedback (i.e., with a loop-gain larger than one) results, which is an inherently unstable condition. In the experiments by Vaas *et al.*, this condition led to thermal runaway, where the local temperature escalates until the device is permanently damaged [20].

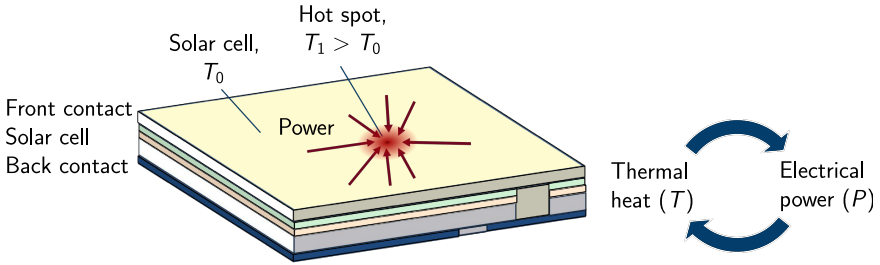


Figure 3.1.1: Schematic illustration of the interaction between local heat and local power dissipation (i.e. positive feedback loop) in thin-film solar cells, where local heating leads to local power dissipation which in turn would lead to a hotter spot.

In this work, similar to the work of Vaas *et al.* [20], a local hot-spot is induced in the solar cell using a laser source while simultaneously applying a reverse-biased excitation. However, my aim is to establish a non-destructive characterization method to study and quantify the positive feedback loop without causing permanent damage to the tested cells. The method by Vaas *et al.* induces conditions where a positive feedback loop is created, making the device inherently unstable and leading to thermal runaway and permanent damage to the cell.

To develop a non-destructive method to measure susceptibility to reverse bias damage, I need to create such unstable conditions while preventing thermal runaway. One way to achieve this is by modulating the experiment. Since thermal runaway requires time to develop, I can create unstable conditions briefly

and then remove them before the system runs out of control. For this reason, I chose to develop a LIT-based characterization method, which is inherently modulated and thus may stabilize otherwise unstable conditions.

3.2 HS-LIT with CW Laser Source

3.2.1 Sample preparation

For my initial HS-LIT experiments, I used solar modules cut from industrially produced semi-fabricated modules (i.e. taken out from a production line before the final contacting and encapsulation). As shown in Fig. 3.2.1, each module has a length of 10 cm and a width of 10 cm, divided into 20 cells that are monolithically series connected, as discussed previously in Chapter 2.2. The structure of a module consists of a 1.1 mm glass substrate with a 1 μm molybdenum (Mo) back contact layer. The CIGS layer stack comprises 3 μm CIGS (produced through a co-evaporation process [75]) and a 50 nm cadmium sulfide (CdS) buffer layer (produced using chemical bath deposition [76]), followed by a 1 μm zinc oxide (ZnO) based transparent conductive electrode layer. All samples were stored in a dark environment before use.

For the experiments I want to contact individual cells. To this end, in every second cell in the module, the CIGS was scratched away and then covered with silver paste, and fitted with silver contact stripes. The silver contact stripes can be seen in Fig. 3.2.1. This process short-circuits the treated cells and contacts the Mo contact. As a result, the untreated cells between the scratched and contacted cells, can be individually contacted. Finally, the modules were encapsulated using ethylene vinyl-acetate (EVA) and a polyester (PET) sheet as a front cover, with a thickness of around 0.3 mm after the encapsulation and lamination processes.

All produced samples underwent testing in the dark and under illumination using a solar simulator. The *IV* sweeps were compared before and after the contacting process to verify that their electrical characteristics were not affected. With this step it is ensured that the new contact does not suffer from a high series resistance.

3.2.2 Experimental

LIT Setup

A schematic representation of the initial setup utilized for HS-LIT experiments is shown in Fig. 3.2.2. The Device Under Test (DUT) is placed on a microscope table in a dark cabinet at room temperature (i.e., 20 °C) to keep out ambient thermal radiation. The laser is directed and focused towards the backside of the DUT via the glass substrate. Since molybdenum is opaque, particularly for lasers in the visible and infrared spectra, no photocurrent was observed from the laser; it only heats the molybdenum layer, which subsequently diffuses into the CIGS layer.

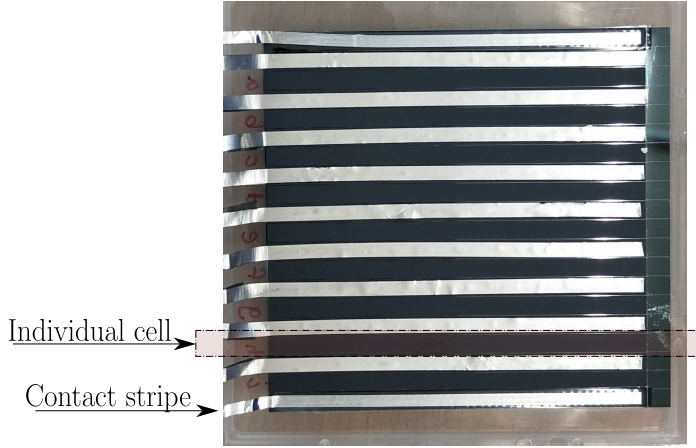


Figure 3.2.1: A CIGS full module with a size of $10 \times 10 \text{ cm}^2$. The series interconnection between cells is cut using silver contact stripes to produce individual cells, each of 8 cm length and 0.40 cm width. Each cell is considered a Device Under Test (DUT) as illustrated in Fig. 3.2.2.

The reverse-bias is applied to the DUT simultaneously with the laser. Meanwhile, a thermal camera is fixed above the microscope table to detect the thermal response of the DUT, identifying hot-spots.

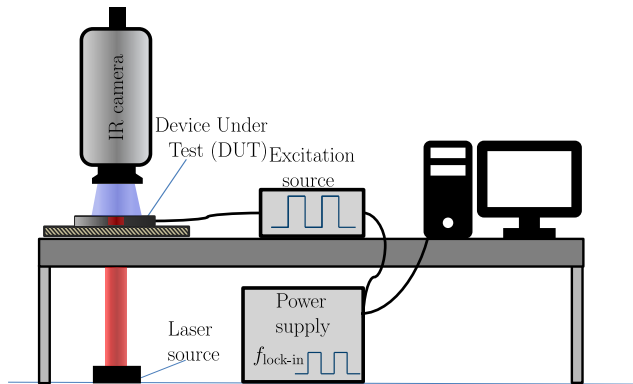


Figure 3.2.2: Schematic illustration of the initial laser-induced Hot-Spot Lock-In Thermography (HS-LIT) setup. A CW laser is pointed to the backside of the device under test (DUT), while a modulated reverse biased current is injected into the DUT simultaneously. A thermal camera is fixed on top to detect the thermal response of the DUT. LIT analysis is made during the experiments using a software from InfraTec GmbH.

The setup is divided into two cabinets. The bottom cabinet contains a red diode continuous-wave (CW) laser with a wavelength of 671 nm and a power of

200 mW. To control the spot size, a $50\times$ objective lens can be moved vertically along the z -axis. The laser beam, with an initial diameter of 1 mm, is focused through the objective lens to achieve a smaller spot size in the micrometer range. A shutter is placed between the laser and the microscopic stage to block the path of the laser beam when not needed. Additionally, the laser is equipped with a safety key mechanism that prevents operation unless the key is switched on.

The top cabinet hosts the thermal camera, an InfraTec ImageIR 9300, which uses an Indium antimonide (InSb) based detector. This camera is sensitive to IR light in the range of 1.5 to $5.5\ \mu\text{m}$. It has a high resolution of 1280×1024 pixels, combining thermal resolution down to 0.025 K with a high frame rate of up to 106 Hz and short integration times of only a few microseconds. Optionally, a close-up lens can be used. The thermal camera is fixed to a motorized vertical stage that is software controlled.

Below the camera in the top cabinet is the microscope table and stage where the DUT is located. This stage moves horizontally along the x - and y -axes and can be manually adjusted. It is equipped with various sample holders for accommodating different types of DUTs. Under the DUT, the table has an opening to the bottom cabinet, through which the laser is applied to the back of the DUT. Each cabinet has its own separate door with safety measures to ensure the laser is off when a door is opened.

To inject a reverse-biased current signal into the DUT, a Keithley 2425 100W Source Measure Unit (SMU) is connected to the DUT in four-terminal sensing mode and synchronized with the lock-in frequency from the thermal camera. Additionally, an oscilloscope is connected to the setup to read the signals (i.e., voltage and current) to and from the DUT. The Keithley is also used to measure an IV sweep of the DUT inbetween LIT measurements to directly detect any changes in device properties, such as damage caused by the experiments.

IRBIS Active OnlineSoftware

A software from InfraTec GmbH, called "IRBIS Active Online", is used to perform the Lock-In Thermography (LIT) measurements. This software controls the camera and the hardware to trigger the external equipment (excitation source). Furthermore, the software performs the Lock-In analysis to determine the phase and amplitude, as detailed in Section 2.5.

As depicted in Fig. 3.2.3, the uppermost bar contains the primary settings related to the thermal camera. Below this bar, four windows display a real-time view from the thermal camera (live image), along with the complex image, amplitude image, and phase image generated post-LIT analysis.

From the menu bar on the left, the lock-in frequency, duty cycle, number of periods, and frame rate can be set before the measurement. For the subsequent experimental work, I employed a lock-in frequency of 0.50 Hz, a duty cycle of 50%, and a frame rate of 40 frames per second. Furthermore, measurements were taken over 100 periods to ensure accurate results.

The IRBIS Active Online software can apply corrections for the used objective if a corresponding calibration file is provided. These corrections include

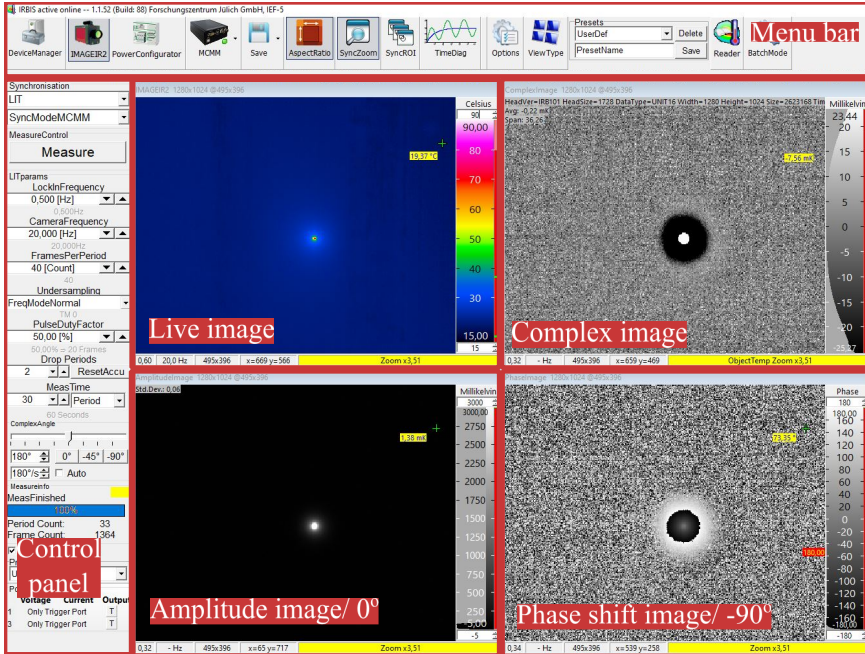


Figure 3.2.3: A screenshot shows the interface of "IRBIS Active Online" software from InfraTec. The software is used during my measurement to conduct LIT analysis. The top bar shows the setting to control the connection to the thermal camera. The left bar is used to control the main LIT parameter such as lock-in frequency, duty cycle, number of periods and the framerate. The remaining widows show the live image from the thermal camera in addition the images produced post-LIT analysis.

a flatfield correction and calibrations with reference black-bodies at various temperatures. Such calibration is required to ensure an accurate temperature response. These calibrations are typically performed by the camera and objective manufacturer. For a single camera and objective combination, various calibration files may be provided for different temperature ranges.

Additionally for this work, I used an SXGA MWIR 300 mm close-up lens to focus on the specific area of interest around the laser-induced hot-spot. The objective lens calibration was selected for the temperature range of 20 – 200 °C. I did not use the emissivity correction provided by the software. Instead, the impact of the sample emissivity is discussed in Appendix A.

3.2.3 Results and Discussion

In Fig. 3.2.4, I show the results for a HS-LIT experiment. The three steady-state thermography measurements are shown in panels (a), (c), and (e) of Fig. 3.2.4. A consistent color scale is used for all steady-state thermographic images.

The lock-in amplitude images, displayed in panels (b), (d), and (f) of Fig. 3.2.4, are presented with the indicated grayscale.

In the first experiment, a modulated, reverse current excitation was applied. Figure 3.2.4(a) shows that the steady-state thermographic image reveals a more or less constant device temperature. The lock-in image shown in Fig. 3.2.4(b) clearly illustrates a thermal response of the cell, where power is dissipated unevenly across the cell area. It is observed that most of the power is dissipated locally along the edge of the cell.

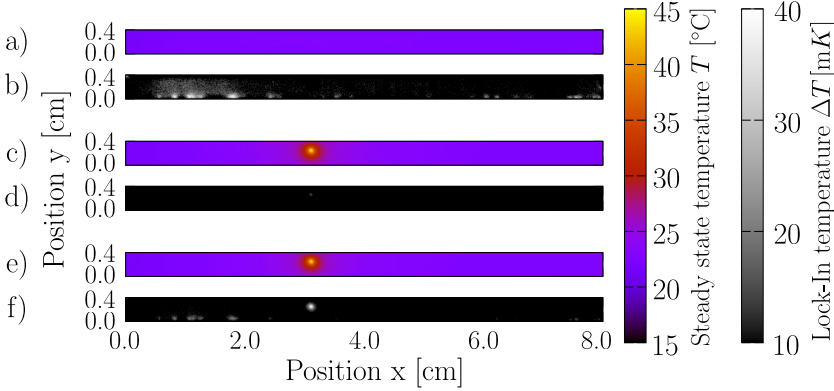


Figure 3.2.4: Results of lock-in measurements using the initial HS-LIT setup. a) steady state thermographic image b) lock-in image of a device when a modulated current excitation is applied in reverse, where most of the power is dissipated along the edge. c) steady state thermographic image d) lock-in image of the device when a CW laser is applied, where a very weak signal appears at the laser location. e) steady state thermographic image f) lock-in image of the device when a CW laser with a modulated current excitation in reverse are applied simultaneously, where a clear signal appears at the laser location due to the interaction between the dissipated power and the hotspot.

In the next experiment, a focused, continuous wave (CW) laser beam was applied to the DUT. No electrical excitation was applied. The steady-state thermographic image in Fig. 3.2.4(c) clearly shows a local hotspot due to the laser excitation. The lock-in image in Fig. 3.2.4(d) shows only a very weak signal at the laser spot. Since no modulated excitation was applied, the absence of a lock-in signal is expected. The weak response is attributed to instabilities of the laser source.

In the final experiment, a CW laser beam and a modulated current excitation were applied simultaneously. In Fig. 3.2.4(e), the steady-state thermographic image shows a local hotspot due to the continuous laser beam excitation. The steady-state temperature distribution is nearly identical to that in Fig. 3.2.4(c), where no electrical excitation was applied. The corresponding lock-in image in Fig. 3.2.4(f) clearly shows a thermal response at the location of the laser-induced hotspot. This response is notably absent in Fig. 3.2.4(d), where the laser was applied without electrical excitation of the device.

The experiment clearly demonstrates the interaction between the temperature profile and local power dissipation in the device. The appearance of the laser hotspot in the lock-in image in Fig. 3.2.4(f), without the laser being modulated, indicates the presence of a positive feedback loop. In this loop, the local hotspot leads to a redistribution of electrical power dissipation, causing the hotspot to become hotter when an electric bias is applied. The magnitude of the lock-in thermal response is thus a direct measure of the hotspot loop gain.

It is important to note that under DC conditions, a positive loop-gain cannot be measured because any small excitation would lead to an infinite response, causing the temperature to increase until the device fails. However, in this experiment, I demonstrate the existence of a positive loop-gain without the temperature increasing uncontrollably. This is because the periodic excitation interrupts the temperature rise. In other words, the slow response of the thermal system allows us to demonstrate the existence of a positive loop gain without damaging the device.

The aim is to quantify the loop-gain. Under DC conditions, this is not possible, as any small signal leads to an infinite response. However, with a modulated excitation, the loop-gain can be quantified. To achieve this, I need a lock-in response for the laser excitation, meaning the laser must be modulated. This experiment is the focus of the next section.

3.3 HS-LIT with Modulated Laser Source

In this section, a modified HS-LIT setup is introduced, which is capable of modulating the laser-induced hotspot, thereby enabling the quantification of the positive loop-gain. The quantification of the loop-gain (i.e., values higher than 1.0) provides a direct measure of the thermal system's instability. The key alterations made to the previous HS-LIT setup are outlined, and their impact on the measurements is detailed.

3.3.1 Sample Preparation

Similar to the samples discussed in the previous section (Section 3.2.1), the samples in this section are cut from industrially produced $\text{Cu}(\text{In,Ga})\text{Se}_2$ semi-modules, which consist of a $\text{ZnO}/\text{CdS}/\text{CIGS}/\text{Mo}/\text{Glass}$ layer stack. The layout and size of the samples is slightly different from those in Section 3.2.1. As shown in Fig. 3.3.1, each sample consists of many individual minimodules on a $10 \times 10 \text{ cm}^2$ glass substrate. The mini-modules, in turn, consist of ten series-connected solar cells, each with dimensions of $0.4 \times 4 \text{ cm}^2$. The cells are monolithically interconnected. As in Section 3.2.1, every second cell was scratched, and contact strips were applied to obtain individually contacted cells for the experiments. All samples are encapsulated using an EVA layer and a polyester (PET) layer as a front cover with a thickness of 0.20 mm after lamination (i.e. the encapsulation layer for this set of samples is thinner compared to those of Section 3.2 due to changing the pressure in the lamination process). Finally, the mini-modules were tested using *IV* sweeps before and after making the contacts using the Keithley 2425 SMU.

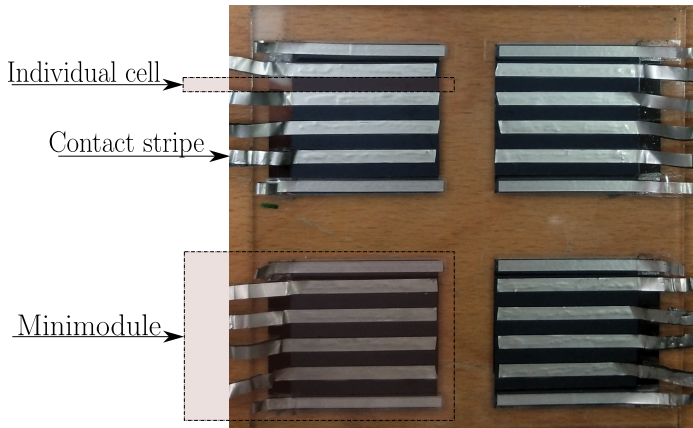


Figure 3.3.1: CIGS minimodules that are used for the HS-LIT experiments with modulated laser and DC reverse biased voltage. Each sample has 4 minimodules. The interconnection between cells in each minimodule is cut to produce individual cells. Each cell in each minimodule is 4 cm length and 0.40 cm width and considered as a Device Under Test (DUT).

3.3.2 Experimental

LIT Setup

The primary update in the HS-LIT setup has been focused on the bottom cabinet containing the laser source and optics. For reference on the setup before the update, see Section 3.2.2. The laser source was replaced with a higher power model, necessitating stricter safety measures. As shown in Fig. 3.3.2, the laser source is now modulated, while the electrical excitation of the DUT is now in DC condition.

Figure 3.3.3 shows an image of the updated HS-LIT setup. The new laser integrated into the setup is a Cobolt CW diode laser from HEUBNER Photonics Group GmbH. This laser is known for its stability and high power, with a maximum output of 2 W and a wavelength of 1064 nm. A half-wave plate is attached to a polarized beam splitter directly after the laser source. By adjusting the polarization of the beam splitter through the half-wave plate, the laser power can be conveniently controlled and reduced. A beam damper is fixed to the beam splitter to reject the reflected polarized light. For automatic rotation, the half-wave plate is mounted on a rotation mount connected to an interface board. The rotation is powered by two elliptic piezoelectric resonant motors. The system is operated using the ELLO software provided by THORLABS GmbH. This setup allows for precise control over the laser power, ensuring safe and efficient operation while also providing a convenient software control interface.

For the modulation of the laser, an optical chopper is integrated in the system. The chopper is used for modulating the laser in the frequency range of 1 – 100 Hz. I found the synchronization of the chopper with a trigger becomes unstable for frequencies below 1 Hz. For this reason, the optical shutter is used

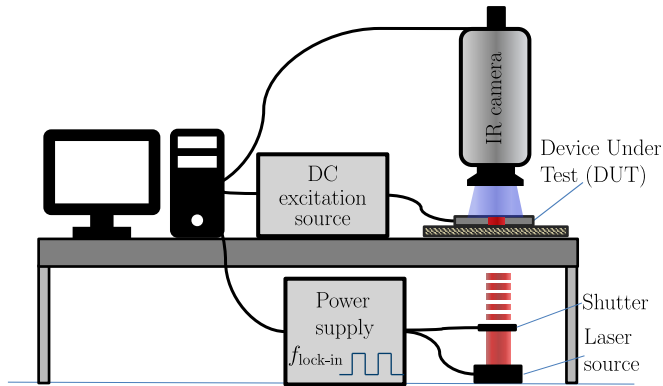


Figure 3.3.2: Schematic illustration of updated HS-LIT setup. A laser is modulated and pointed to the backside of the Device Under Test (DUT), while a DC reverse biased voltage is applied to the sample. A thermal camera is fixed on top to detect the thermal response of the DUT. LIT analysis is conducted during the experiments via the software from InfraTec.

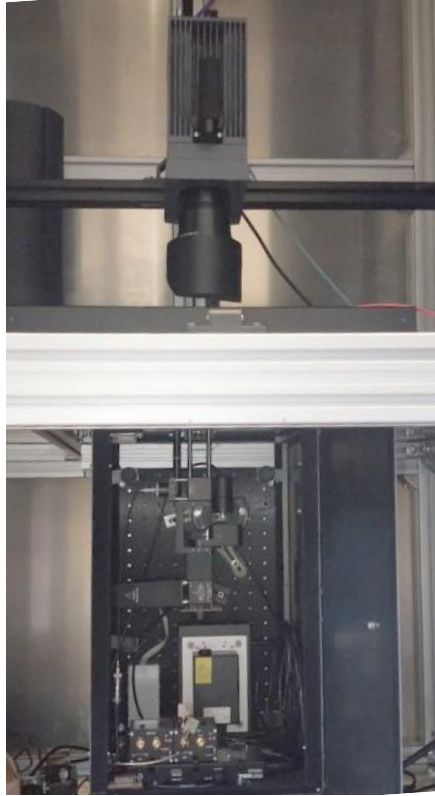


Figure 3.3.3: An actual photo of the updated HS-LIT setup. The setup consists of two cabinets. The top cabinet hosts the thermal camera and a microscopic stage where the Device Under Test (DUT) is placed. The bottom cabinet includes the new laser source with all its required optical components. The new laser is a Cobolt CW diode laser with a maximum output of 2 W and a wavelength of 1064 nm.

to modulate the laser for $f_{\text{lock-in}} < 1.0$ Hz. Both the shutter and the chopper are synchronized to the lock-in setup. The shutter also serves to block the laser on the DUT when the laser is not needed.

The laser beam, with a 1 mm diameter, is focused down to a $5 \mu\text{m}$ diameter on the DUT (i.e., the size of the laser-induced hotspot) using a $20\times$ objective lens. This objective lens is mounted on an xyz -translator, where the xy -translator is used for laser alignment, while the z -translator is connected to an actuator for adjusting the vertical distance between the objective lens and the sample to control the laser beam's focus. The actuator is automated using a K-cube brushed DC servo controller (KDC101). The z -translator allows for easy automatic movement, with a range of 12.0 mm, while the objective lens has a working distance of 6 mm. All optical components mentioned in this section are from THORLABS. Finally, a control panel was developed using LABVIEW

to control all optical components through a single interface, as shown in Fig. 3.3.4.

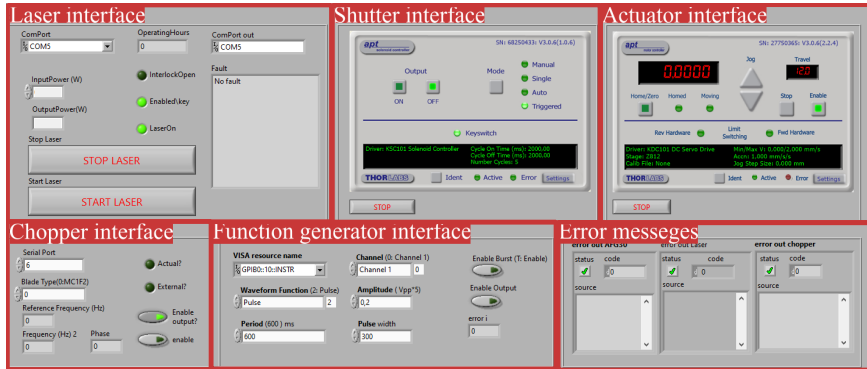


Figure 3.3.4: A screenshot of the interface of the LABVIEW-based control panel that controls most of the optical components in the HS-LIT setup.

Similarly to Section 3.2.2, lock-in amplitude and phase images are produced using the InfraTec GmbH "IRBIS Active Online" software. For this work, a laser power of 50 mW is used and modulated according to the desired lock-in frequency from the thermal camera. The lock-in frequency for these experiments was set to 0.50 Hz, and thus the shutter was used to modulate the laser. The duty cycle is set to 50%. Measurements are acquired over 30 periods, with the first two periods dropped to reject initial transients. The framerate of the camera is set to 40 frames/period. The electrical response is recorded using the SMU 2425, while a DC electrical excitation is applied in reverse. In addition, the electrical characteristics of the DUTs are characterized by means of a dark IV sweep that covers a voltage range between -0.20 V and $+1.20$ V before and after each experiment, using the same SMU 2425.

3.3.3 Results and Discussion

Quantification of the Loop-Gain

In Fig. 3.3.5, both the steady-state temperature and lock-in amplitudes are illustrated. It is essential to note that in HS-LIT experiments, I employed a modulated laser to examine the thermal behavior of CIGS solar cells. However, due to challenges in capturing live thermal images of the modulated laser, the steady-state temperature image shown in Fig. 3.3.5(a) was obtained using a continuous wave (CW) laser operating at the same power as the modulated laser without electrical excitation, and this was done solely for visual reasons. The lock-in amplitude without electrical excitation is presented in Fig. 3.3.5(b), whereas Fig. 3.3.5(c) displays the lock-in amplitude with electrical excitation. As previously mentioned, a color scale represents the steady-state images, while the intensity of the lock-in images is shown in grayscale.

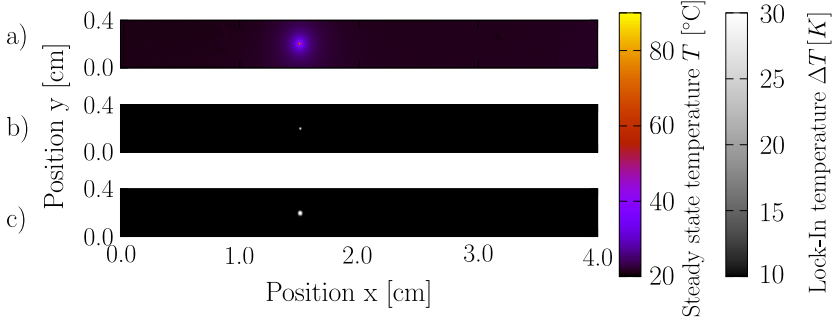


Figure 3.3.5: Results of lock-in measurements using the updated HS-LIT setup. a) steady state thermographic image b) lock-in image of a sample when only the modulated laser is applied, where a clear signal appears at the laser location c) lock-in image of the sample when the modulated laser with a DC reversed voltage are applied simultaneously, where a brighter/wider signal appears at the laser location due to the interplay between the hotspot and the dissipated power.

The steady-state image in Fig. 3.3.5(a) shows the laser hotspot and the heating of the region around the hot-spot due to lateral heat diffusion. Figure 3.3.5(b) shows the corresponding lock-in image, where the lock-in intensity is high only at the very center of the hotspot while it is almost zero anywhere else within the cell. This highly localized response is anticipated, as it indicates that only the heat generated directly by the laser during the lock-in period is captured in the lock-in signal. The lateral heat diffusion that occurs during the lock-in period does not contribute to this measurement, resulting in a very localized detection of the laser hotspot [64, 66]. The spot has a maximum lock-in amplitude of 38.295 K (i.e. the amplitude in this case is order of magnitudes higher than amplitudes in the previous section, which was only in millikelvin range).

In Fig. 3.3.5(c), the lock-in signal is shown for a simultaneous bias of -3 V. A maximum lock-in amplitude of 63.873 K is observed, and the hotspot is notably larger. Since the applied voltage is DC, this increase in the thermal response is due to the interaction between the modulated laser hot spot and the applied biased voltage. As the lock-in frequency remains the same, and hence the spatial resolution is unchanged, the increased size implies that the electrical power is modulated in a wider region around the hotspot. This is attributed to the effects of current crowding.

The local hotspot loop-gain (g_L) is defined as the ratio between the lock-in amplitude with and without electrical excitation.

$$g_L = \frac{A_{1e}}{A_1}, \quad (3.1)$$

where, A_{1e} is the amplitude with modulated laser *and* DC electrical excitation, and A_1 with modulated laser only.

As the size and shape of the hot-spot are different, I define the overall loop-gain as

$$G_L = \frac{\iint_{\Omega} A_{ie} d\Omega}{\iint_{\Omega} A_i d\Omega} \quad (3.2)$$

where, Ω denotes the cell area within the lock-in amplitude images. In my experiment shown in Figure 3.3.5, the overall loop-gain of the hotspot reaches 2.03 and the maximum local loop-gain equals 1.67.

To gain better understanding of the thermal response due to the applied electrical excitation, in Fig. 3.3.6 I zoomed-in on an area of 0.4×0.6 cm around the hot-spot, where the amplitude and phase shift for both scenarios from Fig. 3.3.5 are depicted. The lock-in measurements without electrical excitation are shown in Fig. 3.3.6(a) and (b), depicting amplitude and phase shift, respectively. Figures Fig. 3.3.6(a) and (b) present the corresponding measurements with electrical excitation. All shown in grayscale.

In both scenarios - with and without electrical excitation - the lock-in amplitude signals peak at the center of the hotspot, corresponding to an in-focus phase shift (i.e., phase shift = 0) at that location. Moving away from the cen-

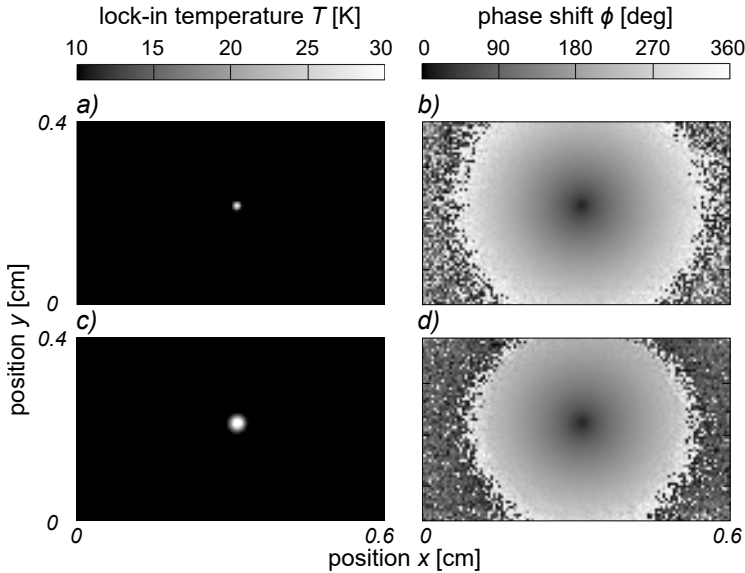


Figure 3.3.6: Results of lock-in measurements using the updated HS-LIT setup. a) lock-in image and b) phase shift of a sample when only the modulated laser is applied. c) lock-in image and d) phase shift of the sample when the modulated laser with a DC reversed voltage are applied simultaneously. Without the electrical input, the lock-in amplitude signal is lower and narrower, and the area showing phase delay (phase shift > 0) is large. Meanwhile, for a higher and wider lock-in amplitude signal, due to the applied electrical excitation, the central point has a wider in-focus phase shift, while the surround area exhibiting phase delay decreases.

ter, positive phase shifts indicate the extent of lateral heat diffusion within the measurement timeframe. As shown in Figure Fig. 3.3.6(a) and (b), without the electrical input, when the lock-in amplitude signal is lower and narrower, the area showing phase delay (phase shift > 0) is large. Meanwhile, for a higher and wider lock-in amplitude signal, due to the applied electrical excitation, the central point has a wider in-focus phase shift, while the surround area exhibiting phase delay decreases, as depicted in Figure Fig. 3.3.6(a) and (b).

This contrast suggests that electrical excitation leads to a more intense and spatially extended thermal response, as evidenced by the amplified lock-in signal. Interestingly, this stronger thermal event results in a smaller region of detectable phase shifts, indicating a more rapid and localized heat diffusion process.

I repeated the HS-LIT experiments on the same cell, where I varied the DC reverse voltage, whilst all other experimental parameters are kept the same. The overall loop-gain for these experiments are presented in Figure 3.3.7. The results show a highly super linear loop-gain with the reverse bias voltage. The line in 3.3.7 is an exponential fit, which I add as a guide to the eye. Attempts to measure the response to higher reverse bias voltages resulted in the destruction of the sample.

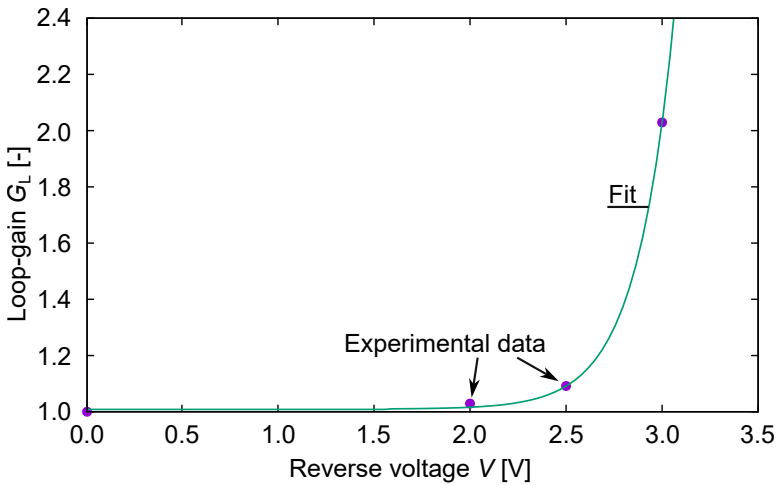


Figure 3.3.7: The loop-gain G_L as a function of reverse voltage V . During the HS-LIT experiments the laser source is modulated with constant power while the applied voltage is increasing gradually. Loop-gain is increasing exponentially w.r.t the applied reverse biased voltage. The maximum recorded over-all loop-gain is 2.03 at voltage of -3 V.

Electro-Thermal Loop-Gain and dissipated Power

As in my experiment I measure a lock-in response of the system to the laser and electrical power, I should be able to relate the measured electrical power to

the absorbed laser power. In the following I verify the consistency of my measurement by comparing the measured electrical response and the laser power, i.e. I check whether I can account for all the modulated heat in the system. From the measured electrical power I can compute the lock-in amplitude. The 0° and 90° lock-in signals (F^{0° and F^{90° , respectively) equal

$$F^{0^\circ} = 2P(t) \sin(2\pi ft) \quad (3.3)$$

$$F^{90^\circ} = 2P(t) \cos(2\pi ft), \quad (3.4)$$

where t is the time, and $P(t)$ is the measured injected electrical power. The electrical power amplitude (A_{Pe}) then equals

$$A_{Pe} = \sqrt{(F^{0^\circ})^2 + (F^{90^\circ})^2}. \quad (3.5)$$

Likewise, I may define the laser power amplitude (A_{Pl}) as the lock in amplitude of the absorbed laser power. The laser power is modulated as a square wave with a duty cycle of 50%. For the absorbed laser power I can write

$$P_l = P_{0,l} \alpha \operatorname{sgn}(\sin(2\pi ft)), \quad (3.6)$$

where, α is the absorbance of the laser in the molybdenum, $P_{0,l}$ the incident laser power and sgn is the sign function (i.e. $\operatorname{sgn}(\sin(2\pi ft))$) is a square wave. Applying Eqs. (3.3), (3.4), and (3.5) to Eq. (3.6), I obtain

$$A_{Pl} \approx 1.2719 P_{0,l} \alpha, \quad (3.7)$$

where I computed the amplitude of the unit square wave with the parameters for the experiment, namely 40 samples per period (the same as the number of frames per period). The value of 1.2719 is close to the theoretical $4/\pi \approx 1.2732$, which is the amplitude of the ground frequency of a square wave.

The definition of the loop-gain in Eq. (??) implies the loop-gain may also be written as

$$G_L = \frac{A_{Pl} + A_{Pe}}{A_{Pl}}, \quad (3.8)$$

as the integrated lock-in signal should be proportional to the total dissipated lock-in power.

For the electrical power amplitude during the experiment I find $A_{Pe} = 16.4 \text{ mW}$, and for the gain I had $G_L = 2.03$. Thus, using Eq. (3.8) I find $A_{Pl} = 15.92 \text{ mW}$. The laser power was set to 50 mW . However, I have optical losses in the half-wave plate, which reduces the incident laser power to $P_{0,l} = 43 \text{ mW}$. I thus can compute the absorbance of the laser as $\alpha = A_{Pl}/(1.2719 P_{0,l}) = 0.29$. For comparison I can compute how much absorbance I would expect for a laser with wavelength 1064 nm incident on a Air/Glass/Mo optical system. To this end I assume a refractive index of glass of 1.5 [77]. For the molybdenum I assume a complex refractive index of $n_{\text{Mo}}^* = 2.3016 + 4.4153i$ [78]. From this I obtain an absorbance of $\alpha = 0.25$. The deviation between the computed and the theoretical absorbance is likely due to

different optical properties of the Glass/Mo interface. This calculation shows that the various measured quantities are consistent and demonstrate that the measured thermographic loopgain indeed implies the same loop-gain in terms of overall laser and electrical power dissipation.

Discussion

If I consider the measured loop-gain of 2.03 in the hotspot, it implies an amount of dissipated heat in the hotspot is amplified 2.03 times within the 1 second "on-period" of one lock-in period (the laser is modulated at 0.5 Hz with a 50 % duty cycle). Thus the implied temperature rise under DC conditions is exponential with a doubling of the temperature every second. It must be stressed that this loop-gain is obtained at the specific conditions of the measurement, i.e. under DC conditions it is to be expected the loop-gain will change over time as the hotspot gets hotter and bigger. However, the measured loop-gain of 2.03 does constitute a massive instability, which is likely to cause a thermal runaway and irreversible damage to the sample in a short period of time.

Impact of Hot-Spot Temperature on Electrical Response

In the previous subsection, I studied the voltage dependency in the local hotspot temperature consequently positive feedback loop-gain, where it has been demonstrated that the loop-gain exhibits an approximately exponential behavior with the reverse bias voltage. In this subsection, my focus shifts to the hotspot temperature dependency of electrical response. For this purpose, I conducted the HS-LIT experiments on a different DUT with maintaining the same environment (i.e. lock-in frequency of 0.50 Hz, duty cycle of 50 %, framerate of 40 frames per periods, and 30 periods with dropping the first two to reject any initial transients). The laser power is gradually increased to raise the hot-spot temperature. For every investigated laser power, two measurements are performed, one with a 0 bias voltage (only laser power), and one with a DC bias of -2 V. Subsequently the electrical current response is determined as a function of the absorbed laser power and hotspot temperature.

Figure 3.3.8 illustrates the electrical current amplitude as a function of the absorbed laser energy in the Mo layer and the resulting steady-state temperature of the laser-induced hot spot. The measurements started at a low temperature of $T = 38$ °C and gradually increased to $T = 79$ °C. Notably, a pronounced superlinear behavior, resembling an exponential trend, is observed, as indicated by the exponential fit. By applying the exponential diode equation, I estimate the activation energy E_b to be approximately 1.2 eV. It is important to note that the fitted activation energy may be overestimated as the hotspot temperature is likely underestimated due to the uncorrected emissivity of EVA, as previously discussed in Appendix A).

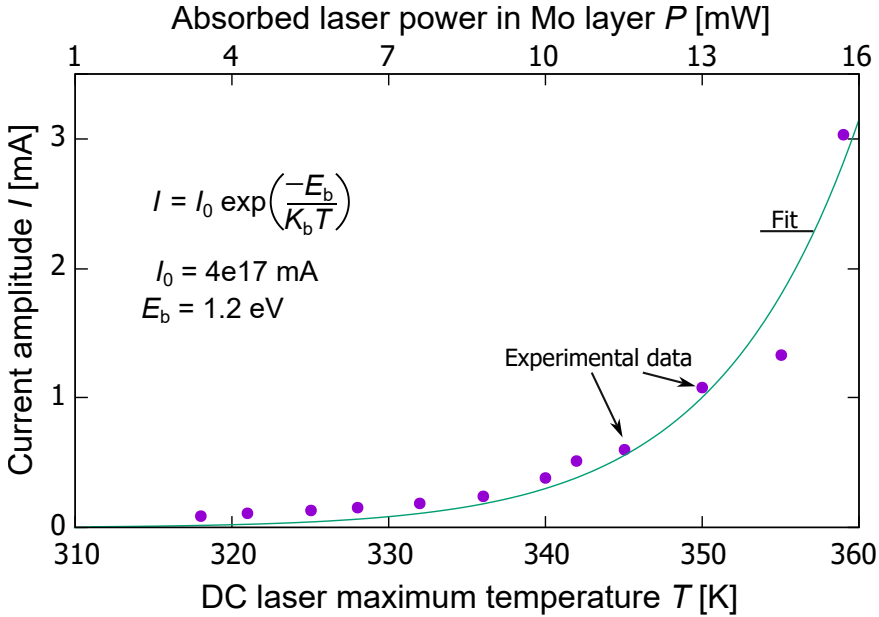


Figure 3.3.8: The electrical power amplitude (A_{Pe}) and the overall loop-gain (G_L) as functions of the local temperature of the laser-induced hotspot. The guide to the eye fitting indicates that the electrical signal exhibits an exponential increase with respect to the absorbed laser power in Mo layer and the resulting local temperature of the laser-induced hotspot. By fitting the temperature-dependent diode equation, an activation energy of 1.2 eV was obtained.

3.4 Summary

This chapter presents a non-destructive thermography-based characterization method that I developed to investigate the positive feedback loop associated with hotspot formation in CIGS thin film solar cells.

The system, which I refer to as Laser-Induced Hot-Spot Lock-In Thermography (HS-LIT) setup, has been optimized to effectively visualize and quantify the loop-gain, demonstrating the interaction between thermal heat and electrical power in a localized hotspot induced by a laser source. The initial HS-LIT configuration clearly proves the interplay between the thermal and electrical properties of the solar cells, where the laser-induced hotspot led to a redistribution of electrical dissipated power, resulting in a hotter region. However, directly measuring the increase in the hotspot temperature was not feasible since the laser was not modulated. To address this, the setup was modified to incorporate laser modulation, allowing to measure the positive feedback loop-gain through the temperature signal increase of the laser-induced hotspot.

Loop-gain quantifies the rate at which thermal runaway develops under specific conditions. I demonstrated that, using lock-in techniques, I can quantify a

loop-gain exceeding 1.0 without causing permanent damage to the sample. This is achieved by measuring the loop-gain at the lock-in frequency under conditions where the system would be unstable under direct current (DC) conditions. I have recorded experimental loop-gain values for industrially produced CIGS cells of up to 2.03 at a reverse bias of 3 V. Additionally, I have found that the loop-gain exhibits a highly superlinear behavior, making the solar cells more susceptible to thermal runaway processes at elevated reverse bias voltages and higher local hotspot temperatures.

The method described in this chapter can be applied to study various scenarios of hotspot mechanisms in CIGS solar cells. The following chapter will detail how the final HS-LIT method can be utilized to observe the impact of the position of the laser-induced hotspot, a factor that can significantly influence the loop-gain. Furthermore, I will investigate and discuss the effect of substrate type and its thickness on the susceptibility of CIGS solar cells to reverse bias stress.

Analyzing Loop-Gain: The impact of Resistive Effects and the Substrate Thermal Conductivity

This chapter aims to expand on the exploration of loop-gain under various conditions using the HS-LIT setup. The previous chapter (Chapter 3) introduced this newly developed HS-LIT setup, detailing its construction and its capability to visualize and quantify the positive feedback effect as loop-gain in thin film solar cells under reverse bias stress. In this chapter, my objective is to investigate how different thermal and electrical properties within the device stack influence the loop-gain. Through a more in-depth examination, I aim to enhance our understanding of hot-spot formation in thin film solar modules resulting from reverse bias stress, utilizing a non-destructive approach.

This chapter is structured into two main sections:

- **Section 4.1** focuses on the impact of electrical resistance effects on the loop-gain. Through a combination of experimental approaches and simulations, this study delves into the loop-gain variation over the solar cell area. I present several experiments on the location dependent loop-gain. Furthermore, a simplified electrical model was specifically designed to predict variations in loop-gain across the cell area. This model does not only align with experimental findings but also extends its utility to hypothetical scenarios not covered by experiments, such as the effect of a local shunt near identified hotspots.
- **Section 4.2** investigates thermal effects of the substrate layer. In this part I make use of flexible solar cells on steel foil. These solar cells have the interesting property that, unlike glass as a substrate, the steel foil is thermally highly conductive. It is expected that such a highly conductive substrate helps transporting the heat away from a hotspot. In this part I thus investigate whether and how such a difference in the substrate material can have an impact on the measured loop-gain.

4.1 The Spatial Distribution of the Loop-Gain: The Impact of Electrode Resistance on the Loop-Gain

Beginning with early research on reverse-bias damage, there has been speculation that the patterning processes could play a significant role in the formation of hotspots, as suggested by Westin *et al.* [5]. This hypothesis is supported by experimental observations, which indicate that scribing lines pose an enhanced risk for reverse bias damage to occur, according to findings by Vaas *et al.* [57]. Various aspects of the patterning processes could potentially increase the likelihood of defect formation. For instance, the P3 scribing could inadvertently damage the semiconductor layers adjacent to the scribed line, while the P1 process might influence the growth quality of the CIGS absorber layer situated above it. In this chapter, however, I explore an independent factor that may contribute to the observed enhanced risk for reverse bias damage at or near the scribing lines. Specifically, the distributed series resistance of the solar cell electrodes is likely to cause an inherent variation of the loop-gain depending on the location within the cell. Thus, independent of possible damage caused by scribing lines, an enhanced likelihood of defect formation may exist at a scribing line. With the newly developed HS lock-in method I have an unprecedented opportunity to examine the extent to which loop-gain is influenced by spatial factors.

This section delves into how defect locations affect loop-gain, particularly focusing on laser-induced hotspots at the edges of the CIGS device, in proximity to the scribing lines, utilizing the refined HS-LIT setup. Assessing loop-gain in these specific areas is vital for a thorough understanding of the dynamics contributing to shunt formation and, by extension, the overall performance of thin-film solar cell modules.

4.1.1 Location-Dependent Measured Loop-Gain

The experimental framework for this investigation aligns with the methodology detailed in Section 3.3, employing identical sample types and following the established HS-LIT procedure. However, rather than having a fixed central position for the laser spot, the location is now varied within the sample to study the effects of the position of a hotspot.

Each edge of the sample corresponds to distinct scribing lines, with one side featuring the P1 scribing line, and the other side the P3 line. To ensure a comprehensive examination, the study compares findings from these edge-specific scenarios against those obtained when the laser spot is centralized. In each instance, the laser is targeted at the specified site, and the HS-LIT procedure is conducted across varying reverse voltage conditions, as previously outlined in Section 3.3.

After conducting LIT measurements, amplitude images akin to those detailed in Section 3.2.3 are generated and then integrated to determine the over-

all loop-gain using Eq.???. Figure 4.1.1 shows the overall loop-gain for all three scenarios plotted against voltage for two different samples. As depicted in Fig. 4.1.1(a), when the laser spot is located at the center of the cell, the loop-gain (represented by purple colored pointed-line) exhibits a significant increase, in a consistent manner with the results previously reported in Section 3.3. Shifting the laser spot towards the left edge (near P1 scribing line) significantly enhances the loop-gain, leading to larger loop-gains at relatively lower voltages. Conversely, when the spot is near the opposite edge of the cell (close to P3 scribing line), the loop-gain experiences a substantial decrease, where it maintains a value closer to 1.0, even at relatively high voltages.

These results are consistent of an enhanced risk for damage near the P1 line, however, not for an enhanced risk near the P3 line (as is observed in [57]). Drawing from previous research, studies by Westin *et al.* [5] and Lee *et al.* [16] have identified a correlation between wormlike defects and scribing lines in CIGS solar cells, where these defects often propagate towards and along the P1 analogue [5, 16]. Similarly, Bakker’s work showed that certain wormlike defects originate at mechanically defined edges, comparable to the P3 scribe line, and subsequently wander towards P1 line [79]. These observations collectively indicate that defects tend to move towards regions of highest loop-gain within the cell (specifically P1 line).

Electronically, the influence of a hotspot’s location on loop-gain can be elucidated in terms of current flow restraint by the most resistive electrode, namely the TCO. The TCO acts as a bottleneck for the current flowing towards the hot-spot. Therefore, when a hotspot is situated at a considerable distance from the P1 scribe line (the point at which the TCO is connected), its series resistance due to TCO resistivity hampers the current flow significantly. Conversely, a hotspot in proximity to the P1 scribe line encounters notably less series resistance. This leads to an increased loop-gain due to the reduced impedence in the electrical pathway.

It is important to highlight that our experimental results, as illustrated in Fig. 4.1.1(a), consistently demonstrate a loop-gain reduction pattern from the cell’s left side (P1 scribe line) to its right side (P3 scribe line), with very low loop-gain values (close to 1.0 even at relatively higher voltages) observed at the right side. In the other experiment depicted in Fig. 4.1.1(b), a similar trend was observed. However, the decrease along the width of the cell was less pronounced. While the loop-gain on the cell’s left side remains higher, reaching a maximum of 1.5 at an early voltage of 1.5 V, the loop-gain on the cell’s right side exhibits values larger than 1.0, reaching a maximum of 1.4 at a later voltage of 2.2 V. I hypothesize that this variation in loop-gain behavior is attribute to an occasional shunt at the P3 line in the first case (Fig. 4.1.1(a)).

To validate my hypothesis and gain deeper insights into this phenomenon, I executed a semi-analytical simulation in the subsequent subsection. This model determine the loop-gain within the cell while it specifically incorporated a shunt at the center of the right side of a CIGS solar cell.

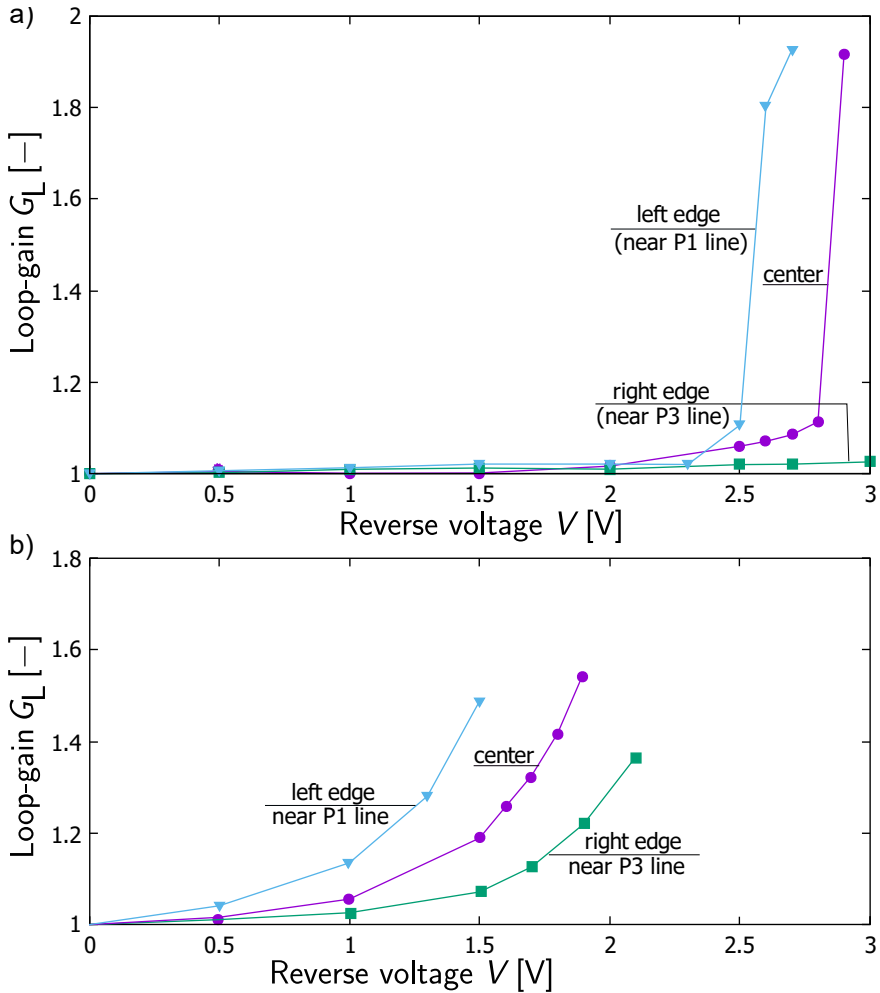


Figure 4.1.1: The overall loop-gain (G_L) as a function of reverse bias voltage (V), while varying the laser-spot location. For each location, I modulate the laser and vary the voltage in reverse while using the same LIT procedure as in Section 3.3. a) A significant increase in loop-gain is observed when the laser spot is positioned at the cell's center and left edge (P1 scribe line), with the loop-gain at the P1 line appearing earlier. In contrast, the loop-gain remains minimal (approximately 1.0) at the opposite edge of the cell (P3 scribe line). b) A loop-gain greater than 1 is evident across all cell locations, including both edges. The overall trend persists, with the P1 scribe line consistently exhibiting larger and earlier loop-gain values compared to other areas.

4.1.2 Modeling Loop-Gain. The Impact of Resistive Effects

To attain a deeper understanding of the influence of the hotspot locations on loop-gain, this study employs a 2D electrical model founded on a semi-analytical approach, as developed by Pieters and Rau [80]. This semi-analytical method applies several simplifications and assumptions:

- The solar cell's current-voltage (I/V) characteristics are linearized around its operating point for simplicity. Although this approximation may detract from the model's precision, the resultant deviation in accuracy is minimal for practical solar cells, where voltage variation within the cell is typically restricted (since substantial voltage variation would indicate considerable series resistance losses) [80].
- The model simplifies the solar cell's structure by considering only one resistive electrode, treating the back contact as an ideal conductor. This assumption is valid as long as the resistivity of one electrode is much higher than the other, like typically the case in a thin-film module with one metal electrode which is much more conductive than the TCO electrode.
- It assumes a strictly rectangular cell configuration, with the resistive electrode connected at one edge. All other edges are deemed to be perfectly isolated.
- Although the solar cell is initially considered homogeneous within the model, it accommodates the introduction of small (circular) regions exhibiting different electrical properties. These regions, acting as point sources, enable the modeling of irregularities such as hot-spots and shunts. Such regions may also have non-linear I/V characteristics.

For an in-depth discussion regarding the model's underlying assumptions and its implementation, I direct readers to reference [80].

This semi-analytical model has the advantage of being relatively fast and accurately modeling the electrical effects I associate with the spatial variation of the loop-gain. However, it lacks a thermal component. Despite this, a first-order approximation of the loop-gain is derived by initially assuming a specific temperature coefficient, α , for the current through the cell under reverse bias. This coefficient increases cell conductivity, described by:

$$I(V, T) = I_0(V)[1 + \alpha(T - T_0)], \quad (4.1)$$

where $I_0(V)$ represents the I/V characteristics at a base temperature (T_0). Utilizing Eq. 4.1, the semi-analytical model can calculate electrical dissipation for specified hotspot temperatures and locations.

My HS lock-in experiments yield a steady-state hotspot temperature, indicating the absence of thermal runaway. Nonetheless, the dissipated laser and electrical power do contribute to hotspot heating. A steady state temperature is achieved when the heating and cooling rates are equal. Consequently, the cooling power is expressed as:

$$P_c = P_L + P_E, \quad (4.2)$$

where P_c denotes the cooling rate, P_L the absorbed laser power, and P_E the electrical dissipation power. The cooling rate is further assumed to be directly proportional to the hotspot temperature:

$$P_c = \beta T_{\text{HS}}, \quad (4.3)$$

leading to a deduced steady-state hotspot temperature given by:

$$T_{\text{HS}} = \frac{P_L + P_E}{\beta}, \quad (4.4)$$

If steady state conditions are reached, the loop-gain is computed from the power ratio:

$$G_L = \frac{P_L + P_E}{P_L}, \quad (4.5)$$

Determining the steady-state operating point iteratively begins by setting $P_E = 0$, then substituting Eq. 4.4 in Eq. 4.1. Continual computation and substitution of new P_E values are performed until the temperature stabilizes. Although more efficient methods may exist to find the steady-state temperature, this fixed-point iteration method offers simplicity in application. By defining T_0 as 0, the iteration process is simplified, transforming Eq. 4.1 to:

$$I(V, T) = I_0(V)[1 + \alpha'(P_L + P_E)], \quad (4.6)$$

where $\alpha' = \alpha/\beta$ is an effective coefficient with the unit W^{-1} , which directly translates the locally dissipated power to the local conductivity.

In this section, the model is applied to illustrate the influence of spatial variations in the loop-gain across the solar cell and the impact of a localized shunt. The parameters for the simulations, detailed in Table 4.1, are selected to approximate the conditions of the experiments shown in Fig.4.1.1(a). It's important to note that the inclusion of a local shunt in the model is hypothetical, aimed at demonstrating its potential effects on the results, as mentioned earlier. This shunt is specifically positioned at the middle of P3 line.

Table 4.1: Simulation parameters for the spatial variation of the loop gain.

Description	Symbol	Value
Solar cell resistivity at T_0	r_C	107 Ωcm^2
Effective conductivity coefficient	α'	23215 W^{-1}
Absorbed Laser Power	P_L	15.4 mW
Applied Voltage	V	-2.7 V
TCO sheet resistance	R_t	24 Ω
Cell length	l	4 cm
Cell width	w	0.4 cm
Shunt x coordinate	x_{sh}	0.364 cm
Shunt y coordinate	y_{sh}	2.0 cm
Shunt radius	r_{sh}	0.03 cm
Shunt resistance	R_{sh}	10^{-12} Ω

Figure 4.1.2 showcases a loop-gain map generated from the 2D semi-analytical model, simulating various hotspot locations across the cell's surface within a grid pattern. The depicted area corresponds to the cell stripe, where notable variation in loop-gain is observed. The highest loop-gain values align with the P1 scribing line. Towards the P3 line within defect-free regions, a modest decline in loop-gain is noticeable, attributed to the limitations imposed by the TCO sheet resistance on current flow through the hotspot. Near the shunt, a significant drop in loop-gain is evident, bottoming out at a minimum value of $G_L = 1$ directly at the shunt site. This phenomenon results from a diversion of current between the hotspot and the shunt, leading to diminished loop-gain. A minor decrease in loop-gain is also perceptible at both the top and bottom edges of the cell. This is a consequence of enhanced current crowding at the edges, where the current pathways are more restricted due to the geometry. With fewer direct current pathways leading to the hotspot, and less surrounding area available to contribute to heat dissipation, the power deposition in these regions is less effective.

This loop-gain distribution in Fig. 4.1.2 closely aligns with experimental observations at a reverse voltage of 2.7 V, the maximum applied voltage shown in Fig. 4.1.1(a). On the left side of the cell, at the P1 line, the maximum loop-gain in simulations reaches approximately 1.96, compared to 1.8 in experimental measurements, as shown in Fig. 4.1.1(a). On the right edge, specifically at the P3 line where the shunt is located, both simulations and experiments yield a loop-gain of 1.02, confirming that the presence of the shunt significantly reduces loop-gain in this region.

Beyond the shunt, loop-gain remains above 1.0 across the right side of the cell stripe. Closer to the shunt, the simulated values reach approximately 1.6, which is consistent with experimental trends. Further from the shunt, loop-gain increases to about 1.8, in agreement with the experimental results in Fig. 4.1.1(b), where all measured locations maintain a loop-gain above 1.0. Although experimental data at 2.7 V is unavailable in Fig. 4.1.1(b), lower-voltage trends confirm that the loop-gain remains above 1.0 at the right edge, supporting the model's predictions in shunt-free areas.

The shunt at the P3 line also influences the middle of the cell stripe, where simulations predict a loop-gain drop to values between 1.2 and 1.4, depending on the proximity to the shunt. Experimental measurements confirm this trend, showing a decrease to 1.1, as seen in Fig. 4.1.1(a).

While the model includes some simplifications, the strong agreement between simulations and experiments reinforces the conclusion that shunts play a critical role in shaping loop-gain behavior.

Interestingly, if I make the hotspot larger (with a radius of 0.3 mm instead of 0.1 mm), an unexpected surge in the loop-gain appears as depicted in Fig. 4.1.3, where the overall loop-gain increased everywhere in the cell peaking at 120 along the left edge, while decreasing along the width of the cell. Near the shunt defect the loop-gain diminishes, reaching a minimum of 1.0 at its center, similar to Fig. 4.1.2. From an electrical perspective, this outcome is understandable as the resistive limitation on current flow is diminished. However, it contradicts

the expectations in a real-world scenario. It is important to note that this simulation doesn't incorporate the thermal dynamics, which play a vital role in actual hot-spots behavior. In reality, the cooling rate of a hotspot is heavily influenced by its size.

The cooling process is governed by the surface area of the hotspot, while the current crowding limitation is determined by its circumference. As the hotspot size increases, its surface area expands more rapidly than its circumference, resulting in more efficient cooling. Consequently, the thermal aspect becomes more critical when studying the behavior of hotspots. This observation highlights the importance of considering thermal aspects alongside electrical ones to achieve a more accurate description of hotspots behavior in solar cells. This electro-thermal coupling is discussed in Chapters 5 and 6, while the impact of hotspot size on loop-gain is discussed in the subsequent section.

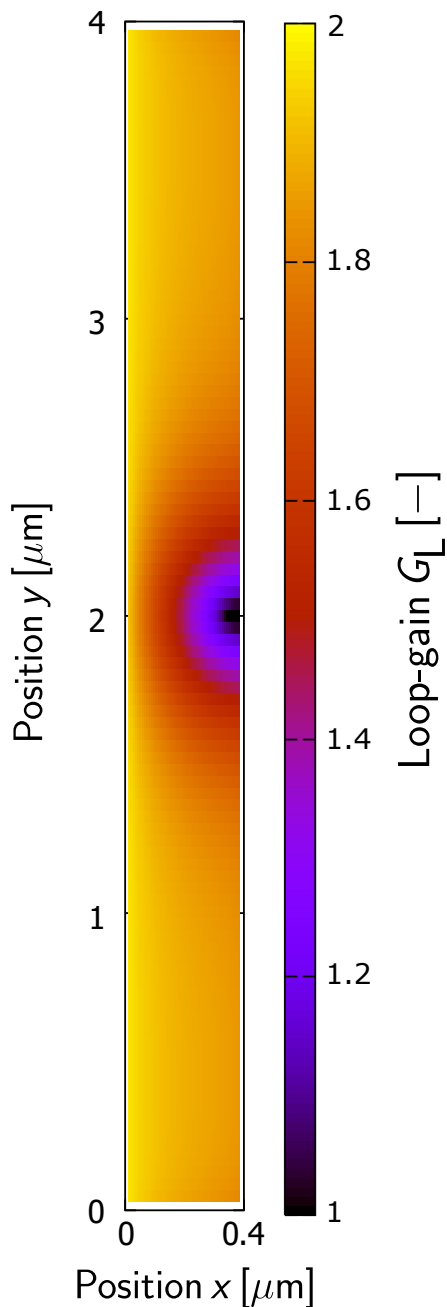


Figure 4.1.2: Loop-gain (G_L) map for a CIGS solar cell, with dimensions of $0.40 \text{ cm} \times 4 \text{ cm}$. The map illustrates a peak loop-gain at the P1 line (left edge), tapering off slightly towards width. Near the shunt defect the loop-gain diminishes, reaching a minimum of 1.0 at its center.

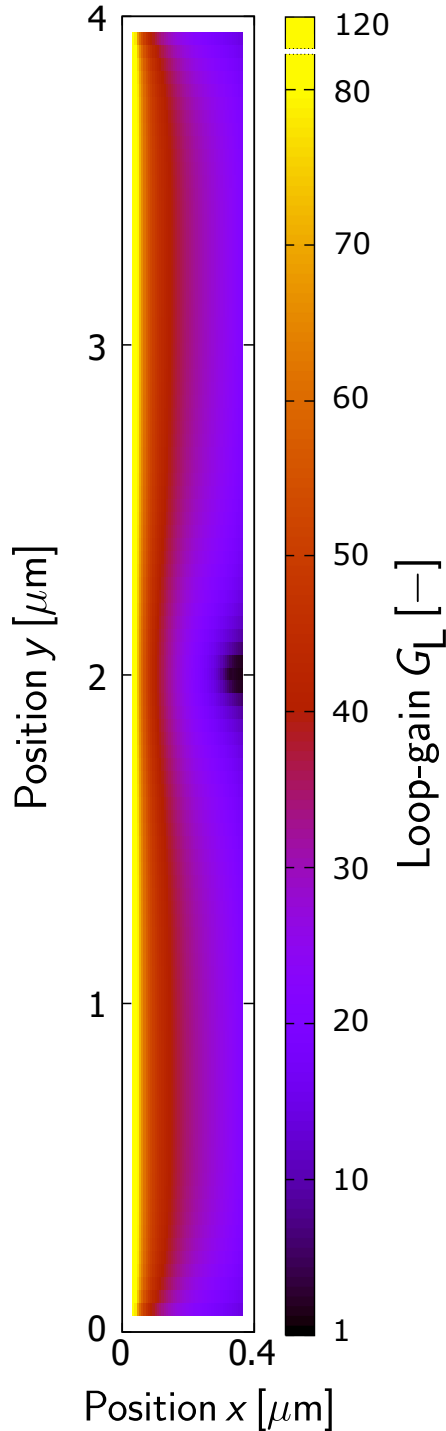


Figure 4.1.3: Loop-gain (G_L) map for a CIGS solar cell, with dimensions of 0.40 cm by 4 cm. The map illustrates a peak loop-gain at the P1 line (the left side of the cell), tapering off slightly towards width. Near the shunt defect the loop-gain diminishes, reaching a minimum of 1.0 at its center. A larger hotspot led to higher loop-gain reaching a peak of 120.

4.2 Flexible CIGS solar cells: the Impact of a Steel Substrate on the Loop-Gain

Beyond the electrical influences on loop-gain covered earlier, this second part delves into how the thermal attributes of the solar cell layer stack affect loop-gain. I introduce industrial CIGS samples, distinct from those previously analyzed, featuring flexibility and deposition on thermally conductive steel foil—a stark contrast to glass substrate samples. This significant change is anticipated to influence loop-gain. I first detail these new samples before presenting and discussing results from HS-LIT experiments.

4.2.1 Flexible CIGS solar cells

Thin-film solar cells offer significant advantages over traditional crystalline silicon cells, including flexibility, which facilitates integration due to their lightweight nature and adaptability to various shapes. Moreover, their non-brittle structure enhances robustness, reducing breakage risks. Consequently, flexible solar cells are particularly relevant for building and vehicle-integrated photovoltaics (BIPV and VIPV, respectively) [3, 28, 81, 82].

Several potential substrates are used in flexible CIGS solar cells technologies. Stainless steel foils, for instance, have advantages regarding their robustness and heat resistance, with recent innovations like SiO_2 diffusion barriers improving their efficiency by blocking impurity migration into the CIGS layer [3, 4, 83, 84]. Alternative metal foils such as titanium, aluminum, and molybdenum are also utilized for their specific attributes: titanium for its strength and resistance to corrosion, aluminum for its light weight and thermal conductivity, and molybdenum for its electrical characteristics [3, 85–87]. Moreover, polymer substrates, notably polyimide and PET, are widely used due to their exceptional flexibility and lightweight nature, although they face constraints in terms of temperature tolerance during manufacturing, necessitating low-temperature deposition methods [3, 82, 88].

In this work I use industrially flexible produced CIGS cells deposited on steel foil. With the help of TNO (Netherlands Organization for Applied Scientific Research) I prepared these samples for the HS-LIT experiments, which will be detailed in the next section. The investigation explores the effects of replacing the traditional glass substrate with a more conductive and thinner steel foil on the loop-gain. Notably, the higher conductivity of steel leads to an increase in the size of the laser-induced hotspot. This larger hotspot size is expected to mitigate the loop-gain in the solar cell, thereby limiting potential damage.

Flexible Sample Preparation

Figure 4.2.1 shows the front and back side of the end encapsulated flexible CIGS cells on steel foil that I received from TNO. The cell features a $12 \times 8 \text{ cm}^2$ substrate, with an active area of $10 \times 4.4 \text{ cm}^2$. These commercially available cells are routinely encapsulated and connected in series to create flexible solar

modules. For these experiments, I needed a single contacted cell, which I can irradiate with a laser from the back side. The normal encapsulation procedure would have polymer encapsulation material on the back of the cell, prohibiting a HS-LIT experiment, as the polymers would not be able to withstand the heat from the laser. To prevent that, the back-side encapsulation material was perforated such that the back encapsulation has a hole through which the steel substrate of the CIGS solar cell is exposed. This way I obtain a sample I may irradiate from the back, directly on the steel substrate.

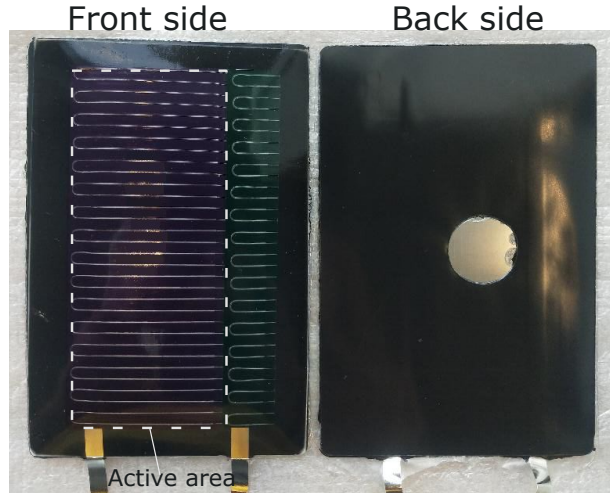


Figure 4.2.1: CIGS cell fabricated on thin stainless steel substrate. The purple area is the active area of the cell. The substrate is $12 \times 8 \text{ cm}^2$, while the active area (i.e. without interconnect) is $10 \times 4.4 \text{ cm}^2$. The backside is encapsulated with PVC polymer. The hole in the polymer is to enable laser application to the backside of the sample in the steel foil directly without risking of melting the polymer and any potential damage to the laser source or its optical components.

HS-LIT on Flexible CIGS Cells

I used the HS-LIT setup as detailed in Section 3.3, with some modifications to accommodate larger samples. Unlike previous experiments, I removed the close-up lens, which has a pixel size of $35 \mu\text{m}$, in favor of the standard lens, with a pixel size of $70 \mu\text{m}$. This change allowed to expand the overall imaged area. By using only the standard lens, I was able to capture the entire active area of the sample within the thermal images frame.

Despite the removal of the close-up lens from the thermal camera, the laser-induced hotspot is much larger in size than earlier while its temperature is lower. I started with parameters and procedure akin to those outlined in Chapter 3 for CIGS on glass, encompassing a lock-in frequency of 0.50 Hz , a camera frequency of 20 Hz , a duty cycle of 50% , and 30 periods with 40 frames per period. However, unlike the previous experiments I did not observe a loop-gain larger

than 1 with these settings. Also electrically, I did not observe any modulation in current due to the modulated hot-spot. Next, the laser power was adjusted to reach a temperature of 80°C (used as the baseline temperature) at the laser spot. It's worth noting that this temperature represents the surface steady-state temperature detected by the thermal camera when only the laser is applied and modulated. Despite this adjustment, the results remained consistent with the initial observations.

Combined with the larger appearance of the laser hotspot, it is apparent that the steel foil mitigates the loop-gain. The larger appearance of the hotspot is due to the higher thermal conductivity. At the same time this large hotspot is less capable to concentrate the power dissipation in a small area, and, thus, the loop-gain is reduced.

As the standard HS-LIT parameters used in other experiments did not allow to measure any noticeable loop-gain larger than 1, I explore various HS-LIT settings in order to quantify a loop-gain for these samples.

In a first attempt I increased the applied reverse voltage, up to -7V . This did not lead to any notable loop-gain, nor did I observe a significant modulation of the current. However, after applying -7V the cell was permanently changed. Figure 4.2.2 depicts EL images at open circuit voltage for a sample, both before and after the LIT measurements. As shown, the sample had a homogeneous EL intensity across the entire cell before the LIT measurement. However, following the measurements, the sample exhibits several dark areas. Thus it appears that although the laser-induced hotspot does not show any enhanced loop-gain, the sample is not immune to reverse bias damage. Furthermore, a small bright spot is noticed there where the laser was applied during HS-LIT measurements.

There are various settings, other than the reverse bias voltage, which may enhance the loop-gain, thereby allowing a non-destructive characterization of the loop-gain. I experimented with a range of parameters such as the duty cycle, which was changed from 50 % to 25 %. The lock-in frequency was also varied. Finally, I increased the laser power, thereby increasing the CIGS temperature.

Figure 4.2.3 shows the electrical response when using a lock-in frequency of 5 Hz, represented as current, as a function of time during LIT measurements while raising the spot temperature and applying a reverse voltage of -2V , simultaneously. Raising the temperature to 115°C proved sufficient to observe a minimal modulation. Further increasing the temperature to 140°C resulted in a more pronounced modulation, making it possible to proceed with the measurements. It should be noted here that only surface temperatures is reported, the actual cell temperatures are expected to be higher and are unknown.

After a lock-in measurement, steady state and lock-in amplitude images have been taken from IRBIS Active Online, similar to Section 3.3.3. In figure 4.2.4, subfigure 4.2.4(a) shows the steady state thermographic image from the thermal camera. For the steady state image the absolute temperature color scale is used. Meanwhile, subfigures (4.2.4(b),4.2.4(c)) present the lock-in amplitude images, which use the shown differential temperature amplitude gray scale.

In the first experiment, only the modulated laser is applied to the sample. The steady state image in subfigure 4.2.4(a) shows the laser-induced hotspot in

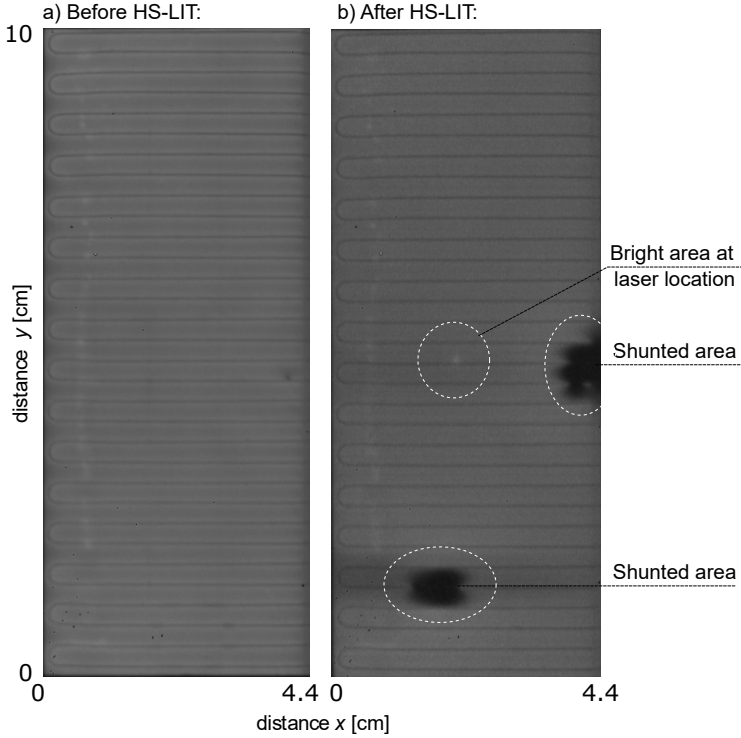


Figure 4.2.2: Electroluminescence (EL) images of a sample a) before and b) after conducting LIT measurements on it. Before the measurements, the sample had a homogeneous power distribution everywhere in the cell. Following the LIT measurements, the sample is shunted while a bright spot appears at the location where the laser was applied.

the device. In this subfigure, the full cell with 10 cm length is apparent in the image. It is also clear that the spot is wider, with a maximum of 140°C . The corresponding lock-in image in subfigure 4.2.4(b) shows a clear signal in the location of the hotspot since the laser is modulated. The spot has a maximum lock-in amplitude of 20 K.

I have repeated the same experiment on the same sample but with an additional DC reversed voltage of 4 V. As observed in subfigure 4.2.4(c), the corresponding lock-in image shows a higher thermal response. The spot now has a maximum lock-in amplitude of 40 K. Furthermore, the size of the hotspot is notably larger, due to the interaction between the modulated laser-induced hotspot and the applied biased voltage.

To gain a deeper understanding of the impact of rising the spot temperature and its influence on the loop-gain, I conducted the full HS-LIT experiments on the same cell, employing two distinct laser-induced hotspot temperatures: 115°C and 140°C . In each case, the laser was modulated at a frequency of 5 Hz while varying the DC reverse voltage, holding all other experimental parameters

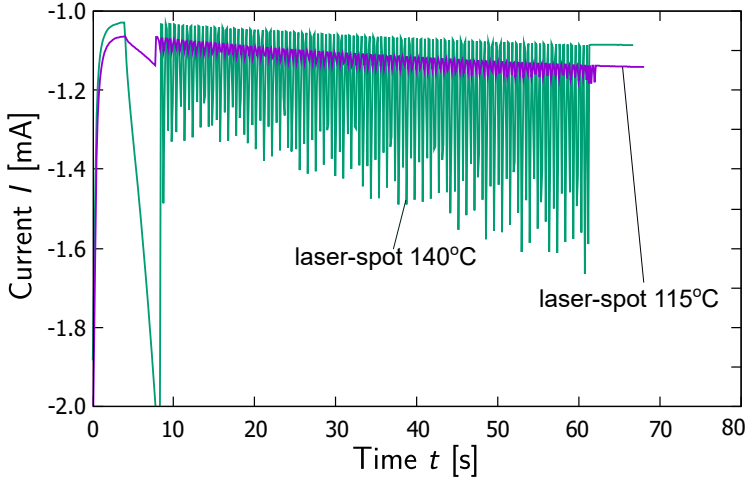


Figure 4.2.3: The electrical response, in terms of current, to the applied DC voltage of -2 V is depicted as a function of time. The current exhibits modulation in response to the modulated laser at a lock-in frequency of 5 Hz , indicating an interaction between the laser-induced hot-spot and the applied voltage. Notably, both LIT measurements are conducted on the same sample, affirming that a higher spot temperature correlates with increased interaction with the current and higher modulation.

constant. From the resulting amplitude images, similar to images depicted in subfig. 3.3.5(b) and (c), the overall loop-gain can be determined using Eq.??.

The resulting overall loop-gain is determined and presented in Figure 4.2.5. As depicted, with the lower temperature case ($115\text{ }^\circ\text{C}$), the loop-gain is weaker with the maximum of 1.07 at a voltage of -4 V . While with the higher temperature case ($140\text{ }^\circ\text{C}$), the loop-gain increases to a maximum of 1.8 at the same voltage.

After the HS-LIT experiments it is important to characterize the sample with I/V sweeps and EL imaging to monitor whether the sample was damaged by the HS-LIT experiments. The results of the I/V sweep before and after conducting the experiments on the sample are depicted in Fig. 4.2.6. The first observation when comparing the differences in IV sweeps before and after the LIT measurement suggests a formation of a moderate shunt during the experiment. The shunt is relatively small, compared to the overall cell area, to not expect a significant performance degradation.

To have a better idea of the changes that happened to the sample, figure 4.2.7 showcases EL images captured at open circuit voltage for the tested sample, both before and after the LIT measurements. Initially, the sample has a homogeneous EL intensity across the entire cell area. However, after the HS-LIT experiments, a dark spot is present situated where the laser-induced hotspot was. Note, however, a thermal runaway was not observed and the resulting shunt is only minor.

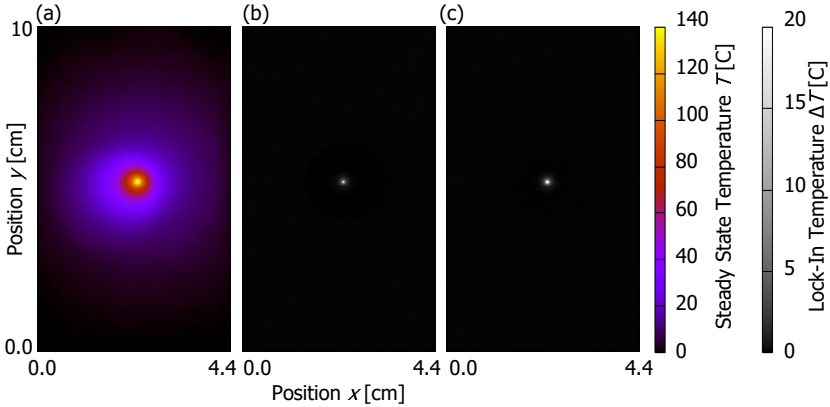


Figure 4.2.4: Results of lock-in measurements using the HS-LIT setup for CIGS on steel. a) steady state thermographic image b) lock-in image of a sample when only the modulated laser is applied c) lock-in image of the sample when the modulated laser with a DC reversed voltage are applied simultaneously. Higher signal appear when applying both the modulated laser and the DC voltage due to their interaction at the laser spot.

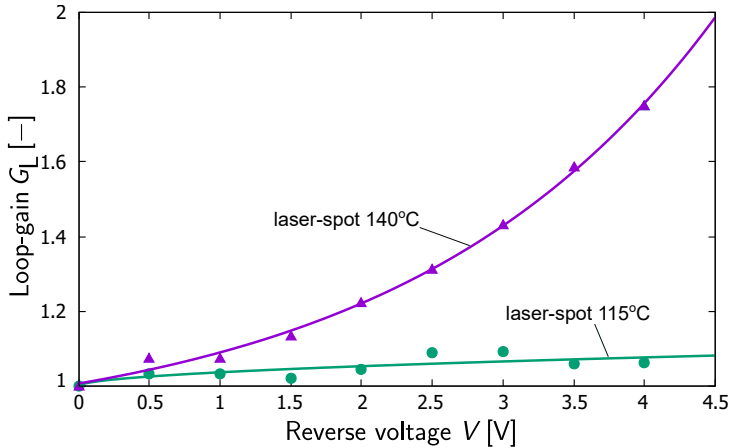


Figure 4.2.5: The overall loop-gain as a function of reverse bias voltage for two different LIT measurements. A maximum loop-gain of 1.8 was achieved with a lock-in frequency of 5 Hz and laser temperature of 140 °C.

Due to the limited availability of samples, and thus the number of experiments I could perform, I could not continue searching for a window of HS-LIT settings to reliably, and non-destructively measure a loop-gain larger than 1 for these samples. However, it is concluded that a positive feedback is observed through HS-LIT. This is achieved by significantly increases the laser hotspot temperature, which in turn damaged the cell. In comparison to the investigated samples on glass, this sample exhibits a significantly reduced loop-gain.

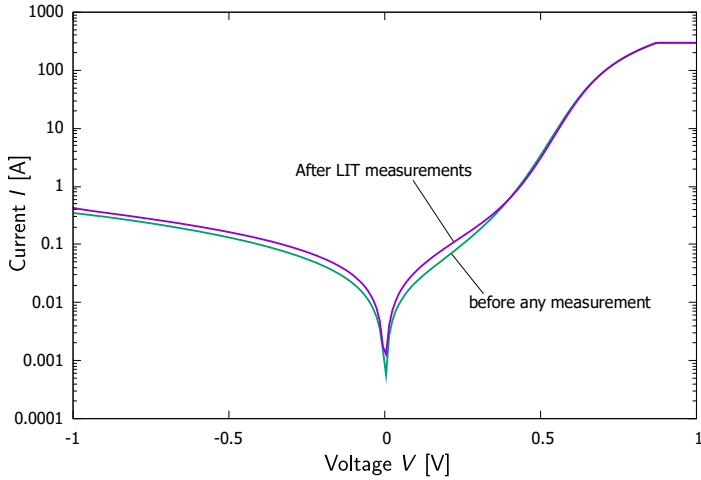


Figure 4.2.6: I/V sweep for the tested sample before and after the LIT measurements. A slight change between the two I/V sweeps indicates that a minor shunt was created, but the sample remains functional.

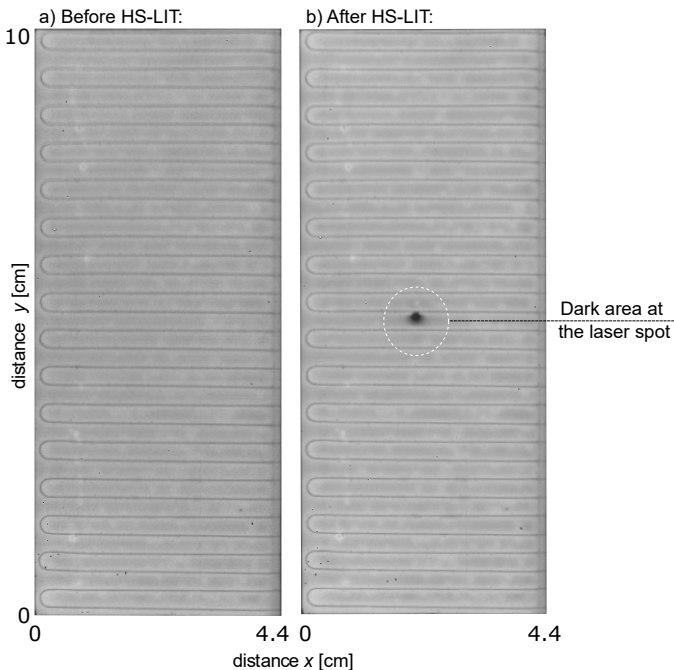


Figure 4.2.7: Electroluminescence (EL) images for the tested CIGS sample on steel a) before and b) after conducting LIT measurements. Before the measurements, the sample has a homogeneous power distribution over the whole cell area. Meanwhile, after conducting the measurements, a dark spot appears at the laser the location suggesting a thermal damage.

4.3 Summary

This chapter continues the experimental investigation to study the formation of hotspots in CIGS solar cells under reverse bias stress. By employing the developed HS-LIT method, outlined in the previous chapter, to further study loop-gain under various conditions, I have found significant location-dependent variations of loop-gain across the solar cell area. Notably, larger loop-gains observed along P1 scribing line indicate an increased risk of damage in these regions. The combination of experimental approaches and simulations, including a simplified electrical model, not only validated these variations but also enabled predictions for defect-presence scenarios. For instance, a local shunt near the P3 scribing line would result in lower loop-gains at that area.

Furthermore, I investigated the thermal effects of substrate layers in the device stack. By using flexible CIGS solar cells on steel foil, I conducted a comparative analysis between glass and steel foil substrates. The results showed that steel foil substrates are less susceptible to reverse bias stress, as the higher thermal conductivity of steel allows for more effective heat dissipation from hotspots. Consequently, hotspots on steel foil became wider and cooler, exhibiting lower loop-gains (i.e. a loop-gain close to 1.0) compared to glass substrates. Further investigation with changing in lock-in thermography parameters like lock-in frequency led to loop-gains larger than one. These findings not only enhance our understanding of hot-spot dynamics in CIGS solar cells but also provide a guidance for future research aimed at optimizing substrate materials and designs.

An Electro-Thermal model for Defect Growth

The work in this chapter focuses on the *destructive* phase of the defect formation due positive feedback effect caused by reverse bias damage in Cu(In,Ga)Se_2 thin film solar cells, specifically the growth of the defect and the time-scale under which it develops. The growth of the defect is an unstable process, where a positive feedback of local current and local temperature also exists. To this end, I developed a Finite Element Method (FEM) model where the electrical and thermal response of CIGS solar cells to reverse bias stress are jointly described. This chapter is dedicated to present the simulation work including the description of the electrical model, the thermal model and their coupling. Additionally, the experimental work that is used for the calibration is briefly discussed. In the end, I study the impact of various device properties on the development of a thermal runaway.

The chapter is structured as follows: Section 5.1 introduces the theory behind the positive feedback loop in CIGS solar cells. Section 5.2 provides an overview of the reverse bias-based experimental work including the main parameters used to build and verify the model. Section 5.3 details the electrical and thermal models and their coupling. Section 5.4 presents key results, including an estimate of the electrical properties of the defective area in CIGS layer and the initial defect size. The full theory of the thermal runaway effect is discussed in Section 5.5, while the summary is given in Section 5.6.

The work presented in this chapter is published in Ref. [89].

5.1 Introduction

Most literature on reverse bias damage uses extended stress conditions (lasting over seconds or more) to investigate reverse bias damage and worm-like defects. However, recent studies focused on shorter time scales of applied reverse stress. Wendlandt and Podlowski [56] have shown that shunt-like defects were formed within a 10 ms light flash while the modules are partially shaded [56]. Furthermore, Vaas *et al.* [57] have shown that with a 10 ms reverse voltage pulse, defects can be created [57]. In the latter experiments, it was shown that a defect with a size of $10\ \mu\text{m}$ was created in less than 1 ms, where there was no sign of a defect before the reverse bias pulse [57]. As the defects reported in the studies by Vaas *et al.* are very small, I do not refer to these defects as worm-like. However, Vaas *et al.* noted that many defects are elongated, which may be an indication that these small defects can propagate to form worm-like defects [57]. Similarly, Johnston *et al.* demonstrated that such small local hot-spots may act as seeds for worm-like defects [51].

One major contribution to theoretically describing these phenomenological findings was published by Karpov [1]. Karpov presented a theory for thermal runaway effects in semiconductor devices, based on the coupling of transverse electron transport and heat transfer in semiconductor thin films. It is shown that the combination of Joule heating with a thermally activated conductivity, leads to a positive feedback and results in instability (thermal runaway) [1]. Experimentally, I have observed such a positive feedback in CIGS solar cells under reverse bias, which I discussed in the previous chapters (Chapter 3 and 4).

Based on Karpov's theory [1], Nardone *et al.* [19] used coupled electro-thermal finite element model (FEM) to demonstrate that, in CIGS solar cells, a small shunt-like defect can lead to such a positive feedback loop, causing thermal runaway [19]. In a related paper, with the same coupled FEM model, it was reported that for a CIGS representative device structure, a pre-existing defect with a radius of $2\ \mu\text{m}$, resulted in a thermal runaway to $T > 1000\ \text{K}$ occurring within a few seconds [58]. However, as discussed before, recent experiments show thermal runaway effects emerging within 1 ms [57]. Thus, there is a discrepancy of 3 orders of magnitude in the modeled and observed rate at which a hotspot develops.

In this chapter, I introduce an electro-thermal FEM model, similar to the model presented in Ref. [19, 58], to investigate the development of thermal runaway effects in CIGS solar cells. I theorize that a small pre-existing defect will develop into a hotspot faster than a large defect, as the volume within which the power is dissipated is reduced, thus, leading to a faster heating. For this reason I use a highly resolved model (both spatially and temporally) and include an initial defect with a 10 nm radius (i.e. a factor 200 smaller than in Ref. [58]). The results are compared with experimental data from the experiments presented in Ref. [57]. In addition, I study the impact of various material properties on the development of a thermal runaway.

5.2 Experiments

The experimental results I use to compare my model to are presented in Ref [57]. These pulsed reverse breakdown experiments were conducted to investigate the time scale of defect creation under reverse bias in CIGS. The used samples consist of two monolithically series connected cells, with a (Glass/Mo/CIGS /CdS/AZO/EVA) layer stack cut from industrial semi-fabricated CIGS modules produced using co-evaporation [75]. The exact thicknesses of all deposited layers can be found in Table 5.1.

The samples are stressed with short (i.e $t = 10$ ms) reverse voltage pulses. Both the electrical and thermal responses are measured using an oscilloscope and thermal camera, respectively. An in depth discussion of the experiments and the results are beyond the scope of this chapter. Here I suffice with some of the key findings.

In this work, I will focus on a single measurement from the experiments in Ref. [57]. The electrical response (both voltage and current as a function of time) for this particular measurement is depicted in Fig. 5.2.1. In this measurement, a 10 ms pulse of -13.40 V (reverse voltage) was applied to the two series-connected cells. Initially, there was no prior-defect visible in thermography for either cell. During the last 1 ms of the pulse, there was a sudden current surge, after which a hotspot became visible in thermography in one of the cells. It's important to note that such a current surge is only, and consistently, observed when a hotspot develops in one cell while the other cell in the series connection remains unaffected and operates normally. In Fig. 5.2.2 the defect was found in the affected cell after the pulse and removal of the encapsulation. The center defect has a radius of about $5 \mu\text{m}$. The observed change in the material indicates the material was locally molten, indicating temperatures around the melting temperature of CIGS (i.e. ranging from 990 to 1070°C [90]). I infer from this experiment that a thermal runaway developed during only the last 1 ms. During this time, the defect developed from something microscopic (invisible in thermography) to a defect of $5 \mu\text{m}$ radius.

5.3 Simulation

In the following, I detail the simulation model for reverse bias hotspots in CIGS solar cells. I start with a short discussion on the seed-defect assumption in Section 5.3.1, which plays a central role in the model. After that, the coupled electro-thermal model will be discussed. I start by introducing the FEM tool `freefem++` in Section 5.3.2, which is used to implement the model. Then, I discuss the thermal model in Section 5.3.3, the electrical model in Section 5.3.4, and the coupling between the electrical and thermal models in Section 5.3.5.

5.3.1 The "seed-defect" assumption

Before diving into the technical details of the simulation model, it is essential to underscore the role of pre-existing defects, i.e. seed defects, in the model for

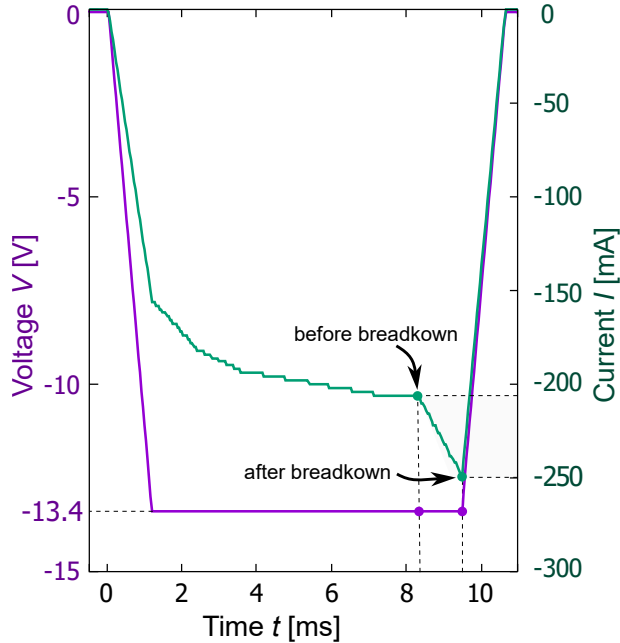


Figure 5.2.1: The electrical response of the sample under investigation, including both the applied voltage (in purple) and the resulting current (in green). The sample, consisting of two-series connected cells, was stressed using a voltage pulse of -13.4 V for 10 ms. A current increase from 210 mA to 250 mA occurred at $t = 8.25\text{ ms}$ after the pulse was applied and lasted for almost 1 ms. This current surge indicates a breakdown in one of the cells (while the other cell in the series connection remains unaffected and operates normally), leading to permanent damage in the affected cell as shown in Fig. 5.2.2 [57].

the formation of worm-like defects in CIGS solar cells. I am not alone in the assumption a pre-existing defect may grow and evolve into a worm-like defect, for example, Johnston *et al.* [51] and Nardone *et al.* [19], both assume a pre-existing defect. The works of Westin *et al.* [5] and Bakker *et al.* [17] indicate that once temperatures reach a threshold that permits thermal decomposition, the CIGS material tends to segregate, forming at least one conductive phase. This formation of a conductive phase can escalate localized power dissipation, creating a positive feedback loop that may not only foster the growth but potentially also the propagation of a defect. It should be noted, however, that there is no proof such a pre-existing defect is always present. In fact, I previously demonstrated a positive feedback in CIGS solar cells under reverse bias with no indications for pre-existing defects are present, using Hot-Spot Lock-In Thermography (HS-LIT), in Chapters 3 and 4. Using HS-LIT, it is possible to observe and quantify a positive loop-gain without causing permanent damage. However, even if no pre-existing defect is present, the observed positive feedback may locally heat the cell to the threshold of thermal decomposition, and lat-

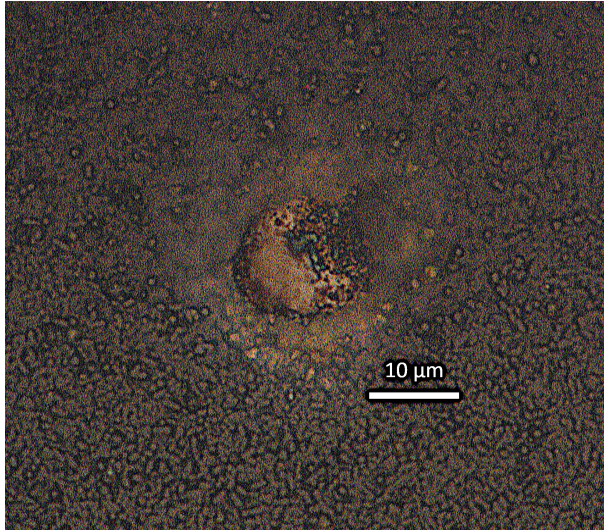


Figure 5.2.2: Microscopic image of a defect with a radius of $5\ \mu\text{m}$ in a CIGS thin film solar cell, after it was subjected to reverse bias stress. The image was acquired using an optical microscope after the removal of the encapsulation [57].

est at this point a shunt-like defect is present, which, from that point onward, may be considered the seed-defect. Another critical point to address is that experiments on reverse bias in CIGS, both in this thesis and in other studies, consistently report the presence of shunt-like defects that form hotspots and may propagate through the device. These defects, visible in the thermographic image as hotspots, clearly indicate significantly higher conductivity compared to the surrounding reverse-biased diode. Consequently, such conductive shunts reduce the local voltage across the diode near the defect, further diminishing the current through the diode in the vicinity of the hotspot. As a result, the temperature of the device remains unchanged far from the defect, while near the defect, the current bypasses the diode. Since the temperature dependency of the diode current, therefore, appears to play a subordinate role in the process, I disregard the thermally activated nature of the diode current in the analysis. This approach also evades the issue of not being able to provide reliable temperature-dependent diode characteristics up to the critical temperatures of $990 - 1070\ \text{°C}$ observed in the experiments.

5.3.2 freefem++

The coupled electro-thermal model is implemented using freefem++ [91]. The freefem++ open-source simulation tool applies the finite element method to solve high-level partial differential equations (PDEs) numerically in 2 dimensional (2D) or 3 dimensional (3D) domains [91, 92]. Furthermore, freefem++ provides its own flexible scripting based on C++ to build meshes and solve

PDE's.

Mesh Generation

An interesting aspect of `freefem++` is the advanced automated mesh generator that can dynamically vary and adapt the mesh as needed, with the ability to generate high-resolved meshes. This feature holds particular significance in the simulations, as I am modeling a very small defect, where precise meshing is crucial for accurate results. To achieve that, `"adaptmesh"` and `"splitmesh"` commands in `freefem++` are used to refine and adapt the mesh in the vicinity of the defect. It is important to note that since the initial defect is very small (a radius of 10 nm), the center of the domain is discretized into FEM triangles with sizes that are even smaller than 10 nm, resulting in a substantial number of FEM elements. As a result, a logarithmic scale is used during the mesh refinement, allowing it to coarsen gradually further away from the area of interest, as depicted in Fig. 5.3.1, to save computation time.

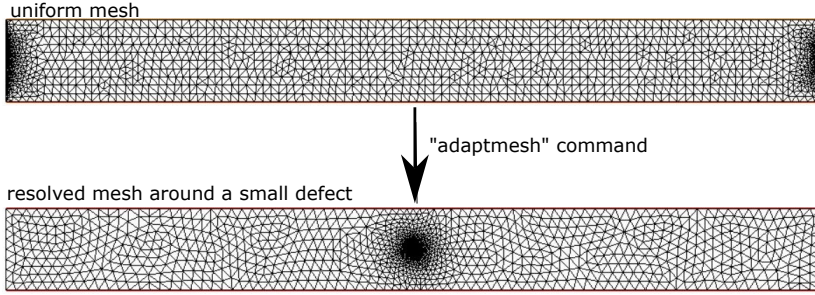


Figure 5.3.1: An illustrative comparison of a generated mesh before and after refining the area in and around a small defect using `"adaptmesh"` command in `freefem++` simulation tool. A logarithmic scale is used to adapt a high resolved area in the center of the domain (area of interest), while the rest of the domain remains coarse to save computation time.

5.3.3 Thermal model

The thermal model entails the complete layer stack consisting of Glass/ Mo/ CIGS/ AZO/ EVA. The initial electrical defect is small both in lateral and vertical dimensions. Thus I require a full 3D model for the thermal system. Furthermore, as I am interested in the dynamics of a thermal runaway process, the thermal model needs to be a transient model. The 3D transient heat equation is formulated as

$$k\nabla^2 T + P(t) = \rho c_p \frac{\partial T}{\partial t}, \quad (5.1)$$

where:

- $k\nabla^2 T$ is the heat conduction within the material, where k is the thermal conductivity and T is temperature.
- $P(t)$ is the locally dissipated electrical power as function of time t .
- $\rho c_p \frac{\partial T}{\partial t}$ is the time dependent change in temperature, where ρ the density of the medium and c_p the specific heat capacity.

I consider solutions of Eq. (5.1) in a 3D cylindrical domain representing the solar cell layer stack, as illustrated in Fig. 5.3.2. The defect is located laterally in the center of the cylindrical domain. Vertically the defect is located in the electrically relevant part, i.e. the CIGS and AZO layers. I use a variable mesh to create a highly resolved mesh around the defect, achieving maximal triangulation of the nodes.

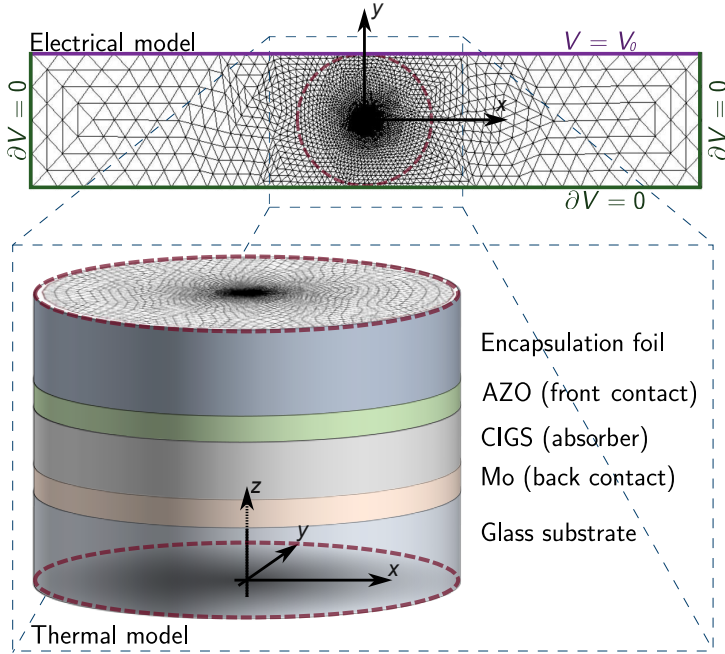


Figure 5.3.2: Schematic illustration of the mesh for both electrical and thermal models. The electrical model is rectangular with dimensions of 0.4 cm X 2 cm, while the thermal model is cylindrical with a diameter equals the width of the cell (i.e. 0.40 cm), and a depth equals the thickness of all layers in the stack as in Table 5.1.

The heat loss at the front and back surface of the stack is taken into account with a Neumann boundary condition according to

$$\frac{\partial T}{\partial \mathbf{n}} = -b(T - T_{\text{amb}}), \quad (5.2)$$

Table 5.1: The used CIGS device properties. The EVA properties are taken from Ref [94]. All remaining properties are from Ref [95]

layer name	thickness d [m]	thermal conductivity k [$\text{Wm}^{-1}\text{K}^{-1}$]	specific heat capacity c_p [$\text{Jkg}^{-1}\text{K}^{-1}$]	density ρ [kgm^{-3}]
EVA	0.30×10^{-3}	0.34	1400	950
AZO	1.05×10^{-6}	23.0	494	5670
CIGS	2.05×10^{-6}	3.7	300	5770
Mo	1.00×10^{-6}	138.0	250.7	10280
Glass	3.00×10^{-3}	1.42	1154	2380

where \mathbf{n} is the exterior normal of the boundary, b is a heat loss term to the ambient air, and T_{amb} is the ambient temperature.

For the vertical cylindrical boundary I apply a Dirichlet boundary condition with $T = T_{\text{amb}}$. However, I choose the diameter of the cylindrical domain such that that $\frac{\partial T}{\partial \mathbf{n}} \approx 0$ for all simulations in this work (i.e. the lateral simulation domain is chosen large enough to represent a semi-infinite xy -plane). For the simulations in this work I found a radius of 0.2 cm to be sufficient to meet this requirement.

I exclude radiative heat transfer, characterized by its T^4 dependence, from the model due to the highly localized nature of high-temperature regions within the layer stack, particularly around shunt-like defects. These localized hotspots are effectively insulated from direct radiative cooling to the ambient environment by the surrounding device layers and encapsulating materials. Moreover, convective cooling, which is included in the model, primarily occurs at the encapsulation surface, at a significant distance from these internal high-temperature zones. Given the relatively short timescales of the simulations, the increase in surface temperature of the device is minimal, further reducing the potential impact of radiative heat transfer.

For the thermal properties of the various materials I used the parameters listed in Table 5.1, which are found in literature as indicated. The convection coefficient b is set to $b = 12 \text{Wm}^{-2}\text{K}^{-1}$ [93]. The ambient temperature is set to $T_{\text{amb}} = 22^\circ\text{C}$.

5.3.4 Electrical model

I expect the electrical response to be much faster than the thermal response. Thus, I consider a steady state solution for the electrical model. The electrically

relevant part of the system consists of several thin-films (Mo/CIGS/AZO). As the Mo electrode is much more conductive than the AZO electrode ($R_b \gg R_f$), I consider the Mo as a perfect conductor while the resistance in the AZO electrode is represented as the sum of both components, $R_{\text{sheet}} = R_f + R_b$. Consequently, I may limit the electrical model to describe the potential in the AZO. As the resulting electrical model consists only of a single thin-film, I can solve this problem in a 2D domain. Within a 2D electrode, the steady-state potential may be described with Poisson's equation [80]

$$\nabla^2 V(x, y) = R_{\text{sheet}} J(x, y), \quad (5.3)$$

where V is the local voltage, R_{sheet} is the electrode sheet resistance (per square), and J is the current density through the solar cell (i.e. out of the electrode).

If I linearize the current density through the solar cell, I can rewrite Eq.5.3 as

$$\nabla^2 V(x, y) = R_{\text{sheet}} \frac{V(x, y)}{R(x, y)}, \quad (5.4)$$

where R is the electrical resistivity of the solar cell. For $R(x, y)$ I assume two phases in the electrical system. A defected phase with $R = R_{\text{def}}$ and a non-defective phase $R = R_{\text{non-def}}$.

As illustrated in Fig. 5.3.2, the CIGS solar cell consists of a rectangular cell stripe. The boundary value problem is defined on a rectangular domain. One edge is assigned a Dirichlet boundary ($V = V_0$) where the voltage is fixed at a constant value V_0 , which is the voltage applied to the cell. The remaining 3 edges are assigned a Neumann boundary ($\partial V = 0$), indicating no change in voltage along those boundaries [80].

In this work I consider a rectangular cell with a width of 0.40 cm, and a length of only 2.0 cm. Note that the lateral dimensions for the electrical model exceed those of the domain I consider for the thermal simulations. However, the electrical dissipation is generally dominated by the defect, and thus the electrical power dissipation is still mostly confined within the domain considered in the thermal simulations. The initial defect radius is varied in this work. However, the smallest initial defect size I consider is 10 nm.

I parameterize the model according to the experiment discussed in Section 5.2 as shown in Table 5.2. The voltage over the two series connected cells is -13.4 V, while the current is around -210 mA before the breakdown and dropped to a higher negative current of -250 mA after the hotspot creation. With a cell area of 8.4×0.40 cm², I can estimate the current density over the cell area before the breakdown as 62.5×10^{-3} mAcm⁻². The non-defected, active part of CIGS would then have an average resistance of $R_{\text{non-def}} = (13.4/2)/(62.5) = 1.07 \times 10^2$ Ωcm².

As the experimental procedure involves a sample with two series-connected cells, the voltage is being divided between them. Before breakdown, it is anticipated that the voltage is evenly distributed, with each cell receiving approximately half of the applied voltage, as previously described. However, only one cell broke down, hence during breakdown, the exact voltage distribution becomes uncertain. Consequently, I opt for a current-driven approach in the

Table 5.2: The electrical properties of CIGS devices used for this work.

Parameter	Value
Voltage over 2 cells (V)	-13.4 V
Current before breakdown (I_{bb})	-210 mA
Current after breakdown (I_{ab})	-250 mA
Current density (J_{bb})	$62.5 \times 10^{-3}\text{ mAcm}^{-2}$
CIGS resistance ($R_{\text{non-def}}$)	$107\ \Omega\text{cm}^2$
Sheet resistance (R_{sheet})	$24\ \Omega$

simulation to ensure that the current matches the breakdown current, as I know that the two adjacent cells will have the same current value. I assume the defected area to be very conductive. The shunt resistance of the defected phase R_{def} is one of the parameters under investigation. I vary the value of R_{def} over a wide range. The minimum value is based on the electrical resistivity of a pure copper crystal (i.e. $1.678 \times 10^{-8}\ \Omega\text{cm}$ at 20°C) [96], and the maximum value is the non-defected resistivity $R_{\text{non-def}}$. For the AZO electrode sheet resistance I rely on data provided by the CIGS module manufacturer, $R_{\text{sheet}} = (R_f + R_b) = 24\ \Omega$.

Validation of the electrical model

To ensure the accurate implementation and reliability of the electrical freefem++ model, I validate the FEM model by comparing it to a semi-analytical model developed by Pieters and Rau [80]. In the context of a 2D rectangular device with no current injection along the x -direction, the problem can be simplified to a one dimensional case. Specifically, I employ a 1D solution based on the shunt-free device model from [80]. It is a semi-analytical approach to solve the 1D system for the potential distribution, which can be described as follows:

$$V = V_0 \frac{\cosh(\lambda(w-x))}{\cosh(\lambda w)}, \quad (5.5)$$

with

$$V_0 = \frac{I_0 R_{el}}{l\lambda \tanh(\lambda w)}, \quad (5.6)$$

and

$$\lambda = \sqrt{\frac{R_{el}}{R_\Upsilon}}, \quad (5.7)$$

where V_0 and I_0 are the applied voltage and injected current across the Dirichlet boundary, respectively. λ is the inverse characteristic length, and R_Υ is resistance of the domain. While l and w are the length and width of the domain, respectively. Further details regarding the equation's derivation can be found in [80].

For the comparison, I consider a single cell of identical dimensions for both `freefem++` simulation and the semi-analytical model. This cell has a length of 4 cm and width of 0.40 cm. A voltage of $V = 6\text{ V}$ is applied along the upper long edge in both models. Additionally, a domain resistance of $107\ \Omega\text{cm}^2$ (i.e non-defective CIGS resistance derived in section 5.3.4) is adopted in both approaches.

Figure 5.3.3 depicts the resulting potential distribution across the width of the cell in for both `freefem++` and semi-analytical methods. The plot clearly shows that the FEM approach produces results that align consistently with the solution from the semi-analytical approach. This alignment confirms the precise implementation of Poisson equation within the developed electrical `freefem++` model.

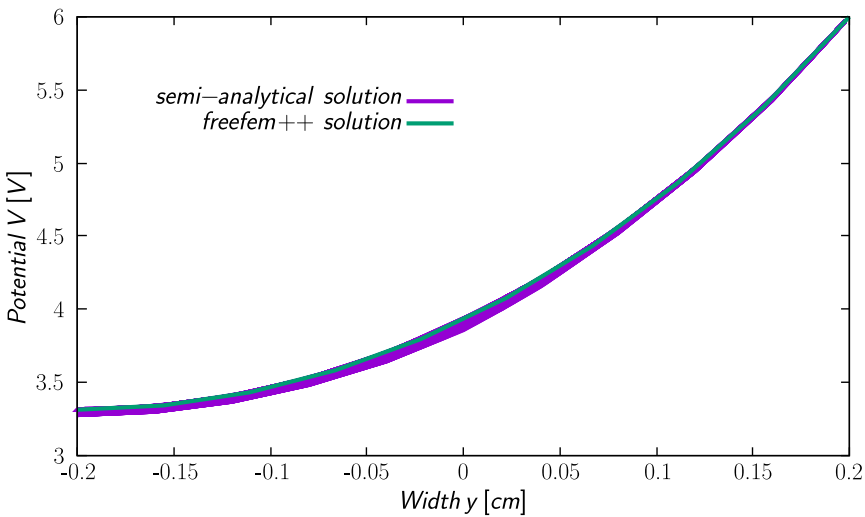


Figure 5.3.3: A comparison in potential distribution between the `freefem++` electrical model and the semi-analytical solution solved as demonstrated by Pieters and Rau [80]. In both approaches, a device with a length of 4 cm and width of 0.40 cm is utilized, with a voltage of $V = 6\text{ V}$ being applied along the upper long edge. Additionally, a domain resistance of $107\ \Omega\text{cm}^2$ (as derived from section 5.3.4) is adopted. The potential distribution resulted from two models, along the width side of the device, align well with each other.

5.3.5 Coupling

To study Joule heating in an electrical system, I need to couple the electrical and thermal models. This coupling is done iteratively, with the output of each model serving as the input for the other. Specifically, I need to extract the electrical power dissipation from the electrical model and map it to the corresponding volumes in the thermal model. To complete the cycle, the temperature distribution from the thermal model influences the electrical properties in the

electrical model, specifically through the defect size. The coupling process is illustrated in Fig. 5.3.4.

From the electrical model in Eq. (5.4), I compute the power density in the AZO electrode as

$$P_{\text{AZO}}(x, y) = \frac{|\nabla V|^2}{R_{\text{sheet}}}, \quad (5.8)$$

where $|\nabla V|$ is the electric field (F) within the electrode. Likewise, the power dissipation in the CIGS solar cell is computed as

$$P_{\text{CIGS}}(x, y) = V^2 G(x, y), \quad (5.9)$$

where $G(x, y)$ is the electrical conductivity.

The power dissipation from Eq. (5.8) is mapped to the AZO layer. Note that the power density from Eq. (5.8) is in Wm^{-2} . By distributing the power uniformly over the AZO layer thickness, I compute a power density in Wm^{-3} to inject in the electrical system. In a similar way I map the electrical power density from Eq. (5.9) to the CIGS layer. However, most of the power dissipation in the solar cell is limited to the depletion width in the solar cell. For simplicity I map the dissipated power density from Eq. (5.9) uniformly to the top third of the total CIGS layer thickness.

As illustrated in Fig. 5.3.4, there is also a coupling back from the thermal model to the electrical model. This coupling is via the defective and non-defective phases in the electrical model. I assume that beyond a critical temperature (T_{crit}) the CIGS undergoes permanent structural changes (i.e., the CIGS becomes porous with copper, indium, and gallium migrating towards the back contact [6]).

The melting point of CIGS is between 990°C and 1070°C [90]. Given this relatively narrow range, I choose $T_{\text{crit}} = 1000^\circ\text{C}$ as the threshold value for the model. Considering the narrow melting point range, I expect any variations due to threshold adjustments to be minimal.

If the temperature within the CIGS exceeds this temperature, I change the phase from non-defected to defected. In other words, the temperature of each triangular element within the finite element mesh of the CIGS layer is evaluated in the thermal model. If it exceeds the 1000°C , the resistance of that corresponding region is switched from non-defected to defected resistance in the electrical mesh. Note, however, that this change is permanent, i.e. the defected phase never changes back to non-defected even if the FEM triangle cools down in the following iterations. This phase change allows the defect to grow.

The solution of the coupled electro-thermal model starts by solving the electrical model in Eq. (5.4) and mapping the dissipated power densities in both AZO and CIGS layers from Eqs. (5.8) and (5.9), respectively, to the thermal system as shown in Fig. 5.3.4. Subsequently, I simulate the transient thermal model until I find the temperature within the CIGS exceeds the critical temperature. If this is the case, the electrical model of Eq. (5.4) is updated and the new power dissipation from Eqs. (5.8) and (5.9) are mapped again to the appropriate volumes in the simulation domain.

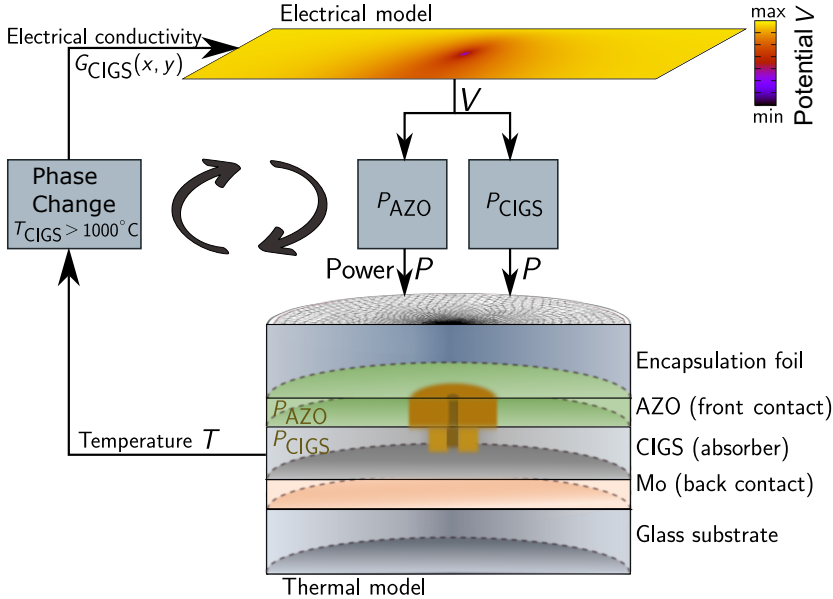


Figure 5.3.4: Schematic illustration of the coupled electro-thermal model. The two models are linked via electrical power from the electrical model and temperature distribution from the thermal model at each time iteration. The electrical power is calculated and mapped in both AZO and CIGS layers. The temperature of each FEM triangle in the middle of CIGS layer is evaluated, if it exceeds the melting temperature of CIGS, the resistance of corresponding area in the electrical mesh is shifted from non-defected to defected value.

For the time discretization I apply a semi-adaptive time step where the time step is linked to the defect area. As in general the maximum dissipated power density decreases with increasing defect radius, the time step can increase for larger defects without much loss of accuracy.

5.3.6 Discussion

As a final note I would like to shortly discuss the difference between current- and voltage-driven experiments. In this work I have opted to simulate a current driven experiment, i.e. the current is kept constant. In current-driven experiments, the creation of defects will reduce the voltage over the device and subsequently quench the power dissipation at hotspots. In contrast, in voltage-driven experiments, the current will increase, potentially accelerating the growth and evolution of hot-spots due to increased power dissipation.

I would like to argue here that voltage-driven experiments do not accurately reflect real-world field conditions for reverse bias damage. In practical scenarios, reverse bias damage is predominantly current-driven. Commercial CIGS modules typically operate with maximum power point voltages ranging from

60–85 V. This relatively high voltage allows the maximum power point current (I_{mpp}) to pass through shaded cells, largely independent of their specific breakdown voltages, which are typically an order of magnitude lower. Consequently, in real-world applications, reverse bias damage occurs under near-constant current conditions, rather than constant voltage.

5.4 Results

Baseline

A baseline for the simulation results is first presented. For this baseline I set the defect resistance to $R_{\text{def}} = 3.14 \times 10^{-7} \Omega\text{cm}^2$ for the initial defect of 10 nm radius. In Fig. 5.4.1 I show the results for the baseline simulation after 0.126 μs . In Fig. 5.4.1(a) the temperature is depicted. In the center of this graph the temperature exceeds the critical temperature of 1000 °C. Accordingly in Fig. 5.4.1(b) the phase map exhibits a circular defect with an approximate radius of 0.90 μm (compared to an initial radius of 10 nm). The corresponding power densities in the AZO and CIGS layers are shown in Fig. 5.4.1(c) and Fig. 5.4.1(d), respectively. From Fig. 5.4.1(c) I observe that the dissipated power density in the AZO increases towards the defect where it peaks at the defect circumference, then drops to 0 Wm^{-3} within the defect. In Fig. 5.4.1(d), the power dissipation is within the whole area of the defect as the power is generated in the CIGS layer itself. Additionally, it is noted that the power in CIGS is much higher than the power in the AZO layer.

Moreover, in Fig. 5.4.2 the results for the baseline after 5 μs is shown. In Fig. 5.4.2(a), the area of temperature exceeding the 1000 °C is expanding. Accordingly in Fig. 5.4.2(b) the phase map exhibits a larger defect with an approximate radius of 2.5 μm . From Fig. 5.4.2(c) I observe that the dissipated power density in the AZO increases towards the defect, and suddenly drops to 0 Wm^{-3} within the defect. This is expected as current crowding at the edge of the defect leads to higher dissipation toward the defect. In Fig. 5.4.2(d), the power dissipation is within the whole area of the defect reaching its maximum at the circumference of the defect.

Figure 5.4.3 shows the results when the defect has reached a radius of 6.2 μm after 0.55 ms. In Fig. 5.4.3(a) the temperature of a larger area exceeds the critical temperature of 1000 °C. Consequently, the phase map in Fig. 5.4.3(b) shows a larger defect. The defect is not exactly circular anymore, but the effective radius is 6.2 μm , where I determined the effective radius from the defect area (i.e. $A_{\text{def}} = \pi r_{\text{eff}}^2$). Figure 5.4.3(c) and 5.4.3(d) depict power densities in the AZO and CIGS layers, respectively. Comparing the results to Figs. 5.4.2(c) and 5.4.2(d), respectively, I observe the electrical power density decreased considerably for the larger defect radius. This is a direct consequence of the increased size as with a larger defect, less current crowding at the edge of the defect is expected. Furthermore, in Fig. 5.4.3(c), higher power density is observed along the contour of the defected area. These areas with a higher power density correspond to the areas with higher power density at the circumference of the

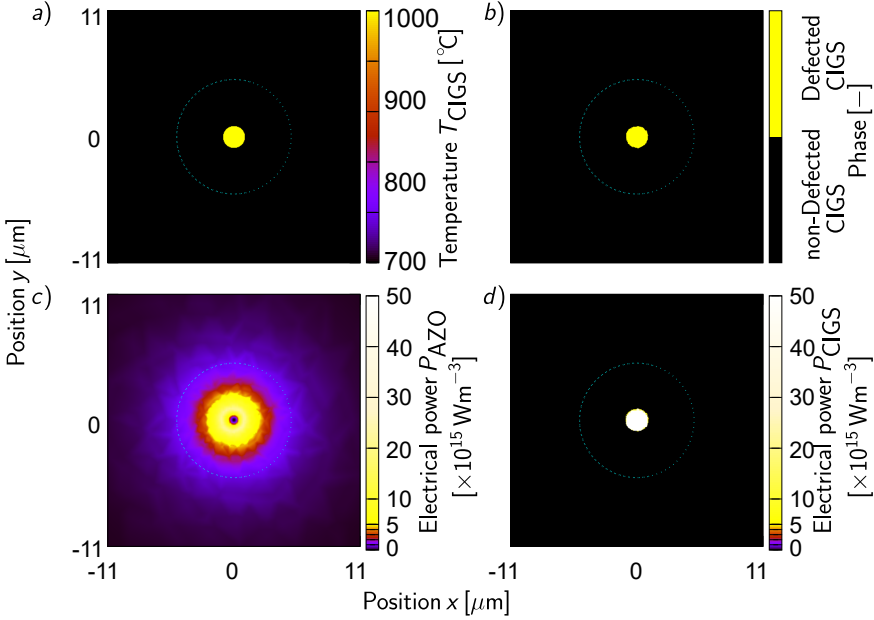


Figure 5.4.1: a) Temperature distribution profile in the middle of CIGS layer, b) phase plot, c) AZO power profile, and d) CIGS power distribution for the baseline simulation (defect resistance is $3.14 \times 10^{-7} \Omega\text{cm}^2$, initial radius of 10 nm), when the defect has reached a radius of around $0.90 \mu\text{m}$ after $0.126 \mu\text{s}$. The current is injected from the top long edge of the cell. Cyan circle indicates a radius of $5 \mu\text{m}$.

defect in Fig. 5.4.3(d). Comparing the locations of areas with higher power density in Figs. 5.4.3(c) and 5.4.3(d) with the phase plot in Fig. 5.4.3(b), I can see that the non-smooth circumference is caused by the ragged contour of the defect. However, this ragged nature of the contour is related to the simulation mesh, i.e. at this point in the simulation the resolution of the mesh is too low to produce a sufficiently smooth contour of the defect.

Time Evolution and Parameter Variation

In Fig. 5.4.4, the effective radius of the defect size is shown as a function of time for three defect resistance values: $3.14 \times 10^{-5} \Omega\text{cm}^2$ (in blue), $3.14 \times 10^{-7} \Omega\text{cm}^2$ (in green, baseline) and $3.14 \times 10^{-9} \Omega\text{cm}^2$ (in purple). As the defect in the simulation is not always perfectly circular, the effective radius is defined as the radius for which a circle has the same area as the defect area in the simulations.

Starting with the baseline simulation in Fig. 5.4.4, which has a defect resistivity of $3.14 \times 10^{-7} \Omega\text{cm}^2$ (in green), the defect initially remains stable with no growth. This is followed by a rapid growth phase where the defect radius increases by more than an order of magnitude. Subsequently, a more steady and gradual growth is observed, with the defect reaching a radius of $6.2 \mu\text{m}$ after

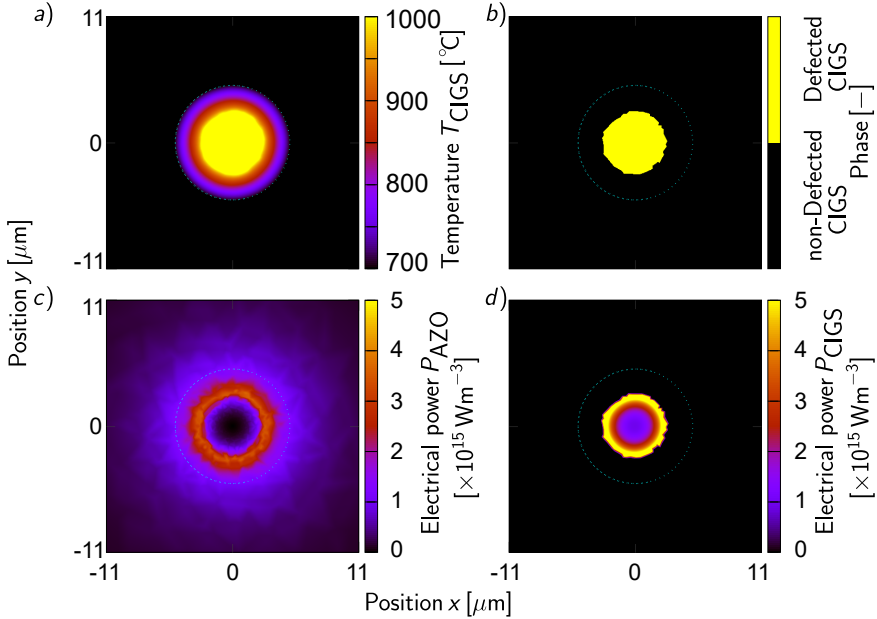


Figure 5.4.2: a) Temperature distribution profile in the middle of CIGS layer, b) phase plot, c) AZO power profile, and d) CIGS power distribution for the baseline simulation (defect resistance is $3.14 \times 10^{-7} \Omega\text{cm}^2$, initial radius of 10 nm), when the defect has reached a radius of around $2.5 \mu\text{m}$ after $5 \mu\text{s}$. The current is injected from the top long edge of the cell. Cyan circle indicates a radius of $5 \mu\text{m}$.

0.55 ms. Following this point, the defect did not grow more up until the end of the simulated time frame of 1 ms. I would like to stress that this does not imply stability; the defect's growth clearly slows down as more time is required to heat a larger volume. However, hotspots and worm-like defects evolve over the time frame of many seconds, which is beyond the scope of this chapter.

In comparison, the defect growth with a lower resistivity (defect resistivity of $3.14 \times 10^{-9} \Omega\text{cm}^2$ (in purple)) exhibits a much faster growth from a very early stage in time followed by a steep increase in the growth where the defect has reached a radius $\gg 15 \mu\text{m}$ in less than the simulation period of 1 ms. On the other hand, a higher defect resistivity of $3.14 \times 10^{-5} \Omega\text{cm}^2$ (in blue) results in no defect growth by the end of the 1 ms.

In the next step, as depicted in in Fig. 5.4.5, I further investigate the impact of the resistivity of the defected area in term of the amount of electrical power dissipated in the defect, using the same defect resistivity values as in Fig. 5.4.4: 3.14×10^{-5} , 3.14×10^{-7} (baseline), and $3.14 \times 10^{-9} \Omega\text{cm}^2$. I only consider the electrical model in order to evaluate the electrical power dissipation. Figure 5.4.5 shows the power dissipation integrated over an area around the defect with a $20 \mu\text{m}$ radius. This specific area was selected in order to compare various cases

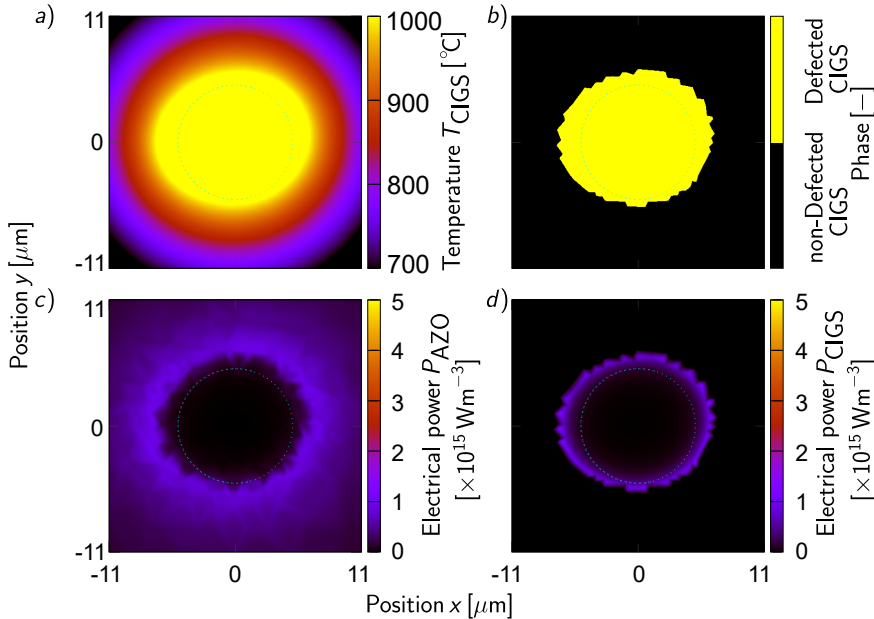


Figure 5.4.3: a) Temperature distribution profile in the middle of CIGS layer, b) phase change plot, c) AZO power profile, and d) CIGS power distribution. for the baseline simulation (defect resistance is $3.14 \times 10^{-7} \Omega\text{cm}^2$, initial radius of 10 nm), when the defect has reached a radius of around $6.2 \mu\text{m}$ after 0.55 ms . The current is injected from the top long edge of the cell. Cyan circle indicates a radius of $5 \mu\text{m}$.

more effectively while varying other parameters including the defect size and its resistivity. Thus this figure describes how much power is deposited at the defect area, i.e. it evaluates the power coupling of the defect to the electrical power source. In Fig. 5.4.5 I distinguish between the integrated power in the AZO (in dark blue) and CIGS layers (in red), and the total (sum) of both contributions (in black).

As depicted in Fig. 5.4.5(a), for a defect resistivity of $3.14 \times 10^{-5} \Omega\text{cm}^2$, the power dissipation in the CIGS layer shows a distinct peak at larger defect radii ($10 \mu\text{m}$), while the maximum power dissipation in the AZO layer forms a much smaller peak. In Fig. 5.4.5(b), with the defect resistivity decreased to $3.14 \times 10^{-7} \Omega\text{cm}^2$, the height and position of the peak power dissipation in the CIGS shift as a function of defect radius. Lower defect resistivity results in a reduced peak power magnitude and a shift towards smaller defect sizes. Conversely, power dissipation in the AZO layer increases, forming a broad peak over a wide range of defect radii. Notably, when the defect size reaches approximately $1 \mu\text{m}$, there is a significant drop in power dissipation in the AZO layer, leading to slow or no further growth in defect size, as shown earlier in green Fig. 5.4.4. Likewise, in Fig. 5.4.5(c), for the lowest defect resistivity of $3.14 \times 10^{-9} \Omega\text{cm}^2$, power

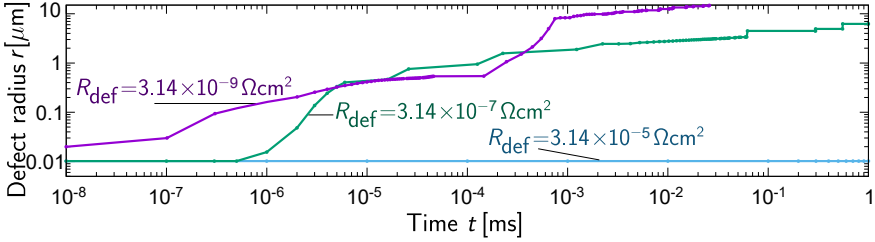


Figure 5.4.4: Growth of a defect illustrated by the change of the effective radius r as a function of time t for three defect resistance values: $3.14 \times 10^{-5} \Omega\text{cm}^2$, $3.14 \times 10^{-7} \Omega\text{cm}^2$ and $3.14 \times 10^{-9} \Omega\text{cm}^2$. For the defect resistivity of $3.14 \times 10^{-7} \Omega\text{cm}^2$ (green, baseline), a short delay shows a phase of rapid growth towards a radius of approximately $1 \mu\text{m}$ is observed, followed by a phase of relatively slower growth towards several micrometers. A lower resistivity (i.e. $3.14 \times 10^{-9} \Omega\text{cm}^2$ (purple)) results in a faster growth behavior at the initial stages and exhibits a phase of rapid growth later in time. Notably the timing when the explosive growth takes place is dependent on the R_{def} and the dissipated power in both AZO and CIGS layers. A higher resistivity ($3.14 \times 10^{-5} \Omega\text{cm}^2$ (in blue)), on the other hand, leads to no growth in the defect. The baseline in green corresponds to the defect shown in Fig. 5.4.2 and Fig. 5.4.3.

dissipation in the CIGS shifts to smaller radii with a decreased magnitude, while the maximum power dissipation in the AZO layer is higher, forming a broader plateau across a wider range of defect radii. It is important to note that in all scenarios, a significant proportion of power is dissipated in the CIGS layer at relatively smaller defect sizes, while at larger defect radii, more power tends to dissipate in the AZO layer.

The observed maxima in the power dissipation in the defect, as seen in Fig. 5.4.5, is the result of the power being limited by a low voltage over the defect when the resistance is low. As the resistance increases the power may increase. However, if the resistance increases further, the power may drop as the current through the defect decreases. The dissipated power in the AZO behaves differently as it only depends on the current through the defect, and hence it is high when the defect resistance is low and drops when the resistance increases.

The results in Fig. 5.4.5 are expected to influence the dynamics of hotspot development, as I expect that especially for small and conductive defects the power dissipation is high. As the defect increases in size, the total power dissipation in the defect decreases, and hence the rate at which the hotspot develops will decrease. For a higher defect resistance value there may be a certain defect size for which the power dissipation exhibits a maximum, which may lead to a fast hotspot development for a certain range of defect sizes. Thus, the results in Fig. 5.4.5 partly explain the very non-uniform growth rate observed in Fig. 5.4.4. Note that the results in Fig. 5.4.5 only consider the absolute electrical power deposited, i.e. not the power density.

For the baseline simulation as shown in Fig. 5.4.5(b) with a $3.14 \times 10^{-7} \Omega\text{cm}^2$,

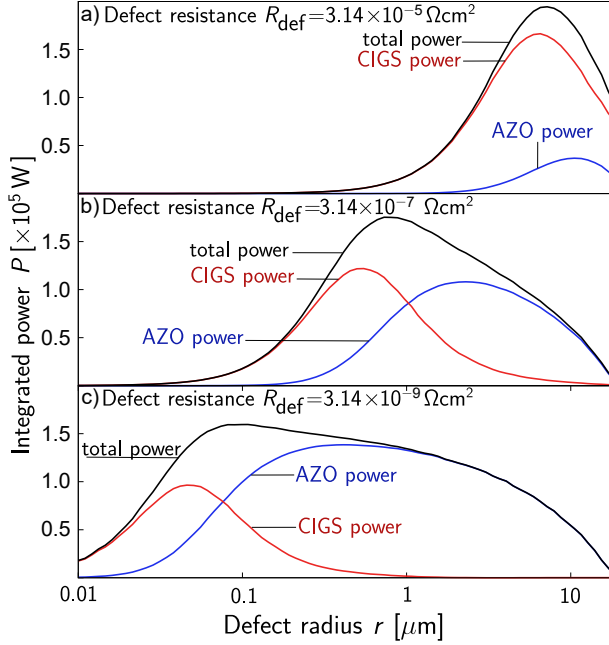


Figure 5.4.5: The dissipated electrical power obtained from the electrical model and integrated separately over the Al:ZnO (AZO) layer (dark blue) and the CIGS layer (red) as a function of the defect radius, over an area around the defect with a $20 \mu\text{m}$ radius. I vary the defect resistance to a) $3.14 \times 10^{-5} \Omega\text{cm}^2$, b) $3.14 \times 10^{-7} \Omega\text{cm}^2$ (baseline) and c) $3.14 \times 10^{-9} \Omega\text{cm}^2$. For all defect resistances, the power is predominantly dissipated in the CIGS layer for smaller radii, while the power dissipation shifts towards the AZO layer with increasing defect size. The total power (sum of power in CIGS and AZO (in black)) displays a maximum at a distinct defect radius that depends on the defect resistance R_{def} .

the total power dissipation exhibits its maximum in the region around $1 \mu\text{m}$. Nevertheless, I believe that the smaller the defect is the faster it tends to grow. To further investigate this matter I change the size of the initial defect in the simulations while keeping the defect resistance fixed at the baseline value. I specifically vary the initial defect to radii of $0.1 \mu\text{m}$, $1 \mu\text{m}$, and $5 \mu\text{m}$ while I limit the simulation time to the 1 ms as the baseline. In Fig. 5.4.6, I depict the growth process for all simulations and focus on the early stages. I notice that with 0.1 and $1 \mu\text{m}$ I obtain the same final radius as the baseline results (about $6 \mu\text{m}$ after 1 ms). However, with $5 \mu\text{m}$ I observe no change in defect size till the end of the 1 ms simulation time as the power is not sufficient to heat up the defected area to the threshold temperature of 1000 C .

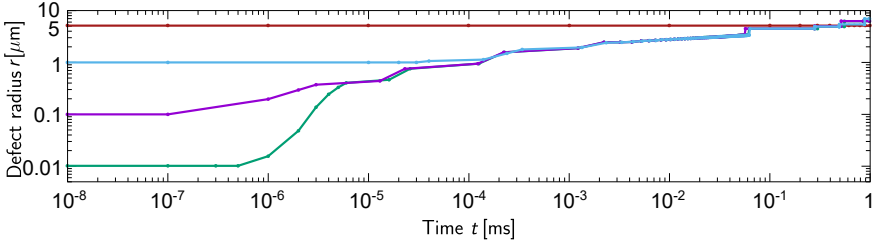


Figure 5.4.6: Growth of a defect as a function of time t due to the change in its initial radius r_0 . For all simulations, defect resistance is set to the baseline value of $R_{def} = 3.14 \times 10^{-7} \Omega\text{cm}^2$. The initial defect is varied to radii of 10 nm (green, baseline), $0.1 \mu\text{m}$ (purple), $1 \mu\text{m}$ (blue), and $5 \mu\text{m}$ (red). No remarkable difference is observed between a radius of 10 nm, $0.1 \mu\text{m}$ and $1 \mu\text{m}$, where in all three cases, after the small defect reaches a radius around $1 \mu\text{m}$, a slower growth is observed similar to the behavior of the baseline (in green) in Fig. 5.4.4, resulting in a defect size of $6 \mu\text{m}$ at the end of the 1 ms. No change in size is observed for the large defect with radius of $5 \mu\text{m}$.

5.5 Discussion

As discussed in Section 5.3.1, I assume a seed defect which gives rise to a positive feedback effect and a thermal runaway. Also in the absence of a shunt-like defect such a positive feedback effect is observed in CIGS solar cells under reverse bias, as previously discussed in Chapters 3 and 4. Thus I argue, the initial defect leading to a hotspot and permanent damage, does not need to be a shunt-like defect. Possibly, early junction breakdown caused by microscopic defects, such as observed in microcrystalline silicon [97], triggers this positive feedback effect leading to a thermal runaway and the creation of the small initial shunt-like defect.

In light of these considerations, I propose a 3 phase process leading to worms in CIGS: the "nucleation" phase, the "growth" phase, and the "wandering" phase. In the first nucleation phase, the thermal activation of the junction breakdown current in CIGS, as experimentally demonstrated in Ref. [50], leads to instability and a thermal runaway starts to develop. The first phase ends when the temperature is high enough for thermal decomposition to take place, and the CIGS segregates, producing at least one conductive phase [5, 17]. At this point, the process becomes irreversible and a shunt-like defect emerges. In the second growth phase, the shunt-like defect grows from a small initial defect to a defect with a diameter in the order of micrometers. This phase is covered by this chapter. In the third and final wandering phase, the defect starts to propagate through the solar cell. This last phase will be further discussed upon in Chapter 6.

5.6 Summary

In this chapter I explain the, experimentally shown, short timescales in which a hotspot may form in CIGS solar cells under reverse bias. To this end I developed an electro-thermal FEM model with a high spatial and temporal resolution. This way I demonstrated that the experimentally observed time scales for hotspot development are reproduced when assuming a small initial defect size of 10 nm. With such a small initial defect, the experimentally observed final size of the defect (i.e. $5\ \mu\text{m}$), develops within 1 ms. To achieve these results, with the coupled electro-thermal FEM model, I investigated the unknown material properties including defect resistivity, as well as the initial defect size, while all other parameters in the solar cell are taken from literature.

Notably, I observed a significant interplay between the defect size, defect resistivity, and the amount of power deposited at the defect. I demonstrate that there is a maximum in the deposited power which depends on the defect resistivity and radius, where a more conductive defect has its maximum in deposited power at a smaller radius. It is expected that this coupling between defect resistivity and defect size affects the dynamics of the defect evolution, and partly explains the non-uniform growth rate I observe in simulations. However, due to the experimental nature of the study, my understanding of the growth process at $t \ll 1\ \text{ms}$ is restricted. Nevertheless, I can still anticipate potential coupling scenarios that result in the experimental defect size at $t = 1\ \text{ms}$. Finally, I propose a 3-phase mechanism for the creation of worms consisting of "nucleation", "growth", and "wandering". In the nucleation phase, junction breakdown (possibly an early breakdown at microscopic electronic defects) trigger a positive feedback loop leading to thermal runaway and material decomposition, creating a small initial shunt-like defect. In the growth phase, this defect grows larger (by the mechanisms described in this work). In the final phase, the defect starts to wander through the solar cell, leading to a worm-like defect.

Impact of Encapsulation, Substrate, and Defect Location on Reverse Bias Damage in CIGS Solar Cells

In Chapter 5, I presented a finite element method (FEM) model to describe the dynamics of reverse bias damage development in CIGS solar cells. Building upon this foundation, the current chapter investigates how various properties of different layers within the solar cell stack, as well as the spatial location of defects, influence defect growth using the established model.

The analysis begins by exploring the influence of material characteristics in specific layers of the solar cell stack, including the glass substrate and the encapsulation layer. In addition, I examine the role of defect location within the cell, with a focus on edge-based defects. These investigations are motivated by earlier experimental findings (Section 4.2 and Section 4.1), which highlighted the significant impact of thermal properties and hotspot positioning on the positive feedback mechanisms preceding defect formation. By extending this analysis, I aim to provide deeper insights into the interplay between material properties, defect positioning, and reverse bias damage progression in CIGS solar cells.

This chapter is organized as follows:

- **Section 6.1** focuses on the impact of encapsulation. Specifically, it examines the case of an unencapsulated solar cell and compares the results to those obtained for an encapsulated cell, as presented in Chapter 5.
- **Section 6.2** investigates the influence of the substrate material by comparing a glass substrate with a steel foil substrate.
- **Section 6.3** explores the effect of defect location on growth dynamics. In this section, defect locations are systematically varied, including positions near the P1 line and the P3 line. The results are then compared to those for a defect located near the center of the cell, which serves as the baseline scenario analyzed in Chapter 5.

6.1 Impact of Encapsulation

The encapsulation of a CIGS solar cell involves adding a layer of encapsulation material. These materials are typically polymers, which exhibit poor thermal conductivity [3, 98]. Since the encapsulation material is in direct contact with the thin-film device, it is expected to significantly impact the development of hotspots.

Mansfield *et al.* [99] investigated the reverse bias damage reliability concerns in CIGS photovoltaics at the cell level, focusing on shading-induced damage. Their findings highlighted the impact of encapsulation on defect formation and thermal runaway. They observed that encapsulated cells showed higher susceptibility to reverse bias stress and were damaged at lower reverse voltages compared to non-encapsulated cells [99]. Furthermore, their study referenced a simulation by Nardone *et al.* [19], which indicated that an encapsulated module reached thermal runaway temperature five times faster than an unencapsulated one [99]. However, comparing these findings with Nardone *et al.*'s model results is challenging due to differences in substrate composition: the experimental samples used by Mansfield *et al.* [99] incorporated a glass substrate, while Nardone *et al.*'s [19] thermal model did not include this layer in its stack ².

On the other hand, Vaas *et al.*'s work [57] demonstrated that non-encapsulated CIGS solar cells are more susceptible to reverse bias stress induced by partial shading compared to encapsulated cells [57]. This finding directly contradicts Mansfield *et al.*'s conclusions. Vaas *et al.* used industrially produced samples, with some encapsulated and others not. He observed more distinct differences in breakdown behavior: non-encapsulated samples were more likely to form defects at cell interconnections, while encapsulated cells more often developed defects further away from the interconnection lines [57].

Given these contradictory findings in the literature, the role of encapsulation in hotspot formation and reverse bias stress in CIGS solar cells remains unclear. The discrepancies in experimental results and modeling approaches have led to conflicting conclusions. It should also be noted that, experimentally, it is often difficult to isolate the effects of encapsulation from other cell properties, as the encapsulation process itself may alter the properties of the CIGS solar cell. Furthermore, especially for non-encapsulated cells, the results may be influenced by the experimental conditions, such as forced convection.

Using the FEM model, I can clearly separate such effects and establish the impact of encapsulation without altering any other properties. In this work, the EVA layer is removed from the FEM model presented in Chapter 5 (which includes the glass substrate in the layer stack). For the cell-air interface, I assume properties corresponding to a convection-free case.

²As discussed earlier in Section 4.2, I demonstrated the significant impact of the substrate (i.e. glass vs. steel substrates) on the loop gain and, consequently, the dynamics of reverse bias damage creation.

Results and discussion

The model for the purpose of this section replicates the parameters of the baseline model described in Section 5.4. The simulation duration remains 1 ms, initiated with a defect of 10 nm radius. Both thermal and electrical properties of the layers stack are listed in Table 5.1 and 5.2, respectively. While the defect resistance is set to $3.14 \times 10^{-7} \Omega\text{cm}^2$.

The sole modification is the removal of the encapsulation layer on top of the layer stack. Without the EVA, the solar cell can dissipate heat directly to the surrounding air through convection. In this scenario, the thermal properties of air become crucial. As discussed in Section 5.3.3, heat loss to air in a convection free environment is approximated using $b = 12 \text{ Wm}^{-2}\text{K}^{-1}$ [93].

Figure 6.1.1 depicts the results when the defect has reached its final size. Figure 6.1.1(a) shows the temperature profile at the middle of the CIGS layer from the thermal model. Figure 6.1.1(b) depicts the defect shape from the electrical model. While Fig. 6.1.1(c) and Fig. 6.1.1(d) show the electrical power dissipated in the AZO layer and in the CIGS layer, respectively. Figs 6.1.1(a) and 6.1.1(b) show that an area with a radius of $8.5 \mu\text{m}$ has reached a temperature of 1000°C after 0.84 ms. This size is larger and more irregular than the encapsulated case (i.e. as detailed in Chapter 5, the encapsulated scenario reached a smaller radius of $6.2 \mu\text{m}$). Additionally, Figs 6.1.1(c) and 6.1.1(d) show weak electrical power, insufficient to cause further defect growth. After this time (0.84 ms) until the final time of 1 ms, there is no more expansion of the defect beyond the $8.5 \mu\text{m}$ radius.

To better visualize and compare the defect growth dynamics, Fig. 6.1.2 presents a time-based comparison of defect growth in both encapsulated (in green) and non-encapsulated (in purple) scenarios. This plot reveals that the defect growth patterns are similar in both cases for most of the simulation period. However, a significant divergence occurs near the end of the 1 ms time frame, where the non-encapsulated case exhibits faster growth.

The initially similar dynamics in the encapsulated and non-encapsulated scenarios are expected, as the hotspot initially develops below the AZO layer. During this phase, there is no heat conduction across the AZO/EVA or AZO/Air interfaces. The deviation only occurs toward the end of the 1 ms time frame, where, in the absence of encapsulation, the defect grows larger compared to the encapsulated case. Specifically, the defect expands by approximately $2 \mu\text{m}$ more at the end of the 1 ms period in the non-encapsulated scenario. It is expected that beyond 1 ms the results will deviate more as the front of the AZO heats up and thus the heat conduction across the AZO/EVA or AZO/Air interfaces affects the outcome more and more.

The difference in outcomes can be attributed to the thermal properties of air and EVA. The convection coefficient for air is such that less heat is extracted from the AZO compared to the encapsulated case, leading to more localized heating in the non-encapsulated scenario. This conclusion aligns well with Vaas *et al.*'s experimental findings, which showed that non-encapsulated CIGS solar cells were more prone to reverse bias damage than encapsulated cells [57].

While these results suggest a clear difference in defect size between the

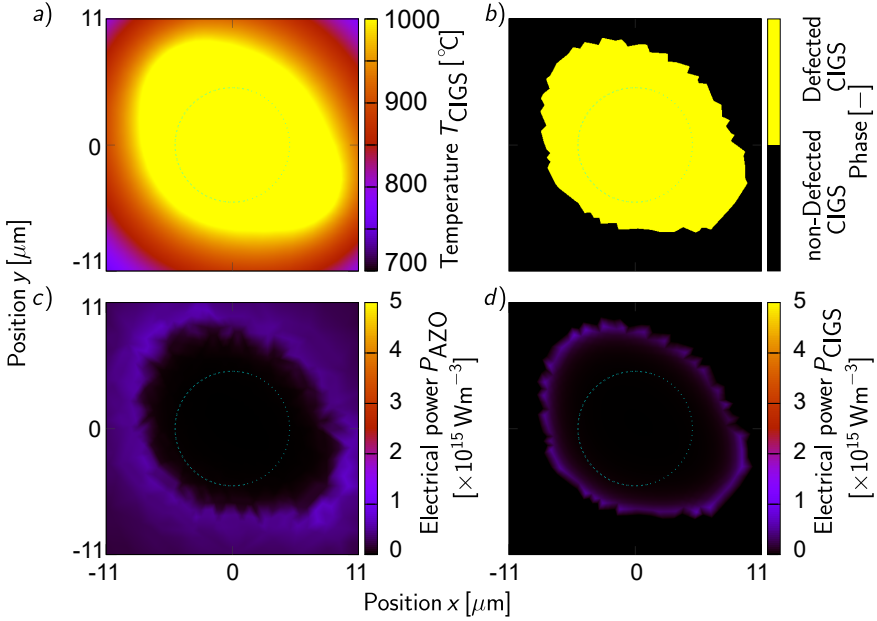


Figure 6.1.1: a) Temperature distribution profile at the middle of CIGS layer, b) phase plot, c) AZO power profile, and d) CIGS power distribution. The current is injected from the top edge of the cell. The defect has reached a radius of around $8.5 \mu\text{m}$ after 0.84ms as depicted in a) and b), while the cyan circle indicates a radius of $5 \mu\text{m}$. The power in c) d) shows low dissipated electrical power in both AZO and CIGS, respectively, leading to no further growth of the defect till the end of the 1ms simulation time. The larger defect size is to the absence of the encapsulation layer as EVA has higher thermal resistance than air leading to more localized heating.

encapsulated and non-encapsulated scenarios, it is important to consider the potential influence of the simulation methodology on these findings, particularly the assumed convection coefficient. For example, in a scenario where there is forced convection during the experiments the outcome may be different. This may offer an explanation for the contradicting results found in literature.

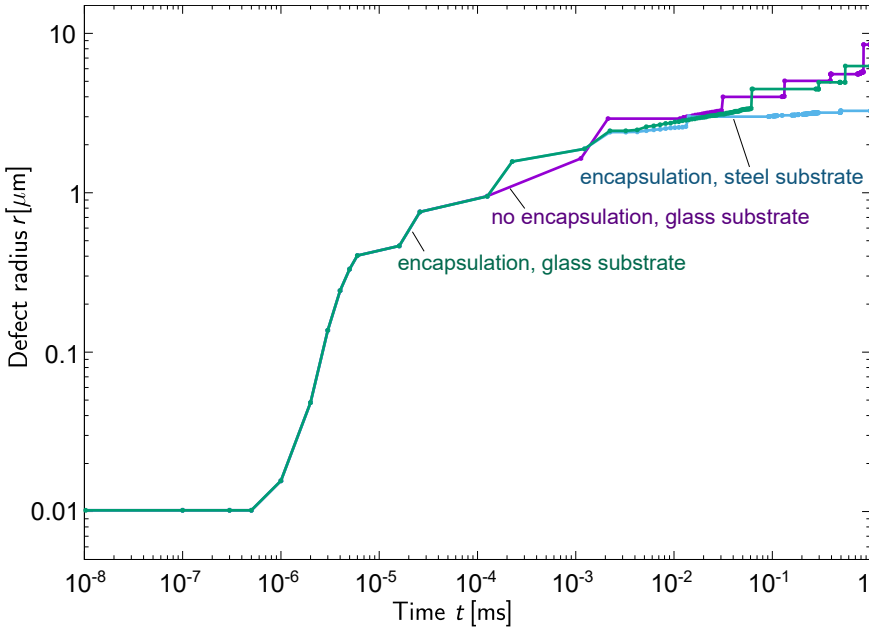


Figure 6.1.2: Growth of a defect illustrated by the change of the effective radius r as a function of time t for various scenarios; baseline (encapsulated, glass substrate, green), (non encapsulated, glass substrate, purple), and (encapsulated, steel substrate, blue). All different scenarios have the same thermal and electrical properties, including a resistance of defected CIGS (R_{def}) of $3.14 \cdot 10^{-7} \Omega\text{cm}^2$, and an initial defect of 10 nm . All simulations after a short delay show a phase of rapid ("explosive") growth towards a radius of approximately $1 \mu\text{m}$ followed by a phase of relatively slower growth towards several micrometers. The baseline case in green (i.e. encapsulated CIGS cell with a glass substrate) has reached a radius of $6.2 \mu\text{m}$ at 1 ms . Removing the encapsulation layer (in purple) makes the growth a bit faster and to a larger size, of $8.2 \mu\text{m}$ radius at 1 ms . Meanwhile, replacing the glass substrate with thin steel foil (in blue) makes the growth slower, where the defect does not grow much, reaching only a radius of $3.64 \mu\text{m}$ at 1 ms .

6.2 Impact of Substrate

The substitution of the glass substrate with thin steel foil is of particular interest due to the potential benefits of steel foils, such as increased flexibility and durability, which could significantly advance CIGS solar cell technology. While extensive research has been conducted on flexible CIGS cells [4, 83, 84], the impact of replacing glass with thin steel foils on hotspot formation and growth mechanisms in CIGS solar cells remains an open question.

Replacing the traditional glass substrate with thin steel foil may have significant implications for the hotspot growth mechanism. The difference in thermal properties, particularly thermal conductivity, between glass and steel may influence the solar cell's overall thermal behavior and reshape the growth of hotspots. In Section 4.2.1, it was found that the measured electro-thermal loop gain for a hot spot is significantly lower for CIGS on steel foil than for samples on glass. This observation could be explained by the higher thermal conductivity of steel. However, as the cells were prepared differently, it is difficult to make definitive statements about the specific impact of the steel foil alone.

In this section, I aim to analyze how thin steel foil impacts the growth of pre-existing defects in the CIGS absorber layer. Similar to the removal of the EVA layer in the simulations of the previous section, the FEM simulation model allows us to isolate the impact of the steel foil.

Results and discussion

Glass and stainless steel foil exhibit distinct thermal properties with notable differences, which can significantly affect heat dissipation and defect growth in solar cells. Glass (properties are listed in Table 5.1) is characterized by low thermal conductivity, a relatively low coefficient of thermal expansion, and a higher specific heat capacity. It is less efficient in heat transfer compared to metals like stainless steel. Additionally, the melting point of glass is generally higher than that of stainless steel [94].

From literature, stainless steel has a density of 8000 kgm^{-3} , a thermal conductivity of $16.2 \text{ Wm}^{-1} \text{ K}^{-1}$, and a heat capacity of $50 \text{ Jkg}^{-1} \text{ K}$ [94]. Hence, steel foil possesses higher thermal conductivity and a higher coefficient of thermal expansion, conducting and transferring heat more effectively, albeit with a lower specific heat capacity [94].

These differences in thermal properties between the two materials have implications for their use as substrates in CIGS solar cells, where considerations such as heat dissipation is a crucial factor on defects growth. To investigate this substitution, I used the FEM model detailed in Chapter 5 with the same parameters for the layer stack as the baseline model described in the previous chapter (i.e. with a shunt resistance of $3.14 \times 10^{-7} \text{ } \Omega \text{ cm}^2$), but with replacing the glass substrate with steel foil that is a factor 30 thinner (i.e. steel foil is set to 0.1 mm thick). The simulation duration remains 1 ms, initiated with a pre-existing defect of 10 nm radius.

Similar to Fig. 6.1.1, Fig. 6.2.1 depicts the results when the defect has reached its final size. Figure 6.2.1(a) shows the temperature profile at the

middle of the CIGS layer from the thermal model. Figure 6.2.1(b) depicts the defect shape from the electrical model. Fig. 6.2.1(c) and Fig. 6.2.1(d) show the electrical power dissipated in the AZO layer and in the CIGS layer, respectively. Figure 6.2.1(a) and (b) show that the defect has reached a radius of only $3.26 \mu\text{m}$ at 0.49 ms . From that point on till the end of the 1 ms period, there was no more growth of the defect despite the relatively high dissipated electrical power in AZO and CIGS as depicted in Fig. 6.2.1(c) and (d), respectively. This means that the generated heat got dissipated significantly through the steel foil due to its high thermal conductivity and low thermal resistance. Moreover, the comparison to glass shows a reduction in defect size by almost half (i.e. the defect in the glass substrate case reached a radius of $6.2 \mu\text{m}$).

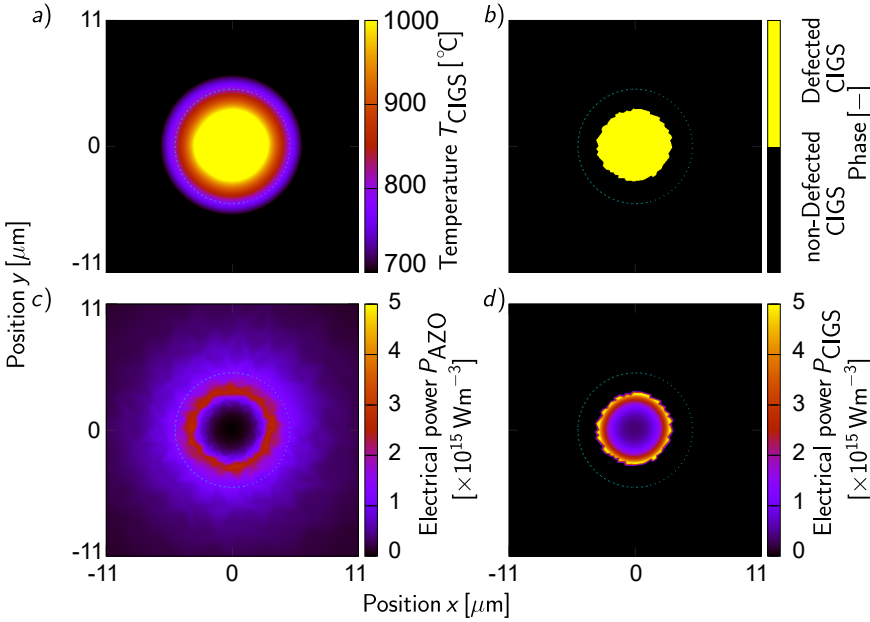


Figure 6.2.1: a) Temperature distribution profile at the middle of CIGS layer, b) phase plot, c) AZO power profile, and d) CIGS power distribution. The defect had an initial radius of 10 nm and resistivity of $3.14 \times 10^{-7} \Omega\text{cm}^2$, while the glass substrate was replaced with a thin steel foil. The defect has reached a radius of around $3.26 \mu\text{m}$ at the end of 1 ms . The current is injected from the top edge of the cell. Cyan circle indicates a radius of $5 \mu\text{m}$.

Furthermore, Fig. 6.1.2 illustrates the defect growth over time for the case where steel foil (in blue) is used as the substrate, in comparison to the simulation with a glass substrate (in green). The graph shows that initially, the defect experiences similar explosive growth, reaching a radius of $1 \mu\text{m}$. However, with the steel foil substrate, the growth rate subsequently slows down and stops at a radius of $3.26 \mu\text{m}$, remaining unchanged for the duration of the simulation.

The initially similar dynamics of defect evolution for both cells on glass and

steel foil can be explained by the fact that the initial hotspot is some distance away from the substrate. Only after the heat reaches the cell/substrate interface does the substrate begin to influence the dynamics. The results suggest that the higher thermal conductivity of steel can indeed mitigate the effects of reverse bias damage, as the damage growth is inhibited. However, it should be noted that the initially identical dynamics indicate that a steel foil substrate cannot *prevent* the damage as such.

This argument also affects the interpretation of HS-LIT measurements, as introduced in Chapter 3. In HS-LIT, the laser-induced hotspot is created at the location where the laser power is absorbed, meaning that the measured loop-gain may not always reflect the loop-gain governing reverse bias damage. In this context, the lower measured loop-gain on a steel substrate compared to a glass substrate in Section 4.2.1 is likely more indicative of the inhibited defect growth, rather than the initial defect creation.

6.3 Impact of defect location

In Section 4.1.1, it was found that the position of the hotspot within the cell can significantly affect the observed loop-gain. Various effects could explain this observation; however, in Section 4.1.1, I have already shown that electrical effects, particularly the AZO sheet resistance and the resulting current limitation toward the hotspot, greatly influence the loop-gain. Thus, it is expected that the same effect will also impact the defect growth dynamics.

In addition to these electrical effects, the scribing lines also introduce changes in thermal properties, as the P1 line interrupts the back contact layer and the P3 line interrupts the AZO and CIGS layers. All these effects can be incorporated into the FEM model to investigate the location-dependent defect growth dynamics.

Defect at P1 scribe line

To shift the defect to the P1 scribe line, some modifications were made to the electro-thermal model, as sketched in Fig. 6.3.1, as follows:

- **Thermal Model:** The defect itself remains at the center of the thermal model. However, the material structure is redefined in terms of layer stack properties to replicate the edge of an active cell. A $50\ \mu\text{m}$ wide stripe of CIGS is introduced along the depth at the P1 scribing line, replacing Mo in that specific area. All other layers remain unchanged.
- **Electrical Model:** The initial defect's location is shifted from the center of the rectangular cell to the top edge (i.e., the Dirichlet boundary of the electrical model, where a voltage is applied). The coordinate axes were repositioned as well, to maintain their origin at the center of the defect, and ensure the coordinates of the two models match.
- **Mesh Resolution:** Both electrical and thermal models employ higher-resolution meshing than the baseline model in and around the defect.

The remaining details of the coupled model stays the same as described in Chapter 5 with the same parameters for the layer stack as the baseline model described in the previous chapter. The simulation duration remains 1 ms, initiated with a pre-existing defect of 10 nm radius.

To better understand the growth behavior of a defect at the P1 line, Fig. 6.3.2 depicts a cross-sectional temperature profile along the depth of the layer stack at $t = 1.02 \times 10^{-5}$ s. Notably, the defect exhibits asymmetrical growth, with a larger size on the active cell side ($y < 0$) compared to the opposite side, despite the defect having the same material properties on both sides at the absorber layer level (i.e., CIGS).

In this scenario, the defect is located at the cell's edge, where power is applied within the electrical model. Consequently, one side of the thermal model experiences growth driven directly by this power input, while the opposite side relies solely on heat diffusion from the powered side. This results in irregular

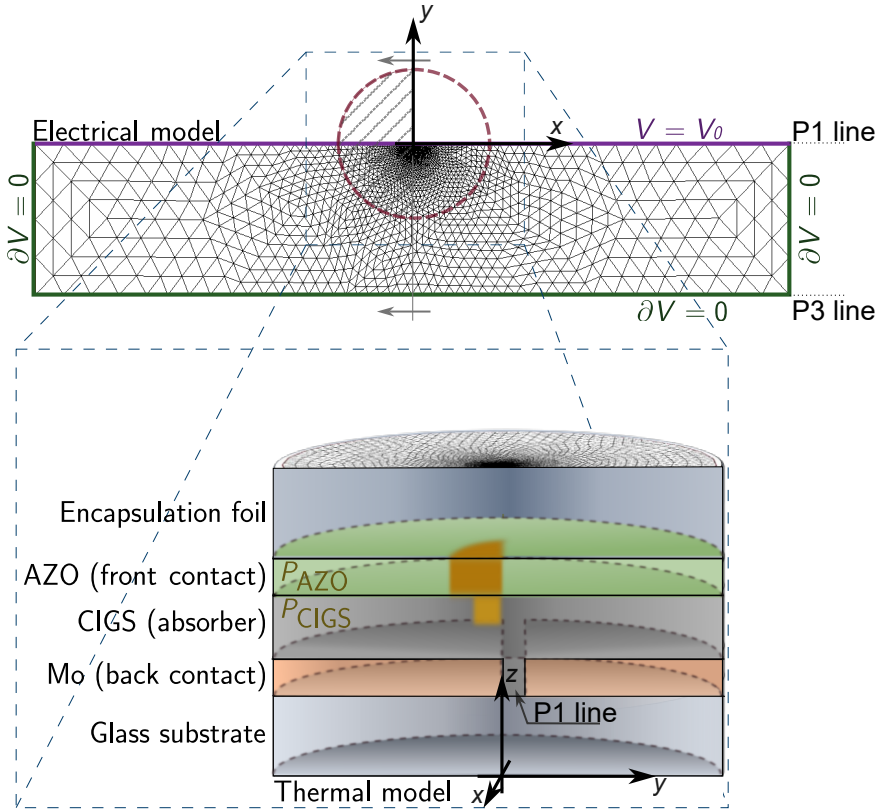


Figure 6.3.1: A schematic illustration of the modified generated mesh for both electrical and thermal models, when the defect is shifted to P1 scribe line. The electrical model has a rectangular domain with dimensions of $0.4\text{ cm} \times 2\text{ cm}$, while the thermal model is cylindrical with a diameter equals the width of the cell (i.e. 0.40 cm), and a depth equals the thickness of all layers in the stack as in Table 5.1. The initial defect with a radius of 10 nm is located along the top long edge of the cell in the electrical model, where the electrical power is deposited. In the thermal model, the defect stays at the center of the cylindrical domain. However, Mo is replaced by CIGS for a width of $50\text{ }\mu\text{m}$ replicating a P1 scribe line.

growth patterns, with one side growing more rapidly than the other due to the uneven distribution of electrical power.

For simplicity, the Dirichlet boundary of the electrical model is placed at $y = 0$. As a result, there is no power dissipation at all in the CIGS layer stack, nor in the AZO layer for $y > 0$. While this setup simplifies the model, it is not entirely realistic, as current would flow within the AZO layer. Thus, the asymmetry in these simulations is somewhat exaggerated. Additionally, some of the asymmetry may also be attributed to the absence of the molybdenum

contact layer.

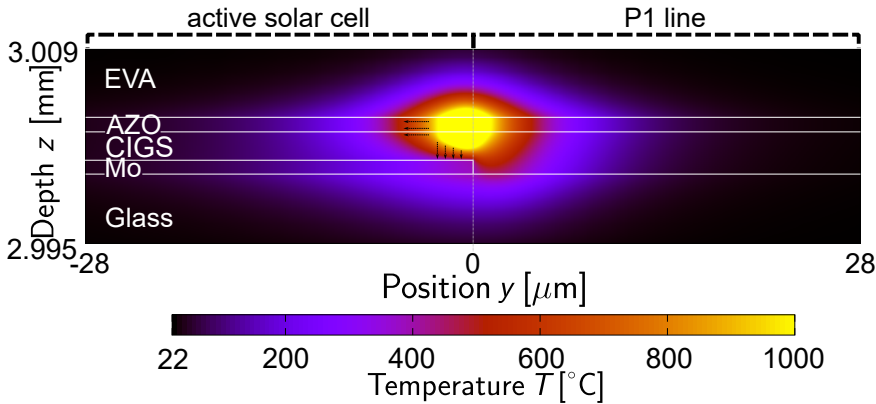


Figure 6.3.2: A cross section in the simulated cell showing the thermal profile and temperature distribution for the layer stack near P1 scribe line. The defect exhibits asymmetrical growth, with larger size on the active cell side compared to the other side (P1 scribe line). At P1 scribe line, one side of the thermal model experiences growth driven by this direct power input, while the opposite side relies solely on heat diffusion from the first side. This results in irregular growth patterns, with one side growing more rapidly than the other due to the uneven distribution of electrical power.

For more details, Fig. 6.3.3 depicts the results at the end of the 1 ms simulation. Figure 6.3.3(a) shows the top view of the defect from the thermal model at the middle of CIGS layer, this view includes both the active cell as well as the P1 scribe line area. The phase plot in Fig. 6.3.3(b), however, depicts the defect in the active solar cell side only as the electrical model is limited to this region. Additionally, Fig. 6.3.3(c) and Fig. 6.3.3(d), shows the Power in both AZO and CIGS from the active cell side, respectively.

The top view in Fig. 6.3.3(b) reveals that the defect expands more than twice as far in the x -direction as in the y -direction, despite both sides being composed of CIGS material. This asymmetrical growth results in an oval shape for the defect, with a horizontal (x -direction) radius of nearly $3.9 \mu\text{m}$. In the y -direction, I can distinguish between the direction into the cell ($y < 0$) and into the P1 scribe ($y > 0$). The maximum extent of the defect in the active cell reaches $-2.5 \mu\text{m}$, while into the P1 scribe line it extends to $1.5 \mu\text{m}$.

In addition, Fig. 6.3.3(c) shows that all power within the AZO layer concentrates at the edge of the defect that is in contact with the edge of the cell, creating a steep gradient that diminishes to zero as one moves away from this edge. This concentration of power at the edge restricts the defect's growth in the y -direction due to the limited power pathways. However, some power accumulation occurs at the corners, allowing for further expansion in the x -direction and contributing to the oval shape. Similarly, Fig. 6.3.3(d) illustrates a concentration of power at the edge of the defect in the CIGS layer as power transfers

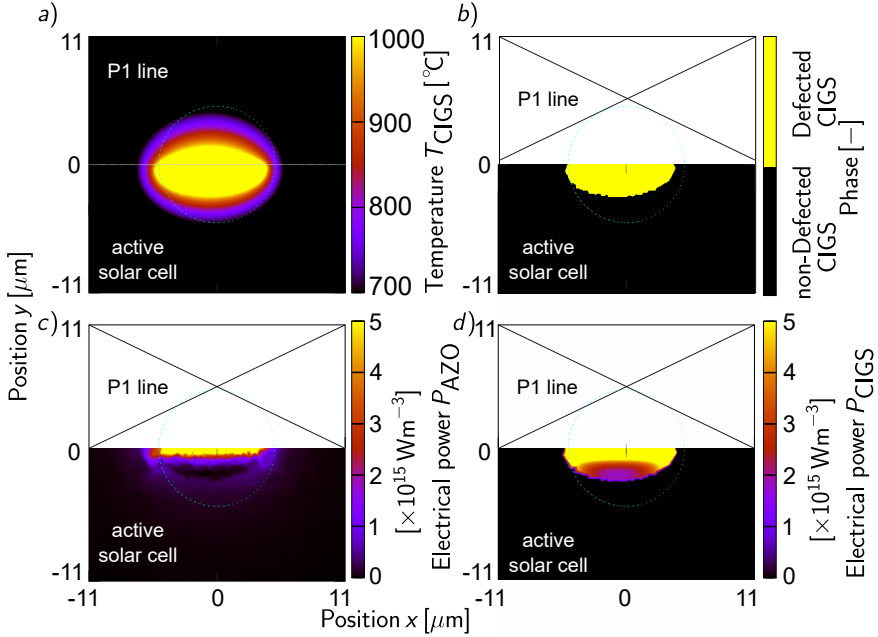


Figure 6.3.3: a) Temperature distribution profile at the middle of CIGS layer, b) phase plot, c) AZO power profile, and d) CIGS power distribution, when the defect is located at P1 scribe line. One side of the defect expands to an area (extent of $-2.5 \mu\text{m}$) more than twice that of the other half (extent of $1.5 \mu\text{m}$), despite both sides being composed of CIGS material. Cyan circle indicates a radius of $5 \mu\text{m}$. The power is deposited at P1 scribe line into the active cell, and is concentrated at the edge of the active cell creating a steep decrease away from the edge of the defect in both AZO and CIGS layers.

vertically, but with a less pronounced gradient. These results indicate that if a defect is located at the P1 edge of the cell, it is unlikely to grow significantly into the cell but will instead expand along the P1 line. This phenomenon, where defects wander along the P1 scribe, has been observed in literature [6].

Defect at P3 scribe line

To relocate the defect to the other side of the cell (i.e. at P3 scribe line), the following modifications in both electrical and thermal models are applied, as sketched in Fig. 6.3.4:

- **Thermal Model:** The defect remains at the center of the circular thermal mesh. Instead, the material structure is reconfigured based on the properties of the layer stack to simulate the edge of an active cell near the P3 scribe line. Specifically, a $50 \mu\text{m}$ wide stripe of EVA is substituted for both AZO and CIGS along the depth at the P3 scribing line, while all other layers stay the same.

- **Electrical Model:** The initial defect's location is shifted from the center of the rectangular cell to the bottom edge, away from where the power is deposited. The axes were also shifted to maintain their origin at the center of the defect and ensure the coordinates of the two models match.
- **Mesh Resolution:** For this simulation, I find that the defect grows particularly asymmetrically and over a large distance, necessitating continuous remeshing of the electrical model. Figure 6.3.5 illustrates the electrical model mesh at various simulation points, using the `freefem++` command `remesh`. As shown in Fig. 6.3.5(a), the simulation begins with an electrical mesh refined using a logarithmic spatial distribution, providing high resolution in and around the defect. However, as the defect grows larger, it extends into coarser regions of the mesh. Consequently, the electrical model must be continuously remeshed based on the potential solution to maintain high resolution in the vicinity of the defect throughout the simulation, as depicted in Fig. 6.3.5(b) and (c). Meanwhile, the thermal model uses a single mesh but employs a higher resolution than the baseline model in and around the defect.

Figure 6.3.6 presents a cross-section of the layer stack from the thermal model at $t = 1.78 \mu\text{s}$. The temperature distribution indicates that the defect is growing laterally into the solar cell and away from the P3 scribe. Since EVA is a poor heat conductor, the heat gradient is steep toward the P3 line.

To have an overview regarding the growth dynamics, Fig. 6.3.7 shows the defect's growth into active part of the solar cell over time. In this figure, (a), (e), (i), (m) and (q) present the top views of the defect from the thermal model at the middle of the CIGS layer, while the phase plots in (b), (f), (j), (n) and (r) depict the corresponded shape of the defect, respectively. Furthermore, (a), (e), (i), (m) and (q) show the electrical power in CIGS layer, while (b), (f), (j), (n) and (r) depict the power in AZO layer, respectively.

As shown in Fig. 6.3.7(a), the defect initially has a circular uniform heat distribution leading to a small half circle-shape in the phase plot depicted Fig. 6.3.7(b) at $t = 0.28 \mu\text{s}$. In Fig. 6.3.7(c), high electrical power densities are observed within the defect in the CIGS layer, as the power is generated in the CIGS layer itself. Meanwhile, the power in AZO layer, as depicted in 6.3.7(d), increases toward the defect then drops gradually to zero within it. As time progresses to $t = 0.88 \mu\text{s}$, as shown Fig. 6.3.7(e), the defect does not maintain a uniform circular heat distribution, leading to a larger, non-uniform region with a semi-circular shape in the phase plot shown in Fig. 6.3.7(f). In the electrical model, however, it is observed that most of the current flows into the defect from the side opposite to the P3 line. This results in asymmetric power dissipation, with higher concentrations on one side of the defect in both the CIGS and AZO layers, as seen in Fig. 6.3.7(g) and (h). Consequently, the highest temperatures develop along this half-ring of the defect. In Fig. 6.3.7(i), I observe this effect more clearly as the defect is significantly cooler at the P3 facing side, resulting in a defect growth primarily in the y -direction toward the P1 line. In the x -direction, the defect does not expand. This uneven

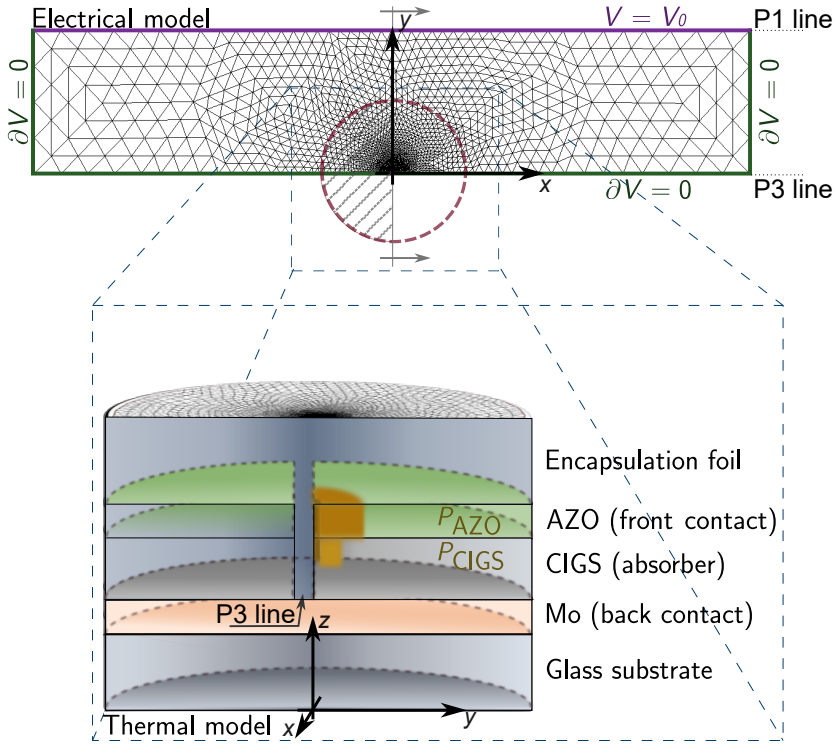


Figure 6.3.4: A schematic illustration of the modified generated mesh for both electrical and thermal models, when the defect is shifted to P3 scribe line. The electrical model has a rectangular domain with dimensions of $0.4 \text{ cm} \times 2 \text{ cm}$, while the thermal model is cylindrical with a diameter of 0.40 cm , and a depth equals the thickness of all layers in the stack as in Table 5.1. The initial defect with a radius of 10 nm is located along the bottom long edge of the cell in the electrical model, away from the power. In the thermal model, the defect remains in the center of the domain. However, both AZO and CIGS are replaced by EVA for an area of $50 \mu\text{m}$ wide to mirror a P3 scribe line.

temperature distribution results in a slightly elongated shape for the defect, as depicted in Fig. 6.3.7(j). Additionally, lower but unevenly distributed power densities are observed in both CIGS (Fig. 6.3.7(k)) and AZO (Fig. 6.3.7(l)), with maximum power concentration occurring at the defect's tip. Later on, as plotted in Fig. 6.3.7(m), (n), (q) and (r), the defect develops a propagating tip away from the P3 line toward the source of the current (P1 line). This directional growth is also reflected in the power distribution, where the maximum power remains concentrated at the tip of the defect, as depicted in in Fig. 6.3.7(o), (p), (s), and (t). In Fig. 6.3.7(r), it is observed that the defect reaches approximately $13.5 \mu\text{m}$ into the cell after $18.5 \mu\text{s}$. Thus the defect propagates at a rate of approximately 0.73 m/s .

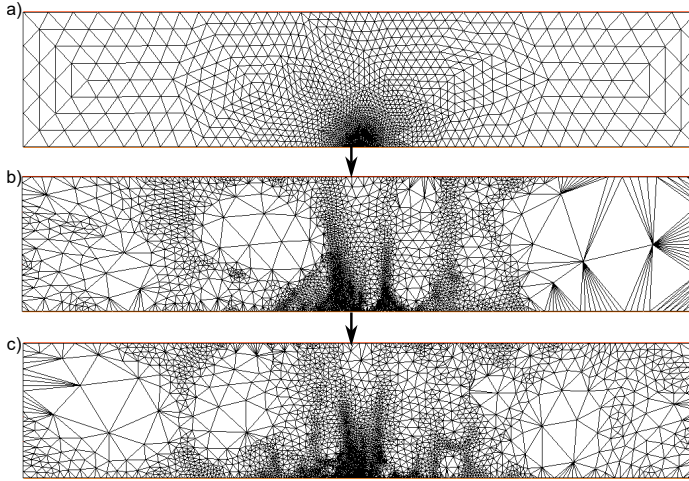


Figure 6.3.5: A schematic illustration for various regenerated meshes of the electrical model throughout the simulation. The electrical model has a rectangular domain with dimensions of $0.4 \text{ cm} \times 2 \text{ cm}$. The initial mesh in (a) is resolved using logarithmic spatial distribution. Afterwards in (b) and (c), the potential solution-from the electrical model-is used to remesh the electrical model, ensuring a high resolution in the vicinity of the defect area as the defect grows with time.

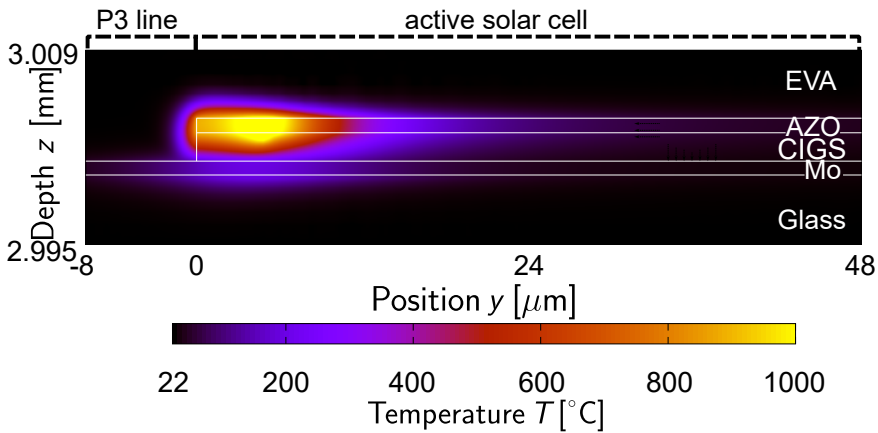


Figure 6.3.6: A cross sections in a CIGS solar cell showing the thermal profile for the layer stack, when the defect, with an initial radius of 10 nm and resistivity of $3.14 \times 10^{-7} \Omega \text{ cm}^2$, has reached a length of around $5 \mu\text{m}$ at $t = 1.78 \mu\text{s}$. The defect shows asymmetrical growth between the two side of the P3 scribe line. No growth is observed in P3 line where the encapsulation foil is present. However, the defect exhibits high temperature distribution ($T > 1000 \text{ }^\circ\text{C}$) in the active cell, indicating that the defect is growing in a single direction reaching a length of $5 \mu\text{m}$ at $t = 1.78 \mu\text{s}$.

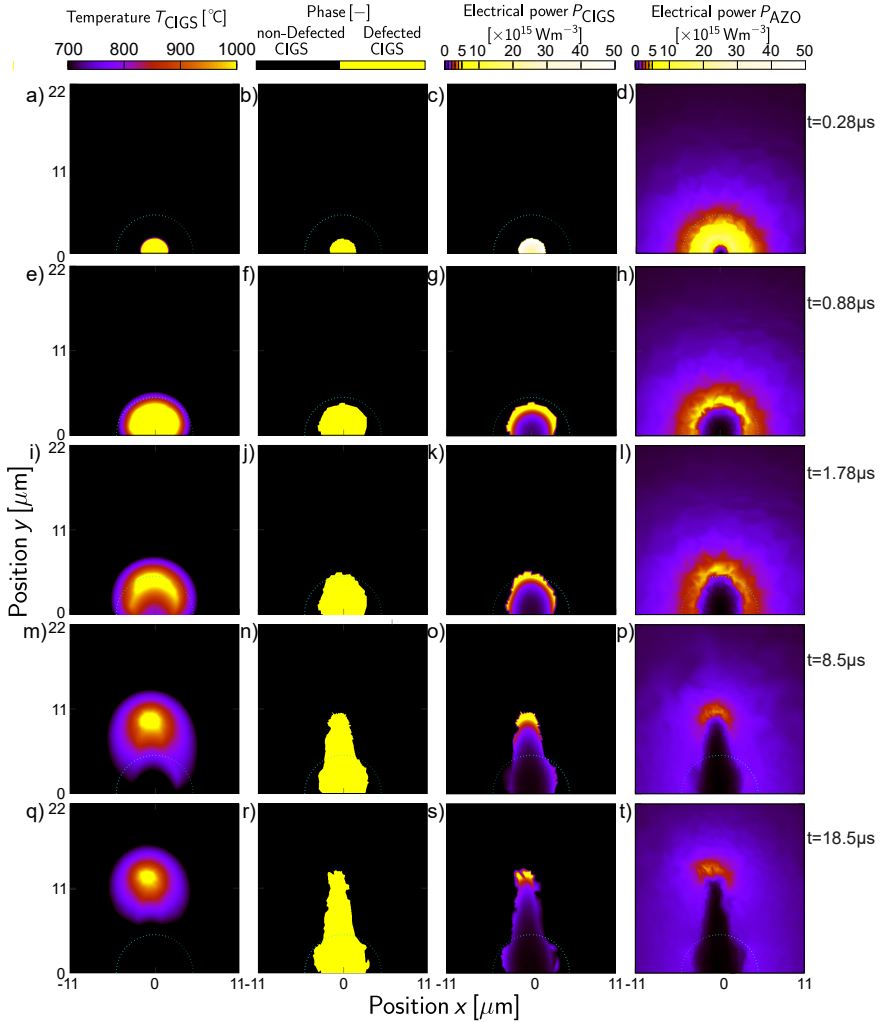


Figure 6.3.7: Evolution of the defect over time in terms of temperature, phase, and power distribution. a) e) i) m) q) Temperature distribution profile at the middle of CIGS layer, and b) f) j) n) r) phase plot c) g) k) o) s) CIGS power profile, and d) h) l) p) t) AZO power distribution, after $0.28 \mu\text{s}$, $0.88 \mu\text{s}$, $1.78 \mu\text{s}$, $8.5 \mu\text{s}$, and $18.5 \mu\text{s}$, respectively. Initially, the defect appears as a regular half-circular shape with uniform temperature and power distribution (a), (e), (b), (f), (c), (d). Over time, the front side heats up while the rest cools down, leading to an irregular shape (i), (j) where power has its maximum along the defect ring in both CIGS (g) and AZO (h). Afterwards, the defect has a unidirectional growth as shown in (m), (n), (q), and (r), with power peaking at its tip as depicted in (o), (p), (s), and (t). The defect has reached a length of $13.5 \mu\text{m}$ as depicted in the phase plot (r). The defect is clearly propagating away from P3 scribe line towards P1 line, where power is deposited, replicating a behavior of a wormlike defect.

Comparing the results with the baseline simulations, it should be noted that even in the baseline simulations, higher power dissipation is observed on the side facing the P1 line. However, in the centered defect case, the power dissipation is much less asymmetric, resulting in a more or less static defect location throughout the entire simulation interval of 1 ms. The simulations presented here, however, demonstrate that the asymmetric power dissipation of a defect can drive its propagation through the material. These simulation results align well with existing literature on the origin and propagation dynamics of wormlike defects, which suggests that wormlike defects often originate from the P3 scribe line and migrate toward the P1 interconnection line [5, 6].

For further comparison, in Fig. 6.3.8, I compute and depict the power density rather than the direct growth to analyze defect behavior at three main locations: (a) the P3 scribe line, (b) the center, and (c) the P1 scribe line, in addition to the electrical potential for these locations. The figure is arranged in two columns and three rows. The left column shows power density plots for each defect location combining four time instances, with time steps presented on a logarithmic scale: 2×10^{-8} , 2×10^{-7} , 2×10^{-6} , and 2×10^{-5} seconds. The plots visualize the defect contours for each time point. The contour color represents the integrated power in logarithmic scale (i.e. the sum of power in both CIGS and AZO layers) in Wm^{-1} along the normal line over a distance of $-0.1 \mu\text{m}$ to $0.1 \mu\text{m}$ across the contour, while the shading depicts the defected area. At the final time point, surface normal vectors are included, scaled to the integrated power across the contour. I hypothesize that this power drives the expansion of the defect by heating the surrounding area, and thus the plot illustrates the defect's expansion dynamics. In this analysis, I use the term "implied growth rate" to refer to this inferred relationship. The right column in Fig. 6.3.8, on the other hand, depicts 2D electrical potential maps corresponding to the final time point, (i.e. 2×10^{-5} s), for each defect location in a linear scale. These potential maps show the voltage distribution driving the localized power dissipation around the defect.

As shown in Fig. 6.3.8(1), during the initial phase (up to 20 ns), the implied growth rates of defects at P3 and the center are similar, while the defect at P1 scribe line grows more slowly. In the subsequent phase, the defect at the P3 scribe line expands more rapidly at first but then experiences a sharp decline in its implied growth rate as it enlarges. While the center defect's growth nearly matches that of the P3 defect, P1 defect exhibits a higher implied growth rate, particularly after 20 μs . These trends are also reflected in the potential maps in Fig. 6.3.8(2). For the P3 defect, the potential is generally low and asymmetrical, particularly along the sides, but is slightly higher at the tip, which allows further growth toward P1 line. The center defect shows a similar but more symmetrical potential distribution, which tends to keep the defect stationary. In contrast, the P1 defect displays a steep potential drop at the tip and higher potential at the corners, while the rest of the cell's potential is largely unchanged.

The differences in defect behavior observed in Fig. 6.3.8 can be attributed to their respective locations. The defect at the P1 scribe line expands more consistently because it is directly connected to a voltage source, ensuring that

potentials and power remain largely unaffected. The defect at the center grows symmetrically, with its implied growth rate slightly decreasing due to increased conductivity. However, some power is lost through series resistance, which reduces current crowding and slows its implied growth.

The defect at the P3 scribe line follows a growth mechanism similar to the center defect. Initially, its growth rate is slower due to higher series resistance, but it compensates through additional current crowding from one side. As the defect expands, current crowding decreases due to its larger border and improved geometric accessibility, allowing current to flow more effectively from multiple directions. This shows that the growth rate is strongest when the defect is small, with current crowding driving expansion in all directions before the defect gradually forms a worm-like structure, focusing growth at the tip.

It should also be noted that wormlike defects typically propagate in a Brownian motion-like pattern, albeit with a preferential direction toward the P1 line. This Brownian motion-like behavior is not reproduced by the model, which assumes homogeneous cell properties. We argue that this behavior stems from the polycrystalline nature of the CIGS films. Additionally, the duration of the simulated reverse stress was limited by the computational intensity of the process. Therefore, we attribute the apparent lack of propagation for the center and P1 defects to the short time scales of the simulations.

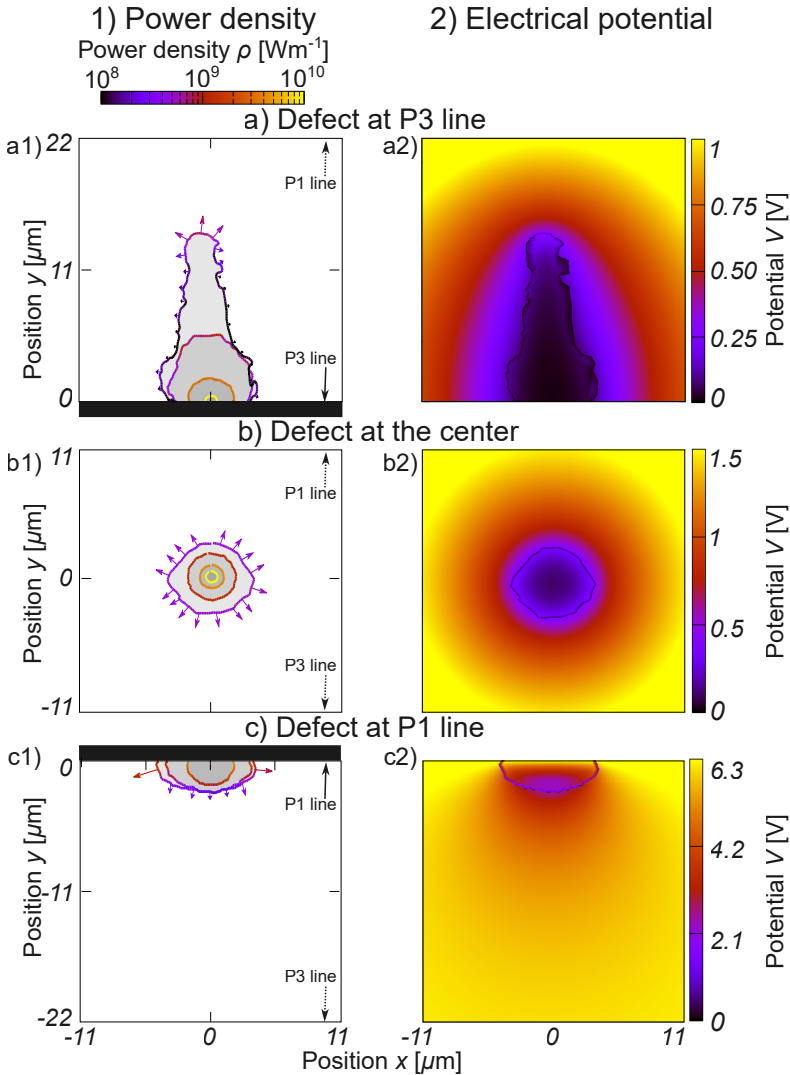


Figure 6.3.8: 1) The implied growth rate in term of power and 2) The electrical potential for a defect at three locations: a) P3 scribe line, b) the center, and c) P1 scribe line. The power shows 4 time points in a logarithmic scale (2×10^{-8} , 2×10^{-7} , 2×10^{-6} , and 2×10^{-5} s), for each defect location. The plots visualize the defect contours for each time point. The contour color represents the integrated power (sum of both in CIGS and AZO layers) along the normal line over a distance of $-0.1 \mu\text{m}$ to $0.1 \mu\text{m}$. At the final time point, surface normal vectors are included to better illustrate the expansion dynamics, with vector length is scaled by power, while the shading as an illustration of the defect area. The potential is depicted for the defect at the three locations, at the final time point in linear scale. Initially, defects at P3 and center grow similarly, while P1 grows slower. After $20 \mu\text{s}$, P3 growth accelerates then declines, P1 growth increases, and center growth follows P3. The P3 defect shows low, asymmetrical potential with a higher tip potential promoting growth toward P1. The center defect's potential is more symmetrical. The P1 defect has a steep potential drop at the tip and higher potential at corners, with the rest of the cell largely unaffected.

6.4 Summary

In this chapter, I examined the impact of thermal properties of various layers within the solar cell stack, as well as the location of defects within the cell, on defect growth using the established coupled finite element method (FEM) model described in Chapter 5. Modifications were made to tailor the model for each specific case under investigation.

I began by analyzing defect growth in non-encapsulated solar cells, in which I needed to remove the encapsulation layer from the thermal model. The results indicated that in the absence of an encapsulation layer, the cell is more susceptible to reverse bias damage, resulting in larger defects compared to encapsulated cells. This is attributed to the encapsulation's ability to maintain the defect at a confined size.

Next, I explored the effects of replacing the glass substrate with a thinner and more thermally conductive material, specifically steel foil. This was done by simply replacing the thermal properties of the substrate from glass to steel. The simulations revealed that while a conductive substrate like steel foil cannot prevent the creation of hotspots and initial reverse bias damage, it can effectively inhibit defect growth by dissipating heat more efficiently through the steel foil, thus limiting heat localization in small areas.

Finally, I investigated how the location of defects within the solar cell influences their growth dynamics and potential for causing damage. By shifting the defect to the interconnection on both long edges of the cell, I replicated conditions for defects at the P1 and P3 scribe lines. The results showed that a defect located at the P1 line (i.e. where the power is also deposited) can restrict the growth due to limited power pathways to the defect. In contrast, a defect positioned at P3 line (i.e. away from the power) exhibited unidirectional growth away from P3 toward P1 line, resulting in a moving "wormlike" defect.

Conclusions

In this work, I have investigated the formation and development of reverse bias damage in CIGS solar cells. The evolution of these reverse bias defects is governed by strong positive-feedback mechanisms, which can often render the process chaotic. Specifically, I propose a three-phase mechanism—nucleation, growth, and wandering—to describe how microscopic electronic or structural imperfections can evolve into large, worm-like defects under reverse bias stress.

1. Nucleation Phase

Positive Feedback and Thermal Runaway

In the first phase, the solar cell experiences a localized junction breakdown when subjected to reverse bias. This breakdown, which is thermally activated, establishes a positive feedback loop: high local currents produce heat, which raises the local temperature, increasing the local conductivity, and thereby attracting even more current. As this feedback intensifies, the cell can undergo thermal runaway and subsequent material decomposition, forming a small, shunt-like defect.

HS-LIT Method Development

To experimentally investigate the onset of this nucleation phase and to quantify the positive feedback loop, I developed the Laser-Induced Hot-Spot Lock-In Thermography (HS-LIT) setup. By incorporating laser modulation into a thermography system, the HS-LIT method allows direct measurement of the temperature rise at a laser-induced hot-spot. This approach made it possible to quantify the loop-gain—i.e., the rate at which thermal runaway can escalate under specific reverse bias conditions.

A key aspect of the method is that through the use of modulation, we can create a non-destructive method that can quantify loop-gains above one. This is achieved as during a modulation cycle, the conditions leading to a loop gain above 1 is followed by a condition with a much lower loop-gain. This way we can quantify a loop-gain

above 1 and drive the device non-destructively into conditions where a non-modulated experiment would experience thermal runaway.

Through HS-LIT measurements, I observed loop-gain values exceeding 1 (up to approximately 2.0 at reverse biases of 3 V), thereby confirming the superlinear susceptibility of CIGS solar cells to thermal runaway at higher reverse bias and increased local temperatures.

Substrate and Location Dependence

The HS-LIT method also revealed significant variation in loop-gain across different regions of the solar cell. Hot-spots forming near the P1 scribe line often exhibited increased loop-gain values, suggesting an elevated risk of localized breakdown. Comparisons between CIGS on steel foil and CIGS on glass showed that steel's higher thermal conductivity reduces the likelihood of runaway by dispersing heat more effectively. Consequently, cells on steel foil formed wider, cooler hot-spots with lower loop-gains (around 1.0), while cells on glass had more localized and hotter spots with correspondingly higher loop-gains.

2. **Growth Phase** Once the initial, small shunt-like defect forms in the nucleation phase, it expands through a second positive feedback mechanism: as current flows through this defect, it dissipates heat locally. The surrounding material—now at a higher temperature—further decomposes, causing the defect to grow in size and consequently become more conductive.

High-Resolution Electro-Thermal FEM Simulations

To understand and replicate the experimentally observed fast time scales (on the order of milliseconds) for defect growth, I developed a coupled electro-thermal finite element model (FEM) with high spatial and temporal resolution. By assuming a small initial defect size 10 nm in radius, the simulations were able to reproduce a final defect size on the order of a $5\ \mu\text{m}$ within one millisecond of reverse bias stress.

Additionally, the model allowed exploration of various parameters—such as defect resistivity and initial defect geometry—while using established literature values for other parts of the solar cell stack. A key result of these simulations is that the power deposited at the defect reaches a maximum that depends on both its size and resistivity. More conductive defects achieve their maximum power dissipation at smaller radii, thus influencing how quickly the defect can expand.

Impact of Other Layers

Using the same FEM framework, I analyzed how device stack layers (e.g., encapsulation with EVA versus exposure to air, or glass versus steel substrates) affect the heating and expansion of the defect. Notably, encapsulation generally mitigates rapid defect growth by promoting heat dissipation away from the hot-spot, whereas a non-

encapsulated device permits more localized heating and potentially larger final defect sizes.

3. **Wandering Phase** In the final wandering phase, the defect no longer grows simply in place but migrates through the solar cell, ultimately forming the worm-like tracks characteristic of advanced reverse bias damage. Both experimental observations and simulations show a tendency for the defect to move toward the P1 line, where electrical power is injected.

Interestingly, defects on the edge where current enters (near the P1 scribing line) tend to remain relatively small, whereas those originating toward the center of the cell or near the P3 scribing line can propagate more extensively and cause permanent damage, consistent with a strong internal drive to move toward the P1 region. Particularly near the P3 line, the defect quickly develops into an elongated shape, moving toward the P1 line.

Through the combination of HS-LIT experiments and electro-thermal FEM simulations, this work demonstrates that the formation of reverse bias damage in CIGS solar cells is a multi-step process driven by strong positive feedback loops at each stage. The susceptibility to thermal runaway is highly sensitive to local conditions—defect location, substrate thermal properties, and encapsulation—all of which modulate heat dissipation and current flow.

By understanding and quantifying these feedback processes, we can more effectively predict the onset of damage, tailor materials or device stack architectures (such as using steel foil substrates with higher thermal conductivity), and develop processing or design strategies to mitigate or delay catastrophic defect formation.

Emissivity using FTIR spectrometer

An important parameter for thermography experiments is the emissivity. For a black body, the thermal radiation from an object is directly linked to the object's temperature. For objects with an emissivity below 1, several effects alter the thermal radiation. First of all, the intensity of the emitted radiation is less, by the factor of the emissivity. Thus, for the same actual thermal amplitude, an object with a lower emissivity will appear to have a lower amplitude. Another complication stems from reflections and transmissions of thermal radiation. As an object with an emissivity less than 1, by definition, does not absorb all incoming radiation, part of the thermal radiation coming from the object's location may actually be reflected or transmitted radiations from the surroundings [100–102].

In this work, I am interested in Lock-In experiments. As in Lock-In experiments temperature differences are detected, the absolute temperature is irrelevant. This means that reflection and transmission of thermal radiation plays no role as long as these contributions are not modulated with the excitation frequency. Thus, in the setup of my experiment, it is not to be expected that reflections affect the measurement. Neither are transmissions from below the sample likely, as the sample is opaque. However, the device consists of a layer stack and each layer in the device has its own spectral emissivity. If the emissivity of the last layer (the layer facing the camera i.e. the encapsulation layer) is not 1, thermal radiation of layers below will mix with the emission of the last layer, i.e., the total thermal radiation emitted by the sample is then a mix of emissions from various depths within the sample. As the signal comes from within the sample, a portion of this radiation will be modulated with the excitation signal and thus will affect the lock-in experiment.

In this study, I aim to determine the emissivity of the encapsulation layer. To do so, a large CIGS sample (i.e. a sample of one cell with an area of 10 cm^2) was encapsulated with an Ethylene Vinyl Acetate (EVA) and Polyethylene Terephthalate (PET) sheet. Subsequently, the encapsulation foil was peeled off and a rectangular piece was cut out of $2 \times 2\text{ cm}^2$. The thickness was determined to be 0.30 mm. For the measurement of the absorption, Fourier-Transform Infrared Spectroscopy (FTIR) measurements were performed.

FTIR is an analytical technique used to obtain a high-resolution IR spec-

trum of absorption of a material [103, 104]. The "Fourier-Transform" in its name refers to the fact that in FTIR the actual measurement is a so-called "interferogram," which is a complex representation of the optical response of the sample. This measured response is then transformed into an absorption (transmission) spectrum using a Fourier Transform. In FTIR, the complete spectrum is measured at once, contrary to a setup with a monochromator, where one wavelength is measured at a time.

Prior to characterizing the EVA sample, a crystalline silicon (c-Si) film was used for calibration. Subsequently, an open window was employed as the background reference. The EVA encapsulation sample was then analyzed using the transmission mode of the FTIR spectrometer, where the transmitted light intensity was measured. The FTIR instrument internally converted the transmission spectrum to absorbance mode using the following formula:

$$A = \log \left(\frac{100}{\%T} \right),$$

where A represents the absorbance and $\%T$ denotes the percentage of light transmitted through the sample. During this conversion, the reflected light from the sample surface was neglected.

The obtained absorbance from the FTIR measurement is shown in Figure A.0.1. For the used camera, the relevant wavelength range is $1.5 - 5.5 \mu\text{m}$, which corresponds to $6667 - 1818 \text{ cm}^{-1}$. above 4000 cm^{-1} the absorbance was not measured. From $4000 - 1818 \text{ cm}^{-1}$, I observe one band of high absorbance between $3100 - 2700 \text{ cm}^{-1}$, with an absorbance of about 4.5. In the remainder, the absorbance is around 0.5.

The transmission (T) can be then obtained again from the absorbance (A) spectrum using the following equation:

$$T = 100 \times 10^{-A}, \quad (\text{A.1})$$

which indicates a transmittance of about 31.6% when the absorbance is 0.5. Regarding reflection, the refractive index (n) of EVA is comparable to that of glass, which is 1.5, while the refractive index of air is 1.0 [105, 106]. Thus, the reflection is given by:

$$R = \left(\frac{n_1 - n_2}{n_1 + n_2} \right)^2 = 4\%, \quad (\text{A.2})$$

where n_1 is refractive index of air, while n_2 is refractive index of EVA. Therefore, the effective transmission of EVA is around 27%.

With a transmittance of approximately 27%, obtaining an accurate measurement of the surface temperature is challenging. One should consider that deep inside the layer stack the highest temperatures are expected, and thus the highest emission rates, meaning that more than 27% of the thermal radiation will originate from deeper layers. To achieve a well-calibrated measurement, applying black paint to the front of the cell would be necessary. However, this would prevent the measurement of luminescence or illuminated characteristics of the cell. For this reason, in this work, I opt to use inaccurate temperature

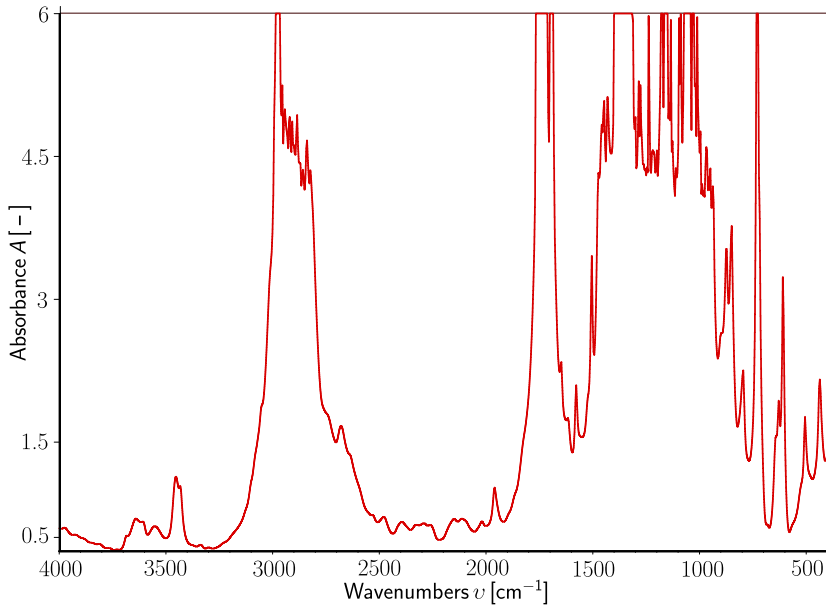


Figure A.0.1: FTIR measurement of EVA layer with an area of $2 \times 2 \text{ cm}^2$ and a thickness of 0.30 mm. The plot shows the absorbance A is depicted as a function of wavenumbers cm^{-1} . EVA has an average absorbance of approximately 5 for the MID-IR range.

estimates. Nonetheless, for a well-calibrated experiment in the future, it is crucial to ensure that the final layer has high emissivity through careful sample design.

Bibliography

- [1] V. Karpov, *Coupled electron–heat transport in nonuniform thin film semiconductor structures*, Physical Review B **86**, 165317 (2012).
- [2] B. J. Stanbery, *Copper indium selenides and related materials for photovoltaic devices*, Critical Reviews in Solid State and Materials Sciences **27**, 73 (2002).
- [3] F. Kessler and D. Rudmann, *Technological aspects of flexible CIGS solar cells and modules*, Solar Energy **77**, 685 (2004).
- [4] C. Zhang, T. Qi, W. Wang, C. Zhao, S. Xu, M. Ma, Y. Feng, W. Li, M. Chen, C. Yang, and W. Li, *High efficiency CIGS solar cells on flexible stainless steel substrate with SiO₂ diffusion barrier layer*, Solar Energy **230**, 1033 (2021).
- [5] P.-O. Westin, U. Zimmermann, L. Stolt, and M. Edoff, in *24th European Photovoltaic Solar Energy Conference, 21-25 September 2009, Hamburg, Germany* (WIP-Renewable Energies, 2009) pp. 2967–2970.
- [6] K. Bakker, H. Nilsson Åhman, K. Aantjes, N. Barreau, A. Weeber, and M. Theelen, *Material property changes in defects caused by reverse bias exposure of CIGS solar cells*, IEEE Journal of Photovoltaics **9**, 1868 (2019).
- [7] U.S. Energy Information Administration, *International energy outlook 2021* (2021).
- [8] J. Keller, K. Kiselman, O. Donzel-Gargand, N. M. Martin, M. Babucci, O. Lundberg, E. Wallin, L. Stolt, and M. Edoff, *High-concentration silver alloying and steep back-contact gallium grading enabling copper indium gallium selenide solar cell with 23.6% efficiency*, Nature Energy **9**, 467 (2024).
- [9] W. Hörig, H. Neumann, H. Sobotta, B. Schumann, and G. Kühn, *The optical properties of CuInSe₂ thin films*, Thin Solid Films **48**, 67 (1978).
- [10] N. Touafek and R. Mahamadi, *Back surface recombination effect on the ultra-thin CIGS solar cells by SCAPS*, International Journal Of Renewable Energy Research **4**, 958–964 (2014).

- [11] Y. Osman, M. Fedawy, M. Abaza, *et al.*, *Optimized CIGS based solar cell towards an efficient solar cell: impact of layers thickness and doping*, *Optical and Quantum Electronics* **53**, 245 (2021).
- [12] N. R. E. Laboratory, Best research-cell efficiency chart, Available at: <https://www.nrel.gov/pv/cell-efficiency.html> (2024), accessed: 2024-12-09.
- [13] Özkalay, Ebrar, Valoti, Flavio, Caccivio, Mauro, Virtuani, Alessandro, Friesen, Gabi, and Ballif, Christophe, *The effect of partial shading on the reliability of photovoltaic modules in the built-environment*, *EPJ Photovolt.* **15**, 7 (2024).
- [14] H. H. Khaing, Y. J. Liang, N. N. M. Htay, and J. Fan, *Characteristics of different solar PV modules under partial shading*, *International Journal of Energy and Power Engineering* **8**, 1418 (2014).
- [15] N. G. Dhere, E. Schneller, and A. Kaul, in *2015 IEEE 42nd Photovoltaic Specialist Conference (PVSC)* (2015) pp. 1–3.
- [16] J. Lee, S. Bae, W. Oh, H. Park, S. M. Kim, D. Lee, J. Nam, C. Mo, D. Kim, J. Yang, Y. Kang, H.-S. Lee, and D. Kim, *Investigation of damage caused by partial shading of $\text{CuIn}_x\text{Ga}_{(1-x)}\text{Se}_2$ photovoltaic modules with bypass diodes*, *Progress in Photovoltaics: Research and Applications* **24** (2016).
- [17] K. Bakker, H. N. Åhman, T. Burgers, N. Barreau, A. Weeber, and M. Theelen, *Propagation mechanism of reverse bias induced defects in $\text{Cu}(\text{In},\text{Ga})\text{Se}_2$ solar cells*, *Solar Energy Materials and Solar Cells* **205**, 110249 (2020).
- [18] K. Bakker, A. Weeber, and M. Theelen, *Reliability implications of partial shading on CIGS photovoltaic devices: A literature review*, *Journal of Materials Research* **34**, 3977 (2019).
- [19] M. Nardone, S. Dahal, and J. Waddle, *Shading-induced failure in thin-film photovoltaic modules: Electrothermal simulation with nonuniformities*, *Solar Energy* **139**, 381 (2016).
- [20] T. Vaas, B. Pieters, A. Gerber, and U. Rau, *Thermal stimulation of reverse breakdown in cigs solar cells*, *IEEE Journal of Photovoltaics* **13**, 398 (2023).
- [21] S. Hegedus and A. Luque, *Handbook of Photovoltaic Science and Engineering, first Edition* (John Wiley & Sons, Inc., 2003).
- [22] P. Würfel, *Physics of Solar Cells: From Basic Principles to Advanced Concepts*, 2nd ed. (Wiley-VCH, Weinheim, 2009) pp. 132–142.
- [23] W. Shockley, *The theory of p-n junctions in semiconductors and p-n junction transistors*, *The Bell System Technical Journal* **28**, 435 (1949).

- [24] D. Abou-Ras, T. Kirchartz, and U. Rau, *Advanced Characterization Techniques for Thin Film Solar Cells* (John Wiley & Sons, Ltd, 2011).
- [25] S. M. Sze and K. K. Ng, *Physics of Semiconductor Devices*, 3rd ed. (Wiley-Interscience, 2006).
- [26] J. Ramanujam and U. P. Singh, *Copper indium gallium selenide based solar cells – a review*, Energy Environ. Sci. **10**, 1306 (2017).
- [27] S. Bose, J. Cunha, J. Borme, W. Chen, N. Nilsson, J. Teixeira, J. Gaspar, J. Leitão, M. Edoff, P. Fernandes, and P. Salomé, A morphological and electronic study of ultrathin rear passivated Cu(In,Ga)Se₂ solar cells (2021).
- [28] S. Roberts, K. Voss, and M. Casini, *Building Integrated Photovoltaics: A Handbook* (Routledge, 2022).
- [29] PV magazine, NICE solar energy sets new world record for CIGS efficiency (Dec. 4, 2019), accessed on: Jan. 23, 2021.
- [30] S. J. Heise, T. Taskesen, A. K. Ndoukoue Chintouo, and J. Ohland, *Which parameters determine the low-light behaviour of CIGSSe-based thin-film solar cells?*, Frontiers in Energy Research **10** (2022).
- [31] W. Li, X. Yan, A. G. Aberle, and S. Venkataraj, *Effect of sodium diffusion on the properties of CIGS solar absorbers prepared using elemental Se in a two-step process*, Scientific Reports **9**, 2729 (2019).
- [32] K. Orgassa, H. W. Schock, and J. H. Werner, *Alternative back contact materials for thin film Cu(In,Ga)Se₂ solar cells*, Thin Solid Films **431-432**, 387 (2003).
- [33] U. Rau and H. Schock, *Electronic properties of Cu(In,Ga)Se₂ heterojunction solar cells—recent achievements, current understanding, and future challenges*, Applied Physics A **69**, 131 (1999).
- [34] A. Morales-Acevedo, *A simple model of graded band-gap CuInGaSe₂ solar cells*, Energy Procedia **2**, 169 (2010), proceedings of Inorganic and Nanostructured Photovoltaics (E-MRS 2009 Symposium B).
- [35] T. Wada, N. Kohara, S. Nishiwaki, and T. Negami, *Characterization of the Cu(In,Ga)Se₂/Mo interface in CIGS solar cells. thin solid films*, Thin Solid Films , 118 (2001).
- [36] K.-J. Hsiao, J.-D. Liu, H.-H. Hsieh, and T.-S. Jiang, *Electrical impact of MoSe₂ on CIGS thin-film solar cells*, Phys. Chem. Chem. Phys. **15**, 18174 (2013).
- [37] A. Sylla, T. Siaka, J.-P. Vilcot, *et al.*, *Theoretical analysis of the effect of the interfacial MoSe₂ layer in CIGS-based solar cells*, Open Journal of Modelling and Simulation **9**, 339 (2021).

- [38] K. S. Cho, J. Jang, J.-H. Park, D.-K. Lee, S. Song, K. Kim, Y.-J. Eo, J. H. Yun, J. Gwak, and C.-H. Chung, *Optimal CdS buffer thickness to form high-quality CdS/Cu(In,Ga)Se₂ junctions in solar cells without plasma damage and shunt paths*, ACS Omega **5**, 23983 (2020).
- [39] B. Williams, V. Zardetto, B. Kniknie, M. Verheijen, W. Kessels, and M. Creatore, *The competing roles of i-ZnO in Cu(In,Ga)Se₂ solar cells*, Solar Energy Materials and Solar Cells **157**, 798 (2016).
- [40] K. Ellmer, *Past achievements and future challenges in the development of optically transparent electrodes*, Nature Photonics **6**, 809 (2012).
- [41] S. Jiang, K. Wang, H. Zhang, Y. Ding, and Q. Yu, *Encapsulation of PV modules using ethylene vinyl acetate copolymer as the encapsulant*, Macromolecular Reaction Engineering **9**, 522 (2015).
- [42] D. Hwang, S. Kuk, Z. Wang, and et al., *Laser scribing of CIGS thin-film solar cell on flexible substrate*, Applied Physics A **123**, 55 (2017).
- [43] F. Jamaatisomarin, R. Chen, S. Hosseini-Zavareh, and S. Lei, *Laser scribing of photovoltaic solar thin films: A review*, Journal of Manufacturing and Materials Processing **7** (2023).
- [44] B. Mistic, B. E. Pieters, U. Schweitzer, A. Gerber, and U. Rau, *Defect diagnostics of scribing failures and Cu-rich debris in Cu(In,Ga)Se₂ thin-film solar modules with electroluminescence and thermography*, IEEE Journal of Photovoltaics **5**, 1179 (2015).
- [45] W. T. Picciano, *Determination of the solar cell equation parameters, including series resistance, from empirical data*, Energy Conversion **9**, 1 (1969).
- [46] A. Ortiz-Conde, F. García-Sánchez, J. Muci, and A. Sucre-González, *A review of diode and solar cell equivalent circuit model lumped parameter extraction procedures*, Facta Universitatis, Series: Electronics and Energetics. **27**, 57 (2014).
- [47] M. J. Heredia-Rios, L. Hernandez-Martinez, M. Linares-Aranda, M. Moreno-Moreno, and J. F. Méndez, *Analysis of losses associated with series resistance (Rs) in simple-structured c-Si solar cells*, Energies **17** (2024).
- [48] D. A. Neamen, *Semiconductor Physics and Devices: Basic Principles*, 4th ed. (McGraw-Hill Education, 2012).
- [49] P. Szaniawski, J. Lindahl, T. Törndahl, U. Zimmermann, and M. Edoff, *Light-enhanced reverse breakdown in Cu(In,Ga)Se₂ solar cells*, Thin Solid Films **535**, 326 (2013).

- [50] S. J. Heise, A. Komilov, M. Richter, B. Pieters, A. Gerber, and J. Neerken, *Reverse-bias behaviour of thin-film solar cells: effects of measurement-induced heating*, EPJ Photovoltaics **14**, 17 (2023).
- [51] S. Johnston, E. Palmiotti, A. Gerber, H. Guthrey, L. Mansfield, T. J. Silverman, M. Al-Jassim, and A. Rockett, in *2017 IEEE 44th Photovoltaic Specialist Conference (PVSC)* (2017) pp. 1400–1404.
- [52] E. Palmiotti, S. Johnston, A. Gerber, H. Guthrey, A. Rockett, L. Mansfield, T. J. Silverman, and M. Al-Jassim, *Identification and analysis of partial shading breakdown sites in $\text{CuIn}_x\text{Ga}_{1-x}\text{Se}_2$ modules*, Solar Energy **161**, 1 (2018).
- [53] S. Johnston, D. Sulas, E. Palmiotti, A. Gerber, H. Guthrey, J. Liu, L. Mansfield, T. J. Silverman, A. Rockett, and M. Al-Jassim, in *2018 IEEE 7th World Conference on Photovoltaic Energy Conversion (WCPEC) (A Joint Conference of 45th IEEE PVSC, 28th PVSEC 34th EU PVSEC)* (2018) pp. 1897–1901.
- [54] T. Silverman, M. Deceglie, C. Deline, and S. Kurtz (2015) p. 95630F.
- [55] S. Dongaonkar, C. Deline, and M. A. Alam, *Performance and reliability implications of two-dimensional shading in monolithic thin-film photovoltaic modules*, IEEE Journal of Photovoltaics **3**, 1367 (2013).
- [56] S. Wendlandt and L. Podlowski, in *Proc. 35th Eur. Photovolt. Sol. Energy Conf. Exhib.* (2018) pp. 1230–1235.
- [57] T. Vaas, B. Pieters, A. Gerber, and U. Rau, *Reverse-bias defect creation in $\text{Cu}(\text{In},\text{Ga})\text{Se}_2$ solar cells and impact of encapsulation*, Solar **3**, 184 (2023).
- [58] H. Guthrey, M. Nardone, S. Johnston, J. Liu, A. Norman, J. Moseley, and M. Al-Jassim, *Characterization and modeling of reverse-bias breakdown in $\text{Cu}(\text{In},\text{Ga})\text{Se}_2$ photovoltaic devices*, Progress in Photovoltaics: Research and Applications **27**, 812 (2019).
- [59] R. Spotnitz and J. Franklin, *Abuse behavior of high-power, lithium-ion cells*, Journal of Power Sources **113**, 81 (2003).
- [60] T. M. Bandhauer, S. Garimella, and T. F. Fuller, *A critical review of thermal issues in lithium-ion batteries*, Journal of The Electrochemical Society **158**, R1 (2011).
- [61] S. Shahid and M. Agelin-Chaab, *A review of thermal runaway prevention and mitigation strategies for lithium-ion batteries*, Energy Conversion and Management: X **16**, 100310 (2022).
- [62] J. H. Lee, *Thermal Runaway in Power Transistors*, Master’s thesis, University of Missouri–Rolla (1968).

- [63] D. Dibra, M. Stecher, S. Decker, A. Lindemann, J. Lutz, and C. Kadow, *On the origin of thermal runaway in a trench power MOSFET*, IEEE Transactions on Electron Devices **58**, 3477 (2011).
- [64] O. Breitenstein and M. Langenkamp, *Lock-in Thermography: Basics and Use for Evaluating Electronic Devices and Materials* (Springer Science & Business Media, 2003).
- [65] F. J. H. de Boer, R. W. van Dijk, and J. H. de Vries, *Thermal imaging and lock-in thermography for solar cell characterization*, Progress in Photovoltaics: Research and Applications (2019).
- [66] O. Breitenstein, *Quantitative evaluation of shunts in solar modules using lock-in thermography*, Solar Energy Materials and Solar Cells **79**, 437 (2003).
- [67] O. Breitenstein, *Application of lock-in thermography to solar cell investigation*, Solar Energy Materials and Solar Cells **48**, 369 (1997).
- [68] O. Breitenstein, *Investigation of shunting in circular monocrystalline solar cells using lock-in thermography*, Journal of Applied Physics **83**, 1234 (1998).
- [69] O. Breitenstein and J. Rakotoniaina, *Electrothermal simulation of a defect in a solar cell*, Journal of Applied Physics **97**, 074905 (2005).
- [70] C. Gearhart, Black-body radiation, in *Compendium of Quantum Physics*, edited by D. Greenberger, K. Hentschel, and F. Weinert (Springer Berlin Heidelberg, Berlin, Heidelberg, 2009) pp. 39–42.
- [71] T. M. Vieira, Ézio C. Santana, L. F. S. Souza, R. O. Silva, T. V. Ferreira, and D. B. Riffel, *A novel experimental procedure for lock-in thermography on solar cells*, AIMS Energy **11**, 503 (2023).
- [72] M. H. Siegloch, *Failure Analysis of Thin Film Solar Modules using Lock-In Thermography*, Ph.D. thesis (2015).
- [73] S. Nofal and B. Pieters, in *IEEE 48th Photovoltaic Specialists Conference (PVSC)* (2021) pp. 1328–1330.
- [74] S. Nofal, B.E. Pieters, M. Hülsbeck, C. Zahren, A. Gerber, and U. Rau, *A direct measure of positive feedback loop-gain due to reverse bias damage in thin-film solar cells using lock-in thermography*, EPJ Photovolt **14**, 6 (2023).
- [75] C. Xu, H. Zhang, J. Parry, S. Perera, G. Long, and H. Zeng, *A single source three-stage evaporation approach to CIGS absorber layer for thin film solar cells*, Solar Energy Materials and Solar Cells **117**, 357 (2013).

- [76] D. Hariskos, M. Powalla, N. Chevaldonnet, D. Lincot, A. Schindler, and B. Dimmler, *Chemical bath deposition of CdS buffer layer: prospects of increasing materials yield and reducing waste*, *Thin Solid Films* **387**, 179 (2001).
- [77] J.-L. Meyzonnette, J. Mangin, and M. Cathelinaud, in *Springer Handbook of Glass* (Springer, 2019) pp. 997–1045.
- [78] M. A. Ordal, R. J. Bell, R. W. Alexander, L. A. Newquist, and M. R. Querry, *Optical properties of Al, Fe, Ti, Ta, W, and Mo at submillimeter wavelengths*, *Appl. Opt.* **27**, 1203 (1988).
- [79] N. Bakker, *Reverse bias degradation of CIGS solar cells*, Dissertation (TU Delft), Delft University of Technology (2023).
- [80] B. E. Pieters and U. Rau, *A new 2d model for the electrical potential in a cell stripe in thin-film solar modules including local defects*, *Progress in Photovoltaics: Research and Applications* **23**, 331 (2015).
- [81] R. Lee, H. Lee, D. Kim, and J. Yoon, *Performance evaluation of flexible CIGS modules based on operational data under outdoor conditions*, *Energy Science & Engineering* **10**, 292 (2022).
- [82] T. Tolio, G. Copani, and W. Terkaj, *Factories of the Future: The Italian Flagship Initiative* (Springer International Publishing, 2019).
- [83] R. Wuerz, A. Eicke, M. Frankenfeld, F. Kessler, M. Powalla, P. Rogin, and O. Yazdani-Assl, *CIGS thin-film solar cells on steel substrates*, *Thin Solid Films* **517**, 2415 (2009).
- [84] L. Zortea, S. Nishiwaki, T. P. Weiss, S. Haass, J. Perrenoud, L. Greuter, T. Feurer, G. Palaniswamy, S. Buecheler, and A. N. Tiwari, *Cu(In,Ga)Se₂ solar cells on low cost mild steel substrates*, *Solar Energy* **175**, 25 (2018).
- [85] T. Yagioka, *Cd-free flexible Cu(In, Ga)Se₂ thin film solar cells with ZnS(O, OH) buffer layers on Ti foils*, *Applied Physics Express* **2**, 2201 (2009).
- [86] D. Brémaud, D. Rudmann, M. Kaelin, K. Ernits, G. Bilger, M. Döbeli, H. Zogg, and A. Tiwari, *Flexible Cu(In,Ga)Se₂ on Al foils and the effects of Al during chemical bath deposition*, *Thin Solid Films* **515**, 5857 (2007).
- [87] M. Stanley, M. Jubault, F. Donsanti, and N. Naghavi, *Flexible Cu(In,Ga)Se₂ based solar cells using molybdenum foils as substrate*, *physica status solidi c* **14** (2017).
- [88] D. Bremaud, D. Rudmann, G. Bilger, H. Zogg, and A. Tiwari, in *Conference Record of the Thirty-first IEEE Photovoltaic Specialists Conference, 2005.* (2005) pp. 223–226.

- [89] S. Nofal, T. S. Vaas, U. Rau, and B. E. Pieters, *An electro-thermal finite element method (FEM) model for local hotspot kinetics in Cu(In, Ga)Se₂ thin-film solar modules*, Journal of Applied Physics **136**, 115102 (2024).
- [90] Tinoco, T. and Rincón, C. and Quintero, M. and Pérez, G. Sánchez, *Phase Diagram and Optical Energy Gaps for CuIn_yGa_{1-y}Se₂ Alloys*, physica status solidi (a) **124**, 427 (1991).
- [91] F. Hecht, *New development in FreeFem++*, J. Numer. Math. **20**, 251 (2012).
- [92] G. Sadaka, Freefem++, a tool to solve PDEs numerically (2012), arXiv:1205.1293 .
- [93] F. P. Incropera, D. P. DeWitt, T. L. Bergman, and A. S. Lavine, *Fundamentals of Heat and Mass Transfer*, 6th ed. (John Wiley & Sons, Hoboken, NJ, 2007).
- [94] J. Speight and N. Lange, *Lange's Handbook of Chemistry*, 16th ed. (McGraw-Hill, New York, 1992).
- [95] W. Haynes, *CRC Handbook of Chemistry and Physics*, CRC Handbook of Chemistry and Physics (CRC Press, 2014).
- [96] R. A. Matula, *Electrical resistivity of copper, gold, palladium, and silver*, Journal of Physical and Chemical Reference Data **8**, 1147 (1979).
- [97] O. Breitenstein, J. Bauer, K. Bothe, W. Kwapil, D. Lausch, U. Rau, J. Schmidt, M. Schneemann, M. C. Schubert, J.-M. Wagner, and W. Warta, *Understanding junction breakdown in multicrystalline solar cells*, Journal of Applied Physics **109**, 071101 (2011).
- [98] S. Azizi, Éric David, M. F. Fréchette, P. Nguyen-Tri, and C. M. Ouellet-Plamondon, *Electrical and thermal conductivity of ethylene vinyl acetate composite with graphene and carbon black filler*, Polymer Testing **72**, 24 (2018).
- [99] L. M. Mansfield, I. L. Repins, R. L. Garris, M. A. Contreras, K. A. Horowitz, and K. Ramanathan, *Cell-level reliability testing procedures for CIGS photovoltaics*, MRS Advances **6**, 555 (2021).
- [100] M. Kasemann, B. Walter, C. Meinhardt, J. Ebser, W. Kwapil, and W. Warta, *Emissivity-corrected power loss calibration for lock-in thermography measurements on silicon solar cells*, Journal of Applied Physics **103**, 113503 (2008).
- [101] K. Li, G. Y. Tian, and J. Ahmed, *Emissivity correction and thermal pattern reconstruction in eddy current pulsed thermography*, Sensors **23** (2023).

- [102] Y. Gao and G. Y. Tian, *Emissivity correction using spectrum correlation of infrared and visible images*, *Sensors and Actuators A: Physical* **270**, 8 (2018).
- [103] B. C. Smith, *Fundamentals of Fourier transform infrared spectroscopy* (CRC press, 2011).
- [104] J. S. Gaffney, N. A. Marley, and D. E. Jones, *Fourier Transform Infrared (FTIR) Spectroscopy* (John Wiley & Sons, Ltd, 2012) pp. 1–33.
- [105] P. Spinelli, F. Lenzenmann, A. Weeber, and A. Polman, *Effect of EVA encapsulation on antireflection properties of Mie nanoscatterers for c-Si solar cells*, *IEEE Journal of Photovoltaics* **5**, 559 (2015).
- [106] K. R. McIntosh, J. N. Cotsell, J. S. Cumpston, A. W. Norris, N. E. Powell, and B. M. Ketola, in *34th IEEE Photovoltaic Specialists Conference (PVSC)* (2009) pp. 544–549.

Curriculum Vitae

5th Dec 2025	Doctoral Examination for Dr.-Ing.
2019-2024	Research Assistant and Doctoral Candidate Institute of Energy Materials and Devices, Photovoltaics (IMD-3) RWTH Aachen University, Germany
2015-2019	Master of Science in Renewable Energy and Sustainability Palestine Polytechnic University, Palestine
2018	Research Assistant Institute of Energy Materials and Devices, Photovoltaics (IMD-3) RWTH Aachen University, Germany
2017	ERASMUS semester at Sapienza University of Rome, Italy
2008-2013	Bachelor of Art in Civil Engineering Palestine Polytechnic University, Palestine
2008	Higher Education Entrance Qualification (Tawjihi) Idna Secondary School for Girls, Palestine
1990	Born in Idna, Palestine

Acknowledgments

First and foremost, I would like to thank my parents: Jamal and Naima, and my siblings: Abeer, Tahreer, Nofal, Ghada, Raghda, and Ahmed. Their unwavering support throughout my journey as a PhD student has been my anchor. I could not have reached this point without their encouragement and belief in me, even from afar.

I would also like to thank my best friends in Palestine: Wafa, Riham, Mariam, Rahma, and Marwa, for their continued support, encouragement, and motivation. Their pride in what I do, and their presence have meant more to me than words can express.

I would like to express my admiration and appreciation to Dr. Bart Pieters, who has had a profound impact on my work and my growth as a scientist. I feel very fortunate to have him as my mentor. His guidance, feedback, and ideas have been invaluable, and he consistently encouraged and challenged me to grow both professionally and personally. I am especially thankful that he gave me the freedom and space to explore and try things independently in my work, while always being there when I needed help, feedback, or guidance. I greatly appreciate his patience in explaining complex concepts and sharing his expertise in physics and electrical engineering. I am also grateful for the many meetings we had discussing new ideas, some of which turned into memorable conversations over coffee, and sometimes even about unicorns. I feel honored that he let me name one of his servers “Gummybear”. Working with Bart has been inspiring and rewarding. I could talk with him for hours about nearly anything, which truly shows how much I value him, both as a remarkable scientist and as a person. I am truly thankful for his support and friendship throughout my PhD journey.

I am also deeply grateful to Prof. Dr. Uwe Rau for his trust in my abilities and for believing in me, offering me the opportunity to continue at IMD-3 after my MSc and to do my PhD. His support, expertise, insightful input, and insistence on high standards in my publications have been invaluable. His encouragement throughout my MSc and PhD journeys always motivated me to give my best. I would like to also thank Prof. Michael Powalla for his support as the second examiner.

Furthermore, I am grateful to Prof. Maurice Nuys, my MSc supervisor, who was the first person I met from the IMD-3 institute when he visited Palestine in

2018 to discuss my suitability for doing my MSc thesis at the institute. Despite my limited experience in lab work, he believed in me and gave me the chance to prove myself. Under his guidance, I grew as a scientist and learned a great deal, including from my mistakes, receiving his support and encouragement to stay curious, ask questions, and explore. This experience paved the way for me to begin my PhD journey at IMD-3.

I also appreciate Markus Hülsbeck, who has been the main person I worked in the lab with during my MSc. He provided guidance while giving me the freedom to explore and try things independently in the lab. His support continued during my PhD. Markus was a major part of my experimental work, and I learned a lot from him, especially regarding lasers and optics. I also appreciate his stimulating discussions and creative ideas we put together, which greatly helped me advance my research.

A special thanks goes to the entire "Messtechnik" group. I am especially grateful to Dr. Andreas Gerber, whose advice I could always rely on, both professionally and personally. I would like to thank Dr. Timon Vaas for sharing his valuable experience in the field of CIGS, which was the topic of his MSc. I greatly appreciate his willingness to explain his work, guide me on where to start, how to proceed, and patiently answer my questions. I am honored to continue this work as his successor and build upon it.

I also thank Christoph Zahren for his help with laboratory setups, particularly for building the thermography setup, and for the valuable discussions and ideas we shared on how to improve it. I am also grateful to Niklas Bongartz for his support with sample preparation and his help with experiments on the thermography setup. I would like to thank Sabine Kasper and Jonathan Werner for their assistance with the samples I used, and Thomas Birrenbach for his help with the laminator. Furthermore, I am thankful to Evgenii Sovetkin, Jonas Noll, Dirk Erdweg, Wilfried Reetz, Willi Hilgers, and all others in the group who were always there to help whenever needed.

Alongside all the brilliant people, I would also like to give a lighthearted thanks to my "monsters" that supported me throughout this journey: my PC "Big Monster" for running endless simulations, my laptop "Monster" for helping me do most of my PhD work, my phone "Little Monster", and the servers "Ponytail" and "BadBunny" that also supported my simulation work. I would also like to thank "Elefantos", the step stool in the lab, which was essential for helping me reach many of my goals, quite literally. Without them, much of this work would not have been possible.

Moreover, I deeply appreciate everyone I met during my time at IEK-5/IMD-3. From the moment I arrived in 2018, this institute became my first *HOME* in Germany; a place where I felt happy, supported, and motivated to give my best. I would like to thank the lunch group: Timon, Zina, Georgette, and Yoma, as lunchtime was something I looked forward to, not only for the good food, but also for the great company, laughter, and our conversations about life, culture, and, of course, food. The connection, support and friendship I have gained with you is one of the greatest rewards of this journey. A special mention goes to Timon and Niklas for letting me express myself in our shared

office. They never minded the colorful decorations, unicorn-like themes, and the endless stickers and labels I used to name everything. They made my office time truly memorable, and I will always cherish our discussions and laughter.

Moreover, I am especially grateful to Sina Kurth, who was a true support during my MSc; thanks to her, I learned how to ride a bike; an impact that will last forever. I would like to thank Nelli Hambach, with whom I worked on similar CIGS samples but for different topics. We frequently discussed and exchanged ideas, which was very helpful. I am also grateful to Seçil and Thérèse for the hiking trips and gatherings over coffee or lunch, which truly helped to de-stress PhD life. I would also like to thank: Basita, Sergey, Alex, Benedikt, Ugochi, Toby, Li-Chung, Aryak, Jinan, Sandheep, Ashish, Mory, Ifeanyi, Yaqin, Binbin, Yanxin, Sercan, Uchechi, Katharina, Gaosheng, and Johanna, for the regular social gatherings and for sharing experiences, advice, and tips throughout our PhD journey. The thank you also goes to other members of the institute who I was happy to share moments and conversations with: Yannick, Janine, Gina, Alain, Pascal, Ralf, Petra, Daniel, Joachim, Stefan, Tsvetelina, Benjamin, Resi, Thomas, Gunnar, Brigitte, Frank, Dr. Beyer and many more.

I was also lucky to meet other people during this time that I can call friends, including Gerrit, Kübra, Tim, and many more.

Looking back, this journey has been about much more than earning a PhD; it represents an entire chapter of my life that I have built here in Germany. I am deeply grateful to everyone I have met, worked with, or shared a conversation or warm moment with. Each interaction has shaped my experience in meaningful ways.

At the end, I would like to thank my family in Germany and Palestine for their unconditional love and support throughout this journey. Through both good and difficult times, they definitely made this journey brighter and lighter.

Band / Volume 691

A Parallel-in-Space Simulator for Accelerating Power System Simulation on Graphics Processing Units

J. Zhang (2026), 112 pp

ISBN: 978-3-95806-882-7

Band / Volume 692

Entwicklung von Reparaturmethoden für einkristalline Bauteile mittels thermischer Spritzverfahren

M. L. Létang (2026), X, 211 pp

ISBN: 978-3-95806-883-4

Band / Volume 693

Assessing the Environmental Implications of Offshore Wind Energy Advancements on the Future German Electricity Sector

A. Benitez (2026), xi, 176 pp

ISBN: 978-3-95806-885-8

Band / Volume 694

Entwicklung von Korrosionsschutzschichten für Protonen-Austausch-Membran-Wasserelektrolyseure

T. Sievert (2026), 201 pp

ISBN: 978-3-95806-888-9

Band / Volume 695

Hierarchical Modeling of Electrocatalytic Reactions from a Local Perspective

X. Zhu (2026), ix, 121 pp

ISBN: 978-3-95806-889-6

Band / Volume 696

Nanocrystalline Silicon Carbide in Transparent Passivating Contact Solar Cells

A. Eberst (2026), xiii, 225 pp

ISBN: 978-3-95806-891-9

Band / Volume 697

Theory of Electronic and Ionic Perturbations at Supported Electrocatalyst Nanoparticles

Y. Zhang (2026), XI, 131 pp

ISBN: 978-3-95806-896-4

Band / Volume 698

Aufbau und Einsatz eines on-board Messsystems zur Untersuchung der Abgaszusammensetzung von Fahrzeugen betrieben mit konventionellen und alternativen Kraftstoffen

V. Polinowski (2026), VIII, 269 pp

ISBN: 978-3-95806-897-1

Band / Volume 699

Ab Initio-based large-scale Atomistic Simulations of Cathode Materials for Secondary Batteries: From Computational Methodologies to Applications towards improved Structural and Chemical Stability

K. Köster (2026), x, 204, x pp

ISBN: 978-3-95806-898-8

Band / Volume 700

Materials Design, Processing and Application of Proton-Conducting Oxides for Electrochemical Energy Conversion

Y. Zeng (2026), vii, 117 pp

ISBN: 978-3-95806-899-5

Band / Volume 701

Accelerating the discovery of alkaline-stable anion exchange membrane materials via computational exploration

F. P. Tipp (2026), xii, 135 pp

ISBN: 978-3-95806-900-8

Band / Volume 702

Methods for Investigating the Structure-Performance Correlation in Membrane Electrode Assemblies

N. Utsch (2026), XIII, 138, LXVII pp

ISBN: 978-3-95806-901-5

Band / Volume 703

Hot-Spot Formation in Cu(In,Ga)Se₂ Thin Film Solar Cells

S. Nofal (2026), xvii, 131 pp

ISBN: 978-3-95806-903-9

Energie & Umwelt / Energy & Environment
Band / Volume 703
ISBN 978-3-95806-903-9

Mitglied der Helmholtz-Gemeinschaft

